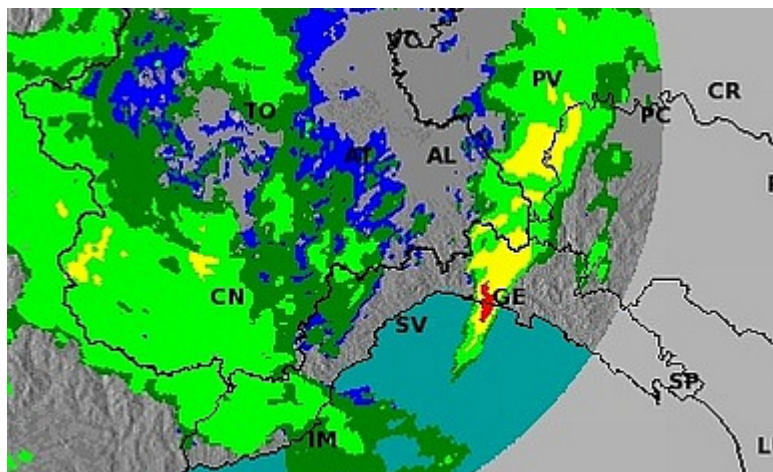


Ph.D. Program in Civil, Chemical and Environmental  
Engineering Curriculum in Fluid Dynamics and Environmental  
Engineering



*Department of Civil, Chemical and Environmental Engineering  
Polytechnic School, University of Genoa, Italy.*



**Exploiting the WRF-ARW model for  
the prediction of flash-floods events  
over Liguria: a validation strategy and  
an investigation of the role of the sea  
surface temperature**

Francesco Ferrari



Exploiting the WRF-ARW model for the  
prediction of flash-floods events over Liguria:  
a validation strategy and an investigation of  
the role of the sea surface temperature

by

Francesco Ferrari

*Dissertation discussed in partial fulfillment of  
the requirements for the Degree of*

DOCTOR OF PHILOSOPHY

*Civil, Chemical and Environmental Engineering  
curriculum in Fluid Dynamics and Environmental Engineering,*

*Department of Civil, Chemical and Environmental Engineering,*

*University of Genoa, Italy*



October, 2016

Advisor:

Prof. Andrea Mazzino - Dipartimento di Ingegneria Civile, Chimica e Ambientale, Università degli Studi di Genova

External Reviewers:

Prof. Silvana Di Sabatino - Dipartimento di Fisica e Astronomia, Università di Bologna

Prof. Enrico Zambianchi - Dipartimento di Scienze per l'Ambiente, Università di Napoli Parthenope

Examination Committee:

Prof. Marco Colombini - Dipartimento di Ingegneria Civile, Chimica e Ambientale, Università degli Studi di Genova

Prof. Ambrogio Manzino - Dipartimento di Ingegneria dell'Ambiente, del Territorio e delle Infrastrutture, Politecnico di Torino

Prof. Alessandro Stocchino - Dipartimento di Ingegneria Civile, Chimica e Ambientale, Università degli Studi di Genova

Ph.D. program in Civil, Chemical and Environmental Engineering  
*Curriculum in Fluid Dynamics and Environmental Engineering*  
*Cycle XXIX*

# Contents

<b>Contents</b>	<b>v</b>
<b>Introduction</b>	<b>1</b>
<b>1 Introduction to atmospheric physics</b>	<b>7</b>
1.1 Introduction . . . . .	7
1.2 Atmospheric dynamics . . . . .	9
1.3 Geostrophic approximation . . . . .	16
1.4 Averaged conservation equations . . . . .	19
<b>2 Numerical weather prediction</b>	<b>23</b>
2.1 Introduction . . . . .	23
2.2 Methods of solutions . . . . .	24
2.3 Parameterizations . . . . .	27
2.4 Global and limited area models . . . . .	33
2.5 The Weather Research and Forecasting model . . . . .	34
<b>3 Simulation of heavy precipitations over Liguria with WRF</b>	<b>45</b>
3.1 Introduction . . . . .	45
3.2 Materials and methods . . . . .	49
3.3 Verification methodology . . . . .	60
3.4 Results and discussion . . . . .	63
3.5 Conclusions . . . . .	84
<b>4 The role of the Sea Surface Temperature on the flash floods events over Liguria</b>	<b>87</b>
4.1 Introduction . . . . .	87
4.2 The analyzed case-studies . . . . .	89

4.3	Model setting and simulations . . . . .	89
4.4	The role of the sea surface temperature . . . . .	92
4.5	Conclusions and perspectives . . . . .	102
	<b>Conclusioni</b>	<b>105</b>
	<b>Bibliography</b>	<b>109</b>

# Introduction

The possibility of forecasting the evolution of atmospheric phenomena through application of thermodynamics and fluid dynamics laws in the last decades had a remarkable development as a consequence of the advancement in computing capacity and of the possibility to have reliable observations.

Already in 1904 Vilhelm Bjerknes recognized that forecasting is fundamentally an initial value problem in mathematical physics, and moreover, that the basic system of equations to be solved was already known, at least in general form: conservation of mass, conservation of momentum (Navier-Stokes equations), conservation of thermodynamic energy and radiative transfer equation. But Bjerknes realized that this system of highly non linear partial differential equations did not possess closed solutions, except in grossly simplified forms that had little direct use in forecasting. In addition, the availability of data necessary to determine the initial conditions were wholly inadequate. During and immediately after World War I, the British scientist Lewis Fry Richardson made the first attempt to predict the weather numerically. Richardson showed how the differential equations governing atmospheric motions could be written approximately as a set of algebraic difference equations for values of the tendencies of various field variables at a finite number of points in space covering the domain of interest. Given the observed values of the field variables at these grid points, the tendencies could be calculated numerically by solving the algebraic difference equations. Richardson worked out one example forecast for surface pressure tendencies at two grid points, but the results were very poor and predicted pressure changes were an order of magnitude larger than those observed.

After Richardson failure to obtain a reasonable forecast, numerical predic-

tion was not again attempted for many years. Finally, after World War II interest in numerical prediction revived due partly to the vast expansion of the meteorological observation network, which provided much improved initial data, also thanks to the invention of the radiosonde in the 1930s resulting in the widespread use of upper air data. Even more important was the development of digital computers, which made the enormous volume of arithmetic operations required in a numerical forecast model; in this context the era of dynamical forecasting by numerical methods, commonly referred to as numerical weather prediction (NWP), begins and soon became the primary basis for modern weather prediction.

NWP must include representations of large-scale dynamical processes, small-scale frictional processes in the atmospheric boundary layer, small-scale drag due to gravity waves, short-wave and long-wave radiative transfer, water-vapor transport, the effects of clouds, precipitation and the transfer of heat, momentum and moisture between the surface and the atmosphere. Some of these phenomena, once that the resolution of the grid over which solve the equations is fixed, can take place on length scales below the grid size and are therefore not explicitly represented in the model. Such processes must be parameterized, that is, expressed in terms of quantities that are explicitly represented. Such parameterizations often involve empirical formulas that do not have rigorous physical justification and may involve disposable constants whose values are poorly known. Much of the art of NWP consists in selecting these constants in such a way as to optimize the resulting forecasts ([Andrews, 2010](#)). Unfortunately none of existing parameterizations is completely satisfactory, resulting in introduction of further errors in the simulations.

Finally, in addition to errors due to parameterization of unresolved phenomena and errors introduced by the discretization of model equations, an other considerable source of errors is the not exact knowledge of the initial conditions that must be provided to the model; indeed initial fields are produced interpolating over the model grid an high number of observed data, non homogeneously distributed, coming from many sources (ground stations, buoys, aircraft, satellite, etc.) resulting therefore approximation of the actual situation. Definitely, all these aspects contribute on model errors, affecting especially the simulation of small scale phenomena.

Unfortunately in most cases small scale phenomena can have heavy impact

on human activities and consequently their correct forecast is one of the major challenges of NWP. For example Liguria is a region frequently subject to floods caused by very localized quasi-stationary, V-shaped convective systems resulting in casualties and very high damages. An example is visible in Figure 0.1 where the radar image, showing the convective system that affected the city of Genoa during the 4 November 2011 flood, emphasizes the extremely limited extension of the system (about ten kilometers in transversal direction); these V-shaped convective systems are triggered by the convergence between a warm and moist south-easterly low-level jet on the eastern side of the region, induced by the presence of deep pressure minimum just west Liguria, and a northerly shallow cold flow due to the presence of a relatively high pressure area over the Po Valley. Nevertheless large scale conditions that lead to the generation of this kind of events are well known and predictable with a satisfactory degree of reliability, the prediction of exact localization, intensity and duration of the convergence line is very problematic. If an high pressure area is present over East Europe preventing the usual East shift of the system, it can remain stationary over the same areas for several hours causing severe floods, but, if during the event also a light shift of the structure intervenes, the precipitations can affect different catch basins, drastically reducing the risk of floods. Liguria indeed is characterized by a sequence of very small catch basins perpendicular to the coast and also a little error in space-temporal localization, in intensity and in evolution speed of the system itself can produce very different scenarios. In order to reduce the hazards due to these events it is therefore evident the importance in reduction as much as possible of the uncertainties associated with the forecast of these convective systems.

In the present PhD thesis I will perform simulations of the four most recent floods that hit Liguria region (Varazze and Sestri Ponente, 4 October 2010, Cinque Terre and Val di Vara, 25 October 2011, and Genoa, 4 November 2011 and 9 October 2014). In particular I will study the effects on simulations of the following features:

- i)* the resolution of the grid over which the equations are discretized,
- ii)* the way in which water species within the clouds are parameterized and
- iii)* the sea surface temperature (SST).

I will focus on these aspects because they have a crucial role in the simu-

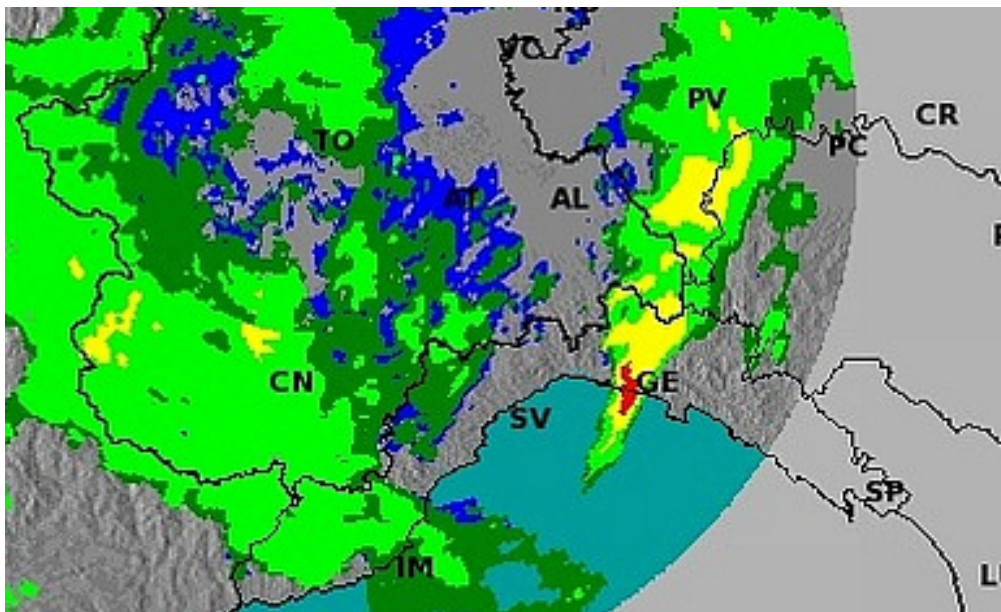


Figure 0.1: Radar image showing the convective system causing the flood the hit Genoa; 11.40 UTC, 4 November, 2011.

lation of the severe events studied. Indeed high resolution simulations are necessary to explicitly resolve convection and localize convergences and precipitation peaks. Microphysical schemes, that are the parameterizations responsible for computing atmospheric water vapor, cloud liquid water, cloud ice and various types of precipitation, are crucial for a correct prediction of severe rainfall events. Finally, the period of the year in which these events (and almost all floods that hit Liguria region in the past) usually occurred, between late summer and mid autumn, suggests that SST can have a strong influence in triggering the convective systems considered. In this period indeed heat and moisture fluxes from the Mediterranean Sea reach the highest values of the year.

The model studied in order to produce these simulations will be the Weather Research and Forecasting (WRF) model, a numerical weather prediction and atmospheric simulation system designed for both research and operational applications (*Skamarock et al., 2008*). WRF is the state of the art in numerical modeling of the atmosphere, produced by a collaboration between several American agencies and universities and suitable for a broad

span of applications across scales ranging from large-eddy to global simulations.

The WRF simulations that will be produced in this thesis will be performed over three two-way nested domains covering western and central Europe with horizontal resolution of 10 km, northern Italy with horizontal resolution of 3.3 km and the Liguria region with a grid spacing of 1.1 km. Different microphysics parameterization schemes, and different SST initializations will be applied.

For the analysis of the simulations two different approaches will be adopted: the calculation of traditional categorical indices based on punctual matching between forecast and observations will be then flanked by a new generation spatial verification techniques based on comparison between features (precipitation patterns in the present case) that characterize both forecast and observations (*Davis et al., 2006; Davis et al., 2006; Davis et al., 2009*). This last method is more suitable to evaluate high resolution simulations because fine-scale differences that are not present in coarser resolution forecasts may be penalized by traditional scores, strongly sensitive to localization and timing errors up to the space and time resolution of the sample (*Lack et al., 2010*). Such shortcomings can be expressed with the so-called 'double penalty effect': a spatially shifted, but otherwise perfect forecast, gives rise to a double error: a miss where rain is observed and a false alarm where it is predicted.

The main results obtained will be:

- a quite strong dependence of the quantitative precipitation forecasts on the adopted microphysics parameterization schemes and on the domain grid resolution; the best performances of higher resolution simulations to provide more realistic and detailed precipitation patterns clearly will emerge from the application of spatial verification techniques, while conclusions that will stem from classical point-based analysis will appear to be misleading due to the double-penalty problem. In particular a set of parameterization schemes able to correctly capture and localize the convergence phenomenon at the basis of the floods analyzed will be identified;
- a significant sensitivity to the SST field ingested by WRF model in the development of the severe flash floods here investigated: in most cases also small variations in SST field will produce a modification in pressure field forecasts and a moistening of the southerly flows. These facts will result

in a strengthening of the convergence phenomenon with the consequent enhancement of precipitation forecasts.

The structure of the thesis will be the following:

in Chapter 1 a brief introduction to basic equations governing atmospheric physics and their averaged formulation, that are the basis of many NWP, will be reported;

in Chapter 2 numerical weather predictions will be presented: numerical methods, global and limited area models, main parameterizations necessary to close models equations; finally the WRF model will be introduced;

in Chapter 3 a description of three different case studies, corresponding to severe rainfall events occurred over the Liguria region between October 2010 and November 2011 will be reported. Then, an intercomparison of eight different microphysics parameterization schemes available in the WRF model and an analysis of the sensitivity of predicted precipitation to horizontal resolution will be presented. The data set used to evaluate model performances will be extracted from the official regional network, composed of about 150 professional WMO-compliant stations. Two different strategies will be exploited to assess the model skill in forecasting precipitation: a traditional approach, where forecasts and observations will be matched on a point-by-point basis, and an object-based method where model success will be based on the correct localization and intensity of precipitation patterns;

in Chapter 4 the sensitivity to SST of the small-scale flood-causing system described in the Chapter 3, plus a further event happened in 2014, will be analyzed. For this purpose two different SST initializations will be considered: a coarse field provided by a global atmospheric model and a high-resolution multi-satellite analysis. For the analysis of the effect of different SST fields, quantitative precipitation forecasts will be evaluated for different forecasting ranges (24, 36 and 48  $h$ ), and in one case, for different large scale initial conditions.

# Chapter 1

## Introduction to atmospheric physics

### 1.1 Introduction

The Atmosphere, a stratified multilayer of gases that surrounds Earth and retained by Earth's gravity, consists of a mixture of gasses present in different concentrations: although molecular nitrogen and molecular oxygen predominate by volume, the minor constituents carbon dioxide, water vapor and ozone play crucial roles in the evolution of atmosphere itself; water in particular is the only atmospheric constituent that can change phase at the typical pressures and temperatures experienced in the Earth atmosphere. In this chapter the basic physical principles that allow to interpret and model physical processes that take places in the Earth atmosphere are introduced.

The major forcing of the atmosphere derives from the Sun, though interactions with the land and the ocean are also important. Sun radiations is fundamental for atmospheric evolution both from a thermodynamic point of view, both from a chemical point of view.

The atmosphere is continually bombarded by solar photons at infra-red, visible and ultra-violet wavelengths. Some solar photons are scattered back to space by atmospheric gases or reflected back to space by clouds or the Earth surface; some are absorbed by atmospheric molecules (especially water vapor and ozone) or clouds, leading to heating of parts of the atmosphere, and some reach the Earth surface and heat it. Atmospheric gases (espe-

cially carbon dioxide, water vapor and ozone), clouds and the Earth surface also emit and absorb infra-red photons, leading to further heat transfer between one region and another, or loss of heat to space ([Andrews, 2010](#)): the balance of all these phenomena determines the mean Earth surface temperature of about  $288\text{ K}$  and the vertical structure of the atmosphere. The atmosphere indeed is conventionally divided into layers in the vertical direction, according to the variation of temperature with height, as shown in Figure 1.1 for the lower  $100\text{ km}$ . In the following we will focus on the troposphere inasmuch is the atmospheric layer where weather phenomena take place.

Because it is a fluid system, the atmosphere is capable of supporting a

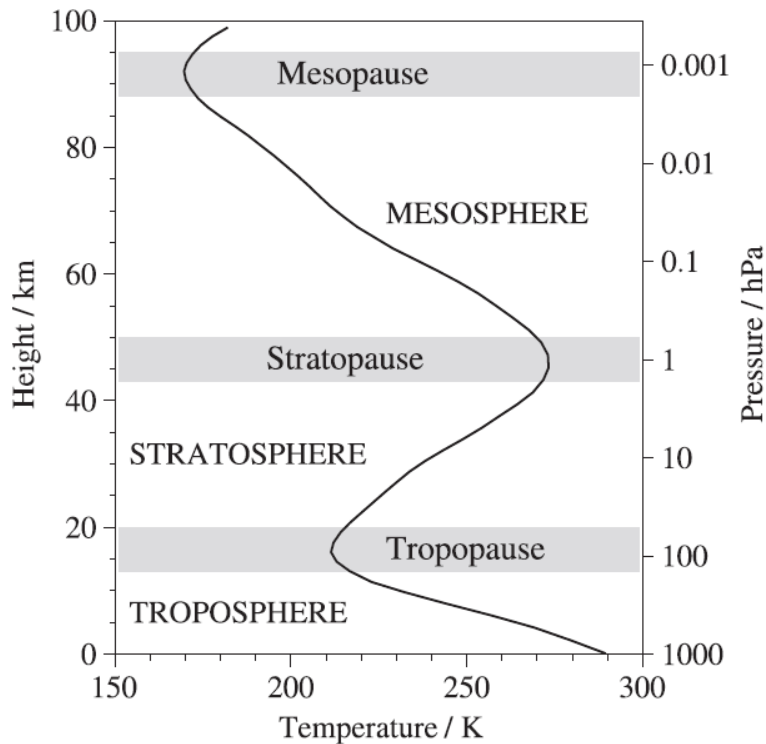


Figure 1.1: Atmosphere vertical structure. Picture from *An introduction to atmospheric physics*, second edition, D. G. Andrews.

wide spectrum of motions. These range from turbulent eddies of a few meters or low, to circulations with dimensions of the Earth itself making the description of the atmospheric system very complex ([Salby, 2012](#)).

## 1.2 Atmospheric dynamics

This section introduces the basic fluid-dynamical laws that govern the wide variety of fluid flows occurring in the atmosphere. The length scales of interest, as reported in Table 3.1 for atmospheric phenomena occurring in middle latitudes, range from meters to thousands of kilometers; these are many orders of magnitude greater than molecular scales such as the mean free path, at least in the lower and middle atmosphere. We may therefore

Table 1.1: Some atmospheric phenomena of middle latitudes as a function of scale. Table from *Numerical Prediction and dynamic meteorology*. John Wiley & sons, second edition, G. J. Haltiner and R. T. Williams.

Scale	horizontal space scale ( <i>km</i> )	time scale ( <i>h</i> )	Typical phenomena
Planetary	$10^4$	$10^3$	long waves, sub-tropical anticyclones
Synoptic	$10^3$	$10^2$	extra tropical depressions, anticyclones
Meso	$10^2$	10	fronts, squall lines
Convective	10	1	convective clouds, tornadoes
Micro	$< 1$	$< 10^{-1}$	boundary layer eddies

average over many molecules, ignoring individual molecular motions and regarding the fluid as continuous. "Local" values of quantities such as density, temperature and velocity may be defined at length scales that are much greater than the mean free path but much less than the scales on which the meteorological motion varies; so for describing the atmospheric evolution are sufficient three partial differential equations:

- the mass conservation for a fluid system (continuity equation)
- the first law of the thermodynamics

- the Newton second law applied to a continuous fluid (Navier-Stokes equations)

with the addition of the perfect gasses law necessary for the closure of the system: this is a system of coupled equations that, in principle, is able to describe the evolution of atmosphere.

## Eulerian and Lagrangian description

In general, in fluid mechanics there are two ways to describe a physical variables of a system: Eulerian and Lagrangian description.

Adopting Eulerian description, variables are evaluated with respect to a fixed point  $(x_1, x_2, x_3)$  in the space for every time; so, in Eulerian description, a variable  $u$  of a fluid system will be function of spatial coordinates and time.

In Lagrangian description indeed, individual fluid parcels belonging to the system are followed through time, so system variables depend on initial position of fluid parcels and on time. Let the position of a given fluid parcel at time  $t$  be  $\mathbf{r}(t)$ ; its velocity at time  $t$  is the Eulerian velocity  $\mathbf{u}$  evaluated at the current position  $\mathbf{r}(t)$  of the fluid parcel; this is also equal to the current time rate of change of the parcel position. Hence

$$\mathbf{u}(\mathbf{r}(t), t) = \frac{d\mathbf{r}}{dt} \quad (1.1)$$

In a similar fashion the acceleration of the parcel at time  $t$ , say  $\mathbf{a}(\mathbf{r}(t))$ , equals the second derivative of the position vector:

$$\mathbf{a}(\mathbf{r}(t), t) = \frac{d^2\mathbf{r}}{dt^2} \quad (1.2)$$

The connection between the Lagrangian and Eulerian pictures is made as follows. Let  $\mathbf{r} = (x_1, x_2, x_3)$  and  $\mathbf{u} = (u_1, u_2, u_3)$ . Considering, for example, the  $x_1$  component of Equation (1.1), we can write

$$\frac{dx_1}{dt} = u_1(x_1(t), x_2(t), x_3(t), t) \quad (1.3)$$

so, differentiating with respect to  $t$  once again

$$\begin{aligned} \frac{d^2x_1}{dt^2} &= \frac{\partial u_1}{\partial x_1} \frac{dx_1}{dt} + \frac{\partial u_1}{\partial x_2} \frac{dx_2}{dt} + \frac{\partial u_1}{\partial x_3} \frac{dx_3}{dt} + \frac{\partial u_1}{\partial t} = \\ u_1 \frac{\partial u_1}{\partial x_1} + u_2 \frac{\partial u_1}{\partial x_2} + u_3 \frac{\partial u_1}{\partial x_3} + \frac{\partial u_1}{\partial t} &= \frac{\partial u_1}{\partial t} + \mathbf{u} \cdot \nabla u_1 = \frac{du_1}{dt}; \end{aligned} \quad (1.4)$$

considering also other directions  $x_2$  and  $x_3$  we obtain the vector expression

$$\mathbf{a} = \frac{d^2\mathbf{r}}{dt^2} = \frac{\partial \mathbf{u}}{\partial t} + (\mathbf{u} \cdot \nabla) \mathbf{u} = \frac{d\mathbf{u}}{dt}. \quad (1.5)$$

In Equation (1.5) we have introduced the operator

$$\frac{d}{dt} = \frac{\partial}{\partial t} + \mathbf{u} \cdot \nabla \quad (1.6)$$

known as the material derivative or advective derivative. This represents the rate of change with respect to time following the motion (or following a blob) and should be contrasted to  $\partial/\partial t$ , the rate of change with respect to time at a fixed point ([Andrews, 2010](#)). This equation allows to pass from Lagrangian coordinates to Eulerian coordinates.

## Mass conservation

Let now consider a mass confined in a volume  $V$ . In absence of sources or sinks of mass in the volume  $V$ , mass variation in  $V$  is due to a mass flow (associated to a velocity vector  $\mathbf{u}$ ) through the surface  $S$  delimiting  $V$

$$-\frac{\partial}{\partial t} \int_V \rho dV = \int_S \rho \mathbf{u} \cdot \mathbf{n} dS \quad (1.7)$$

where  $\rho$  is the density and  $\mathbf{n}$  the unit vector normal to  $S$ . Assuming that  $V$  doesn't change in time, and applying the divergence theorem, we have

$$\int_V \left[ \frac{\partial \rho}{\partial t} + \nabla \cdot (\rho \mathbf{u}) \right] dV = 0; \quad (1.8)$$

equation above must be satisfied for every  $V$ , so we can write

$$\frac{\partial \rho}{\partial t} + \nabla \cdot (\rho \mathbf{u}) = 0. \quad (1.9)$$

This is the Eulerian form of continuity equation. Applying the operator (1.6), continuity Equation (1.9) can be rewrite as

$$\frac{d\rho}{dt} + \rho \nabla \cdot \mathbf{u} = 0 \quad (1.10)$$

Equation (1.10) represents the Lagrangian form of the continuity Equation (1.9).

### The equation of state

Since to a good approximation the atmosphere can be considered as a mixture of ideal gasses, the equation of state, in the case of dry air, is

$$p = R_a T \rho \quad (1.11)$$

where  $p$  is the pressure,  $T$  is the temperature,  $\rho$  the density and  $R_a$  is the gas constant per unit mass of dry air:  $R_a = 287 m^2 s^{-2} K^{-1}$ .

For moist air it is necessary to take into account the presence of water vapor, that, nevertheless is a minor constituent of the atmosphere, plays a crucial role in weather and climate processes. The water vapor content in the atmosphere can be quantified by specific humidity

$$q = \frac{m_v}{m} = \frac{\rho_v}{\rho} \quad (1.12)$$

that is the rate between water vapor mass  $m_v$  and humid air mass  $m = m_v + m_d$ , where  $m_d$  is the mass of dry air. Similarly are defined  $\rho_v = \frac{m_v}{V}$  and  $\rho = \rho_v + \rho_d$ , where  $\rho_d = \frac{m_d}{V}$ . Applying Dalton law, total pressure is the sum of dry air partial pressure and wet air partial pressure:

$$\begin{aligned} p = p_d + p_v &= \rho_d R_a T + \rho_v R_v T = \rho R_a T \left( \frac{\rho_d}{\rho} + 1.61 \frac{\rho_v}{\rho} \right) = \\ &= \rho R_a T (1 + 0.61q). \end{aligned} \quad (1.13)$$

with  $\frac{R_v}{R_a} = 1.61$ .

An analogous formulation of Equation (1.13) is

$$p = \rho R_a T_v \quad (1.14)$$

where  $T_v = T(1+0.61q)$  is called virtual temperature and is the temperature required in a dry atmosphere to have the same value of  $p/\rho$  as in an atmosphere with a specific humidity  $q$ . For typical atmospheric condition ( $q \sim 0.006 \text{ kg/kg}$ ) the difference between virtual and actual temperature is about  $1 \text{ K}$ .

It is to note that in presence of both water vapor both liquid water, we must take into account that

$$\rho = \rho_v + \rho_L + \rho_d \quad (1.15)$$

with  $\rho_L = \frac{m_L}{V}$ .

Equation (1.13), or the analogous formulation (1.14), is the diagnostic relation for atmospheric pressure.

## First law of thermodynamics

The conservation of energy adapted for a thermodynamic system states

$$\delta U = \delta Q - \delta W \quad (1.16)$$

where  $\delta U$  is the increase of internal energy of the system,  $\delta Q$  is the heat supplied or lost by the system and  $\delta W$  the amount of energy gained or lost as the result of work on the system. For a moving fluid parcel of unit mass, undergoing small changes  $\delta S$  of entropy,  $\delta U$  of internal energy and  $\delta V$  of volume in time  $\delta t$ , relation (1.16) can be written:

$$T\delta S = \delta U + p\delta V \quad (1.17)$$

or, for an ideal gas, as

$$T\delta S = c_p\delta T - \frac{1}{\rho}\delta p \quad (1.18)$$

with  $c_p$  specific heat at constant pressure ([Andrews, 2010](#)). Dividing Equation (1.18) for  $\delta t$  and considering  $\delta t \rightarrow 0$ , we obtain

$$Q \equiv T \frac{dS}{dt} = c_p \frac{dT}{dt} - \frac{1}{\rho} \frac{dp}{dt}; \quad (1.19)$$

if  $Q = 0$

$$\frac{dT}{dt} = \frac{1}{\rho c_p} \frac{dp}{dt} \quad (1.20)$$

and in the absence of diabatic heating, the temperature of a moving blob of air will increase if it moves to higher pressure (descends) and will decrease if it ascends. Another way of showing this is to note that, defining the potential temperature,  $\theta$ , as

$$\theta = T \left( \frac{p_0}{p} \right)^{\frac{R}{c_p}}. \quad (1.21)$$

that is the temperature that an air parcel, with an initial pressure  $p$ , reaches when is brought through an adiabatic process to a final pressure  $p_0$  usually taken as  $1 \times 10^5 \text{ Pa}$ , remains constant when the fluid parcel moves adiabatically:

$$\frac{d\theta}{dt} = 0. \quad (1.22)$$

In the lower and middle atmosphere the main physical processes contributing  $Q$  are latent heating and cooling, respectively from condensation and evaporation of water vapor, and radiative heating and cooling from absorption and emission of electromagnetic radiation ([Andrews, 2010](#)), so in presence of diabatic heating, Equation (1.22) becomes

$$\frac{d\theta}{dt} = S_\theta \quad (1.23)$$

or in Eulerian form

$$\frac{\partial \theta}{\partial t} + \mathbf{u} \cdot \nabla \theta = S_\theta \quad (1.24)$$

where the term  $S_\theta$  represents potential heat sources or sinks of heat mentioned above.

## The Navier-Stokes equations

Now we extend the momentum conservation equations to a fluid system, applying Newton second law to a small moving volume of fluid  $V$ . Since this fluid parcel is moving, this means that we are using the Lagrangian perspective; the variation of momentum is due to the sum of surface forces and volume forces acting on the volume itself

$$\int_V \rho \frac{du_i}{dt} dV = \int_S \mathbf{T}_i dS + \int_V \rho G_i dV, (i = 1, 2, 3). \quad (1.25)$$

In Equation (1.25)  $G_i$  represents volume forces (essentially gravity force), while  $\mathbf{T}_i$  is the  $i$ -th row of stress tensor

$$\begin{pmatrix} \tau_{11} & \tau_{12} & \tau_{13} \\ \tau_{21} & \tau_{22} & \tau_{23} \\ \tau_{31} & \tau_{32} & \tau_{33} \end{pmatrix}$$

in which  $\tau_{ij} = \tau_{ji}$  as is a symmetric tensor.

Applying the divergence theorem to the first right hand term in Equation (1.25)

$$\int_S \mathbf{T}_i dS = \int_V \nabla \cdot \mathbf{T}_i dV \quad (1.26)$$

and substituting in Equation (1.25), we obtain

$$\rho \frac{du_i}{dt} = \nabla \cdot \mathbf{T}_i + \rho G_i; \quad (1.27)$$

for a viscous and Newtonian fluid like air, being  $\mu$  the dynamic viscosity, we can write stress tensor as ([Salby , 2012](#)):

$$\tau_{ij} = -p\delta_{ij} + \sigma_{ij} \quad (1.28)$$

where, adopting Einstein notation,

$$\sigma_{ij} = \mu \left[ \left( \frac{\partial u_i}{\partial x_j} + \frac{\partial u_j}{\partial x_i} \right) - \frac{2}{3} \delta_{ij} \left( \frac{\partial u_\alpha}{\partial x_\alpha} \right) \right]. \quad (1.29)$$

Substituting Equation (1.28) in Equation (1.27) we get the final form

$$\frac{du_i}{dt} = -\frac{1}{\rho} \frac{\partial p}{\partial x_i} + \nu \frac{\partial^2 u_i}{\partial x_\alpha^2} + \frac{1}{3} \nu \frac{\partial^2 u_\alpha}{\partial x_i \partial x_\alpha} + G_i \quad (1.30)$$

putting  $\nu = \mu/\rho$ . Here the first right hand term represents the forces related to pressure gradient, the second and the third, the forces related to viscous friction while  $\mathbf{G}$  is the gravity force. It is to note that in incompressible case  $\partial u_\alpha/\partial x_\alpha = 0$ , and consequently the third right hand term in Equation (1.30) is null.

Let consider now a non inertial frame of reference, in particular a rotating frame, as in the case of the Earth. In this case it is necessary transform Equation (1.30) according

$$\mathbf{v} = \mathbf{V} + \boldsymbol{\Omega} \times \mathbf{R} \quad (1.31)$$

and

$$\frac{d}{dt}_{inertial} = \frac{d}{dt} + \boldsymbol{\Omega} \times \quad (1.32)$$

where  $\mathbf{v}$  is the velocity in the inertial frame,  $\mathbf{V}$  is the velocity in the rotating frame,  $\boldsymbol{\Omega}$  is the angular velocity of the rotating frame and  $\mathbf{R}$  is the position vector referred to the rotating frame.

We can write

$$\frac{d\mathbf{v}}{dt}_{inertial} = \frac{d\mathbf{V}}{dt} + 2\boldsymbol{\Omega} \times \mathbf{V} + \boldsymbol{\Omega} \times (\boldsymbol{\Omega} \times \mathbf{R}); \quad (1.33)$$

the second right hand term is the Coriolis acceleration, while the third right hand term is the centrifugal acceleration. Incorporating the centrifugal acceleration in the gravitational term

$$\mathbf{g} = \mathbf{G} - \boldsymbol{\Omega} \times (\boldsymbol{\Omega} \times \mathbf{R}) \quad (1.34)$$

and rewriting the Coriolis term according

$$2(\boldsymbol{\Omega} \times \mathbf{V})_i = 2\epsilon_{i\alpha\beta}\omega_\alpha u_\beta \quad (1.35)$$

with  $\omega_\alpha$  and  $u_\beta$  the component of  $\boldsymbol{\Omega}$  and  $\mathbf{V}$  respectively and  $\epsilon_{i\alpha\beta}$  the Levi-Civita tensor, we arrive to the final form for the momentum conservation equations in a rotating frame

$$\frac{du_i}{dt} = -\frac{1}{\rho} \frac{\partial p}{\partial x_i} + \nu \frac{\partial^2 u_i}{\partial x_\alpha^2} + \frac{1}{3} \nu \frac{\partial^2 u_\alpha}{\partial x_i \partial x_\alpha} + g\delta_{i3} - 2\epsilon_{i\alpha\beta}\omega_\alpha u_\beta \quad (1.36)$$

or, in vector form and in Eulerian coordinates

$$\frac{\partial \mathbf{u}}{\partial t} + (\mathbf{u} \cdot \nabla) \mathbf{u} = -\frac{1}{\rho} \nabla p + \nu \nabla^2 \mathbf{u} + \frac{1}{3} \nu \nabla (\nabla \cdot \mathbf{u}) + g\mathbf{k} - 2\boldsymbol{\Omega} \times \mathbf{u}. \quad (1.37)$$

For an incompressible flow, from continuity Equation (1.9) results  $\nabla \cdot \mathbf{u} = 0$ , so Equation (1.37) becomes

$$\frac{\partial \mathbf{u}}{\partial t} + (\mathbf{u} \cdot \nabla) \mathbf{u} = -\frac{1}{\rho} \nabla p + \nu \nabla^2 \mathbf{u} + g\mathbf{k} - 2\boldsymbol{\Omega} \times \mathbf{u}. \quad (1.38)$$

### 1.3 Geostrophic approximation

Under appropriate dynamical conditions we can simplify Equations (1.36) using the scale analysis method, that is, evaluate the order of magnitude

Table 1.2: Some scales for large scale motion in the atmosphere. Table from Andrews, D. G., *An introduction to Atmospheric Physics*, Cambridge University Press, second edition (2010).

Scale	Symbol	Typical magnitude
Horizontal scale	$L$	$10^6 \text{ m}$
Vertical scale	$H$	$10^4 \text{ m}$
Horizontal velocity	$U$	$10 \text{ m/s}$
Vertical velocity	$W$	$10^{-2} \text{ m/s}$
Timescale	$U/L$	$10^5 \text{ s}$
Surface density	$\rho$	$1 \text{ kg/m}^3$
Earth radius	$a$	$6.4 \times 10^6 \text{ m}$
$2 \times$ rotation rate	$2\Omega$	$10^{-4} \text{ s}^{-1}$
Acceleration of gravity	$g$	$10 \text{ m/s}^{-2}$

of equations terms, in order to neglect smaller terms.

Let consider, for example, motions associated with mid-latitudes large-scale weather systems with the time and space scales given in Table 1.2. Through values reported in Table 1.2, assuming incompressibility of air (if one considers regions whose heights are much smaller than the density scale-height, about  $10 \text{ km}$  (Andrews, 2010), and that do not host large temperature gradients) and cinematic viscosity of air  $\nu \approx 10^{-5} - 10^{-6} \text{ m}^2/\text{s}$ , we can simplify Equations (1.36) taking into account only terms  $> 10^3$ . Starting from horizontal components of Equations (1.36), we obtain

$$\begin{aligned} -\frac{1}{\rho} \frac{\partial p}{\partial x_1} &= -f u_2 \\ -\frac{1}{\rho} \frac{\partial p}{\partial x_2} &= f u_1 \end{aligned} \tag{1.39}$$

where  $f$  is the local Coriolis parameter  $f = 2\Omega \sin \phi$ , with  $\phi$  being considered latitude. These equations represent geostrophic approximation: the horizontal pressure gradients are balanced by Coriolis forces associated with the horizontal winds and are valid if it is possible to neglect temporal derivatives of horizontal velocities in Equations (1.36). In other words, geostrophic approximation is valid if Rossby number, defined as the ratio between inertial terms and centrifugal terms

$$R_o = \frac{U}{fL} \tag{1.40}$$

where where  $U$  and  $L$  are, respectively, characteristic velocity and length scales of the phenomenon, is much less than 1 ( $R_o \ll 1$ ); if this condition is not valid, we obtain quasi-geostrophic equations:

$$\begin{aligned}\frac{du_1}{dt} &= -\frac{1}{\rho} \frac{\partial p}{\partial x_1} + fu_2 \\ \frac{du_2}{dt} &= -\frac{1}{\rho} \frac{\partial p}{\partial x_2} - fu_1.\end{aligned}\tag{1.41}$$

Applying scale analysis to vertical component of Equations (1.36), because temporal variation of vertical velocity is of the order of  $10^{-7} \text{ m/s}^{-2}$ , equation reduces to

$$\frac{\partial p}{\partial x_3} = -g\rho\tag{1.42}$$

This shows that, under our assumed scaling, the vertical momentum equation reduces to hydrostatic balance. For a large number of phenomena Equation (1.42) is a good approximation of vertical momentum equation, but in cases in which it is not possible to neglect vertical acceleration, as in the case of convection, not hydrostatic equations are necessary.

In case geostrophic balance is valid at each height the horizontal wind blows along the isobars (the lines of constant pressure):

$$(u_1, u_2, 0) \cdot \nabla p = \frac{1}{\rho f} \left( -\frac{\partial p}{\partial x_2} \mathbf{i} + \frac{\partial p}{\partial x_1} \mathbf{j} \right) \cdot \left( \frac{\partial p}{\partial x_1} \mathbf{i} + \frac{\partial p}{\partial x_2} \mathbf{j} \right) = 0,\tag{1.43}$$

so in presence of a pressure minimum (Low) we have a cyclonic circulation, while in presence of a pressure maximum (High), we have an anti-cyclonic circulation (Figure 1.2).

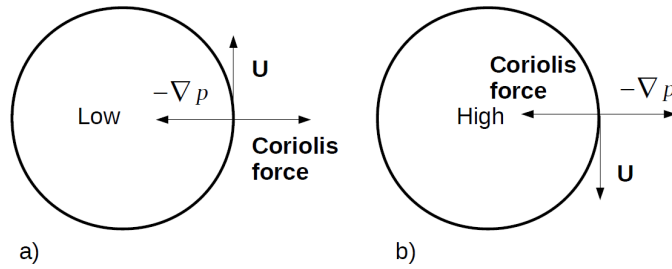


Figure 1.2: Cyclonic, a), and anticyclonic, b), circulation.

## 1.4 Averaged conservation equations

The Section 1.2 has presented the fundamental hydrodynamical equations that govern atmospheric motions and their velocity, pressure and temperature distributions. Given initial observed fields of mass, velocity and temperature, in principle it is possible to determine the mass, the velocity and the temperature distributions at any future time by solving the hydrodynamical equations as an initial value problem. Although these non-linear partial differential equations do not have analytic or closed solutions, they can be integrated by numerical methods to yield a forecast of the meteorological variables for a future time; an introduction at these methods will be treated in the next chapter.

Fundamental equations presented in Section 1.2 are defined in term of differential operators, and thus in term of mathematical formalism are valid only in the limit when spatial and temporal increments  $\delta x_i$  and  $\delta t$  approach zero. In terms of practical applications, however they are valid only when the spatial increments  $\delta x_i$  are much larger than the spacing between molecules, but are small enough so that the differential terms over these distances and over the time  $\delta t$  can be represented accurately by a constant (*Pielke*, 2002). Formally if

$$l_m \ll \delta x_1, \delta x_2 \text{ and } \delta x_3 \quad (1.44)$$

where  $l_m$  is the representative spacing between molecules, and if

$$\frac{\partial \rho u_i}{\partial x_i} \gg \frac{\delta x_i}{2} \frac{\partial^2 \rho u_i}{\partial x_i^2}, \quad i = 1, 2, 3; \quad \frac{\partial \rho}{\partial t} \gg \frac{\delta t}{2} \frac{\partial^2 \rho}{\partial t^2} \quad (1.45)$$

the use of Equations (1.9), (1.24) and (1.38) is justified.

In the atmosphere the criteria given by (1.44) and (1.45) limit the direct application of Equations (1.9), (1.24) and (1.38) to space scales on order of about a centimeter and to time scales of order of a second. Therefore, to use Equations (1.9), (1.24) and (1.38) to represent the atmosphere accurately, these equations must be evaluated over those space and time intervals. This fact reduces remarkable the possibility of application of Equations (1.9), (1.24) and (1.38) in order to predict evolution of atmosphere, inasmuch, for example, to solve mesoscale circulation, that is characterized by horizontal scales on the order of 10 to 100 km, and vertical size of about 10 km, it is

necessary to solve these equations at  $10^{18} - 10^{20}$  locations, exceeding the capacity of any existing computer system.

To overcome this problem it is necessary to integrate fundamental equations over larger spatial and temporal scales, in order to reduce the computational effort. Reducing spatial and temporal scales over which perform integration however introduces errors in the solution of the equations due to the impossibility of simulate phenomena under the resolution adopted. To circumvent this problem, in general, defined a scale on which solve equations, it is necessary to parameterize the effect that subscales phenomena produce on considered scale: major phenomena that require parameterization in a weather simulation will be presented in the following of this thesis. So, in order to perform integration, it is convenient to decompose any dependent variables  $\phi$  of Equations (1.9), (1.24) and (1.38) according

$$\phi = \bar{\phi} + \phi' \quad (1.46)$$

where  $\bar{\phi}$  represents the time average of  $\phi$  over the finite time increment  $\Delta t$

$$\bar{\phi} = \frac{1}{\Delta t} \int_t^{t+\Delta t} dt. \quad (1.47)$$

The variable  $\phi'$  instead is the subgrid scale deviation from the averaged value.

To simplify Equations (1.9), (1.24) and (1.38), after the introduction of the scales separation of dependent variables (1.46), it is convenient to assume that the averaged variables  $\bar{\phi}$  change much more slowly in time than do the perturbations  $\phi'$ , i.e.  $\bar{\phi}$  is approximately constant, while the average of the fluctuation  $\bar{\phi}'$  is zero: this last assumption is commonly called Reynolds assumption (*Pielke*, 2002).

With Reynolds assumption and exploiting rule for time-averaging

$$\overline{\frac{\partial \phi}{\partial x_i}} = \frac{1}{\Delta t} \int_t^{t+\Delta t} \frac{\partial \phi}{\partial x_i} dt = \frac{\partial}{\partial x_i} \frac{1}{\Delta t} \int_t^{t+\Delta t} \phi dt = \frac{\partial \bar{\phi}}{\partial x_i} \quad (1.48)$$

$$\overline{\frac{\partial \phi'}{\partial x_i}} = \frac{1}{\Delta t} \int_t^{t+\Delta t} \frac{\partial \phi'}{\partial x_i} dt = \frac{\partial}{\partial x_i} \frac{1}{\Delta t} \int_t^{t+\Delta t} \phi' dt = 0 \quad (1.49)$$

$$\overline{\bar{f}} = \bar{f}, \quad \overline{\bar{f} + \bar{g}} = \bar{f} + \bar{g},$$

$$\overline{\bar{f} \cdot \bar{g}} = \bar{f} \cdot \bar{g}, \quad \overline{\frac{\partial f}{\partial s}} = \frac{\partial \bar{f}}{\partial s}, \quad (1.50)$$

$$\overline{\int f ds} = \int \bar{f} ds, \quad \overline{f \cdot g} \neq \bar{f} \cdot \bar{g}$$

it is possible to obtain the Reynolds-averaged form of Equations (1.9), (1.24) and (1.38).

Considering the  $x_1$  component of Navier-Stokes Equations (1.38) for incompressible flow, introducing the scales separation (1.46) and averaging on time, we can write

$$\begin{aligned} & \frac{\partial(\bar{u}_1 + u'_1)}{\partial t} + \frac{\partial(\bar{u}_1 + u'_1)^2}{\partial x_1} + \frac{\partial(\bar{u}_1 + u'_1)(\bar{u}_2 + \bar{u}'_2)}{\partial x_2} + \frac{\partial(\bar{u}_1 + u'_1)(\bar{u}_3 + \bar{u}'_3)}{\partial x_3} \\ &= -\frac{1}{\rho} \frac{\partial(\bar{p} + p')}{\partial x_1} + \nu \left( \frac{\partial^2(\bar{u}_1 + u'_1)}{\partial x_1^2} + \frac{\partial^2(\bar{u}_1 + u'_1)}{\partial x_2^2} + \frac{\partial^2(\bar{u}_1 + u'_1)}{\partial x_3^2} \right) + \\ & \quad -2(\Omega_2(\bar{u}_3 + u'_3) + \Omega_3(\bar{u}_2 + u'_2)) \end{aligned} \quad (1.51)$$

From application of Equations (1.48) - (1.50) to Equation (1.51), we get

$$\begin{aligned} & \frac{\partial\bar{u}_1\bar{u}_1}{\partial t} + \frac{\partial\bar{u}_1}{\partial x_1} + \frac{\partial\bar{u}'_1\bar{u}'_1}{\partial x_1} + \frac{\partial\bar{u}_1\bar{u}_2}{\partial x_2} + \frac{\partial\bar{u}'_1\bar{u}'_2}{\partial x_2} + \frac{\partial\bar{u}'_1\bar{u}'_3}{\partial x_3} + \frac{\partial\bar{u}_1\bar{u}_3}{\partial x_3} \\ &= -\frac{1}{\rho} \frac{\partial\bar{p}}{\partial x_1} + \nu \left( \frac{\partial^2\bar{u}_1}{\partial x_1^2} + \frac{\partial^2\bar{u}_1}{\partial x_2^2} + \frac{\partial^2\bar{u}_1}{\partial x_3^2} \right) - 2(\Omega_2\bar{u}_3 + \Omega_3\bar{u}_2). \end{aligned} \quad (1.52)$$

Exploiting the continuity equation and considering also other directions, we obtain the final form for the Reynolds averaged Navier-Stokes equations

$$\begin{aligned} & \frac{\partial\bar{u}_1}{\partial t} + \bar{u}_1 \frac{\partial\bar{u}_1}{\partial x_1} + \bar{u}_2 \frac{\partial\bar{u}_1}{\partial x_2} + \bar{u}_3 \frac{\partial\bar{u}_1}{\partial x_3} = -\frac{1}{\rho} \frac{\partial\bar{p}}{\partial x_1} + \nu\Delta\bar{u}_1 + \\ & \quad - \left( \frac{\partial\bar{u}'_1\bar{u}'_1}{\partial x_1} + \frac{\partial\bar{u}'_1\bar{u}'_2}{\partial x_2} + \frac{\partial\bar{u}'_1\bar{u}'_3}{\partial x_3} \right) - 2(\Omega_2\bar{u}_3 + \Omega_3\bar{u}_2) \\ & \frac{\partial\bar{u}_2}{\partial t} + \bar{u}_1 \frac{\partial\bar{u}_2}{\partial x_1} + \bar{u}_2 \frac{\partial\bar{u}_2}{\partial x_2} + \bar{u}_3 \frac{\partial\bar{u}_2}{\partial x_3} = -\frac{1}{\rho} \frac{\partial\bar{p}}{\partial x_2} + \nu\Delta\bar{u}_2 + \\ & \quad - \left( \frac{\partial\bar{u}'_1\bar{u}'_2}{\partial x_1} + \frac{\partial\bar{u}'_2\bar{u}'_2}{\partial x_2} + \frac{\partial\bar{u}'_2\bar{u}'_3}{\partial x_3} \right) + 2(\Omega_1\bar{u}_3 + \Omega_3\bar{u}_1) \\ & \frac{\partial\bar{u}_3}{\partial t} + \bar{u}_1 \frac{\partial\bar{u}_3}{\partial x_1} + \bar{u}_2 \frac{\partial\bar{u}_3}{\partial x_2} + \bar{u}_3 \frac{\partial\bar{u}_3}{\partial x_3} = -\frac{1}{\rho} \frac{\partial\bar{p}}{\partial x_3} + \nu\Delta\bar{u}_3 + \\ & \quad - \left( \frac{\partial\bar{u}'_1\bar{u}'_3}{\partial x_1} + \frac{\partial\bar{u}'_2\bar{u}'_3}{\partial x_2} + \frac{\partial\bar{u}'_3\bar{u}'_3}{\partial x_3} \right) - 2(\Omega_1\bar{u}_2 + \Omega_2\bar{u}_1) - \rho g \end{aligned} \quad (1.53)$$

Proceeding in a similar manner it is possible to obtain the Reynolds-averaged form of continuity equation (1.9) and of potential temperature equation (1.24)

$$\frac{\partial\bar{u}_1}{\partial x_1} + \frac{\partial\bar{u}_2}{\partial x_2} + \frac{\partial\bar{u}_3}{\partial x_3} = 0 \quad (1.54)$$

$$\begin{aligned} \frac{\partial \bar{\theta}}{\partial t} = & - \left( u_1 \frac{\partial \bar{\theta}}{\partial x_1} + u_2 \frac{\partial \bar{\theta}}{\partial x_2} + u_3 \frac{\partial \bar{\theta}}{\partial x_3} \right) + \\ & - \frac{1}{\rho} \left( \frac{\partial}{\partial x_1} \overline{u'_1 \theta'} + \frac{\partial}{\partial x_2} \overline{u'_2 \theta'} + \frac{\partial}{\partial x_3} \overline{u'_3 \theta'} \right) + \bar{S}_\theta. \end{aligned} \quad (1.55)$$

Equations (1.53) - (1.55) are the basis for many meteorological numerical models: an introduction of these models will be presented in the next chapter.

The complete set of equations for the mean flow (1.53) - (1.55), unlike the equations for the total flow (1.9), (1.24) and (1.38) is not a closed set, as in addition to the five unknown mean variables  $\bar{u}_1$ ,  $\bar{u}_2$ ,  $\bar{u}_3$ ,  $\bar{\theta}$  and  $\bar{p}$ , are unknown also the the subgrid scale fluctuations  $u'_1$ ,  $u'_2$ ,  $u'_3$ ,  $\theta'$  and  $p'$ . To solve these equations closure assumptions must be done to approximate the unknown fluxes in terms of the five mean state variables; varying the scale over which are evaluated the mean values of variables, vary the phenomena that are not explicitly solved by equations and that must be parameterized in order to take into account their effect on explicitly resolved variables.

# Chapter 2

## Numerical weather prediction

### 2.1 Introduction

As anticipated in the previous chapter, the set of nonlinear, partial differential equations (1.9), (1.24) and (1.38) cannot to be solved using known analytic methods, but requires numerical methods of computation where the equations are discretized and solved on a lattice.

A pioneering attempt to predict the weather by numerical integration was made by L. F. Richardson during World War I (*Richardson* , 1922).

Richardson showed how the differential equations governing atmospheric motions could be written approximately as a set of algebraic difference equations for values of the tendencies of various field variables at a finite number of points in space. Given the observed values of the field variables at these grid points, the tendencies could be calculated numerically by solving the algebraic difference equations. By extrapolating the computed tendencies ahead a small increment in time, an estimate of the fields at a short time in the future could be obtained. The new values of the field variables could then be used to recompute the tendencies, which could in turn be used to extrapolate further ahead in time, and so on. Richardson worked out one example forecast for surface pressure tendencies at two grid points. Unfortunately, the results were very poor also due to the poor initial data available (*Holton* , 2004).

After World War II interest in numerical prediction revived due partly to the vast expansion of the meteorological observation network, which provided much improved initial data, but even more importantly to the

development of digital computers, which made the enormous volume of arithmetic operations required in a numerical forecast feasible.

## 2.2 Methods of solutions

There are several broad classes of solution techniques available to represent terms involving the derivatives of fundamental equations including

- finite difference schemes, which utilize a form of truncated Taylor expansion;
- spectral techniques, in which dependent variables are transformed to wave number space using a global basis function (e.g, a Fourier transform);
- pseudo-spectral methods, which use truncated spectral series;
- finite element schemes, which seek to minimize the error between the actual and the approximate solutions using a local basis function; and
- interpolation schemes, in which polynomials are used to approximate the dependent variables.

In the following, in order to introduce problems related to numerical solution of partial differential equations, it will be discussed the finite difference method inasmuch is one of the most common methods used in numerical weather simulations.

### Finite difference schemes

The finite difference method consists in replacing derivatives in the differential equations with finite difference approximations at a discrete set of points in space and in time. The resulting equations can then be solved by algebraic methods. Taylor series may be used to establish appropriate finite difference approximations to derivatives:

$$f(x \pm \Delta x) = f(x) \pm f'(x)\Delta x + f''(x)\frac{\Delta x^2}{2!} \pm f'''(x)\frac{\Delta x^3}{3!} + \dots \quad (2.1)$$

from which, for example stopping to second order, it is possible to obtain

$$f'(x) = \frac{f(x + \Delta x) - f(x)}{\Delta x} + R \quad \text{forward difference} \quad (2.2)$$

$$f'(x) = \frac{f(x) - f(x - \Delta x)}{\Delta x} + R \quad \text{backward difference} \quad (2.3)$$

where the term of highest order in  $R$  is  $f''(x)\Delta x/2$ . In these cases we refer to the approximation for the derivative  $f'(x)$  as a forward difference (if  $\Delta x > 0$ ), or as backward difference (if  $\Delta x < 0$ ) of order  $\Delta x$  ( $O(\Delta x)$ ):  $\Delta x$  represents the truncation error of the finite difference approximation.

If the Equation (2.3) is subtracted from Equation (2.2), we obtain the

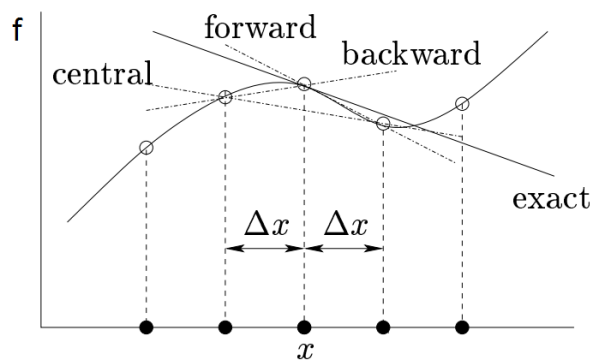


Figure 2.1: Geometric interpretation of backward, forward and centered difference methods.

centered difference approximation for  $f'(x)$

$$f'(x) = \frac{f(x + \Delta x) - f(x - \Delta x)}{2\Delta x} + O(\Delta x^2) \quad \text{centered difference.} \quad (2.4)$$

In this case the truncation error is of order  $\Delta x^2$ , giving more accurate approximation than in forward or backward cases. In Figure 2.3 the geometric interpretation of backward, forward and centered difference methods is represented.

Since wavelike motions are characteristic of the atmosphere it is of interest to apply the centered difference approximation for  $f'(x)$  to a simple harmonic function  $f(x) = A \sin(2\pi x/L)$ . The ratio between the finite difference approximation  $f'_D(x)$  and the true value of  $f'(x)$  is

$$\frac{f'_D(x)}{f'(x)} = \frac{\sin(2\pi\Delta x/L)}{2\pi\Delta x/L}; \quad (2.5)$$

it is evident that the finite difference approximation approaches the true value of  $f'(x)$  when  $\Delta x/L$  approaches zero: so the truncation error will be small when  $\Delta x$  is small compared to  $L$  (*Haltiner and Williams*, 1992).

By contrast, the shortest wave that can be resolved on a finite difference grid has a wavelength of two grid increments; if  $L = 2\Delta x$

$$\frac{f'_D(x)}{f'(x)} = \frac{\sin \pi}{\pi} = 0 \quad (2.6)$$

so that the representation given by Equation (2.4) fails to resolve features that have wavelengths of two grid increments. Thus the representation of derivatives of a function using values at neighboring grid points provides very poor representation of short waves relative to the grid mesh  $\Delta x$ , whereas longer waves are reasonably well resolved. The ability, or lack of a numerical scheme to resolve features of different wavelengths properly is a crucial consideration in the use of a numerical approximation scheme.

In an analog manner finite differencing is also used to advance from one time step to another. As with spatial finite differencing, there exist multiple methods for temporal finite differencing, each with its own accuracy and numerical considerations.

Regarding the forecast of atmospheric evolution by means of numerical models (Numerical Weather Prediction, NWP) the choice of grid resolution is strictly relate to the atmospheric scales we want to explicitly resolve; once the grid spacing is fixed, the choice of the time step is limited by the stability of the solution. The stability of differencing schemes is limited by a non-dimensional value, known as Courant number (*Haltiner and Williams*, 1992)

$$C = U \frac{\Delta t}{\Delta x} \quad (2.7)$$

where  $U$  is the translation speed of the fastest feature or wave on the model grid,  $\Delta x$  is the horizontal grid spacing, and  $\Delta t$  is the time step. Generally speaking,  $U$  is determined by the prevailing meteorology while  $\Delta x$  is determined by the horizontal scales of the features that one desires to resolve on the model grid. The limiting value of the Courant number is known as the *CFL* condition, representing the maximum value of the Courant number that permits numerically-stable model solutions. The exact value of the *CFL* condition varies depending upon the spatial and temporal

scheme utilized; however, a general guideline is that  $C \leq 1$ ; so knowing the value of  $C$ ,  $U$  and  $\Delta x$ , it is possible to choose the time step  $\Delta t$ .

## 2.3 Parameterizations

As shown in previous section, it is possible to formally solve primitive Equations (1.9), (1.24) and (1.38) for resolved scales of motion, which depend on the grid spacing  $\Delta x$  chosen. But, though it is not possible to resolve them, the unresolved scales are not unimportant. Indeed they are interconnected with the resolved scales and it is necessary to account for what occurs on the unresolved scales with what are known as parameterizations. To first order, a parameterization approximates unresolved scales as a function of known or hypothesized relationships that they have with resolved scales, i.e. parameterization involves the representation of a process in term of its known relationship to dependent variables resolved on the model grid. Many ways that each process or set of processes can be parameterized exist, each with their own assumptions, strengths, weaknesses, and level of complexity. Anyway parameterizations are approximations and thus a major contributor to model error along with uncertainties in the initial conditions and imperfect numerical methods.

Beside scales, two other primary reasons to employ a parameterization exist: complexity, i.e. a process or a set of processes can be resolved on the model grid, but doing so would be computationally expensive, or lack of knowledge of the process, that is, it is not known enough about the relevant process or set of processes in order to develop solvable equations to resolve the process or set of processes. Anyway problems involving scales are by far the primary reason for parameterizations within modern models.

The most common processes that are parameterized by modern numerical models include the planetary boundary and surface layers, cumulus convection (particularly for coarser models), cloud microphysics, and radiation. In the following, most common parameterizations adopted in a NWP will be introduced.

## Microphysics

The most common way to form clouds on Earth is by lifting: as moist air rises, it cools and eventually becomes saturated, at which point a cloud forms. Lifting mechanisms in the atmosphere are four: convective lifting, when air lifting is stimulated by local surface heating, convergent lifting, when different direction air flows interact, orographic lifting, when air is forced over a barrier such as a mountain, and frontal lifting, when air lifting occurs along the leading of contrasting air masses (cold and warm fronts); all these mechanisms are generally rapid enough that air parcels are lifted adiabatically: the level at which a parcel adiabatically lifted from near the surface first reaches saturation is called the lifting condensation level, LCL. If the parcel is lifted further, a cloud forms.

Processes controlling the formation of cloud droplets and ice crystals, their growth and fallout as precipitation are known as microphysical processes; Microphysics parameterization schemes play a key role in cloud, climate and weather models and they must take into account a big number of phenomena that occur within a cloud such as latent heating/cooling due to change of phase of hydrometeors present in clouds, fallout of larger particles (precipitation), radiative transfer due to interaction between radiation and hydrometeors, cloud-aerosol-precipitation interaction, etc; all these phenomena occur on scales that are never explicitly resolved by common NWP models, so they need to be parameterized.

In general the complexity of a microphysics parameterization scheme depends on one hand to the number of ways in which water is categorized (for example, vapor, cloud droplets, rain, snow, etc.) and to the number of processes allowed from a category to another (see for example Figure 2.2) and on the other hand to the way in which hydrometeors size distributions are represented. Size distributions of hydrometeors present in a cloud are a crucial point in microphysics parameterization schemes inasmuch as growth rate, rate of conversion between a class of hydrometeors to another (and consequently the amount of latent heat released or adsorbed), sedimentation speed, and finally, precipitation, are strictly related to particles dimension. According to the way of size distributions representation, microphysics parameterization schemes can be divided into two broad categories: spectral schemes if microphysical particles size distribution is divided into bins for different sizes and the evolution of each bin is computed separately, and

bulk schemes if the scheme predicts evolution of one or more bulk quantities assuming some semi-empirical functional form for the particles size distribution (e.g. gamma distribution).

Depending on the number of bulk quantities taken into account, bulk

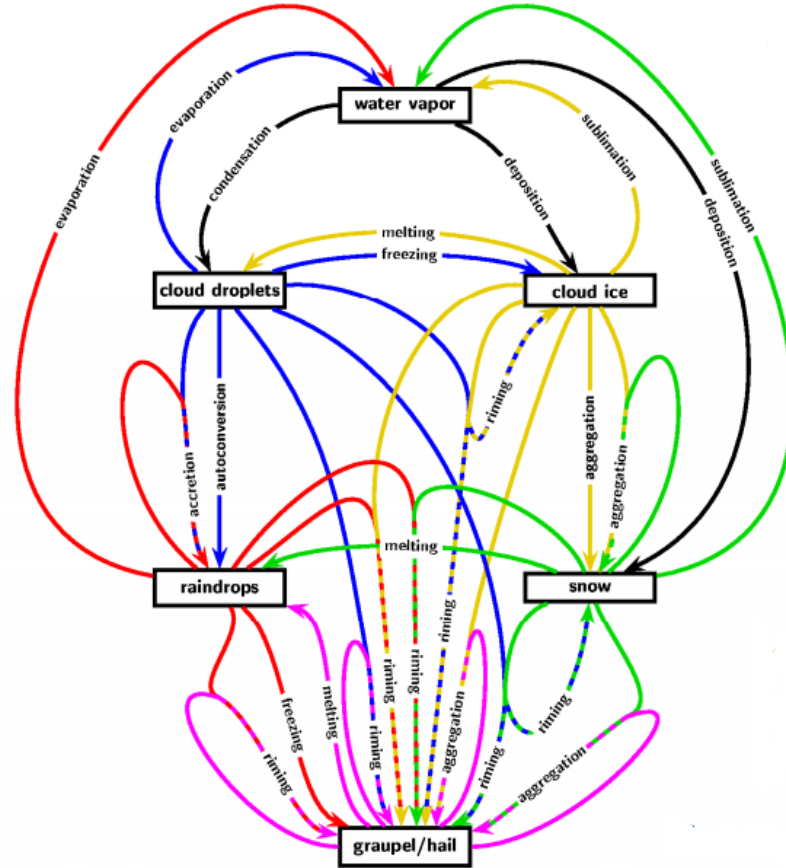


Figure 2.2: Example of hydrometeors and their interactions taken into account in a microphysics parameterization scheme.

schemes are further divided into one-moment and two-moment schemes. In the case of one-moment schemes, for each hydrometeor, only the evolution of mixing ratio is calculated, while for two-moment schemes also evolution of concentration number is calculated.

Usually in NWP bulk parameterization schemes are utilized inasmuch spectral schemes involve a prognostic equation for the evolution of each distribution bin, resulting in a larger number of equations to solve in comparison

to bulk schemes.

## Cumulus

When grid spacing is too large in order to explicitly resolve convection (typical cumulus dimensions are of order of some kilometers), that is when resolution not allows to correctly represent convective phenomena responsible for cumulus development, it is not possible to explicitly resolve water vapor, clouds and precipitation processes involved in microphysics parameterization schemes. In this case it is necessary to determine the statistical effect that the development of this kind of clouds have on resolved scales. The main effect on large scale due to convection is an alteration of temperature and moisture vertical profiles because of sub-scale convective fluxes and precipitations; therefore convection parameterization must take into account two principal aspects: the regulation of the amount of convection by large scale variables in order to define (generally using an additional triggering function) where, when and how strong convection is active, and the regulation of the large scale variables by convection, i.e. evaluate the feedback induced by convection on explicitly resolved variables ([Arakawa, 2004](#); [Yano et al., 2013](#)).

During the years many convection parameterization schemes have been developed, among which, most adopted are Kuo method ([Kuo, 1974](#)), Anthes scheme ([Anthes, 1977](#)) and Kain-Fritsch scheme ([Kain and Fritsch, 1992](#); [Kain, 2004](#)).

## Planetary boundary layer

The Planetary Boundary Layer, PBL, is the portion of the atmosphere in which the flow is strongly influenced by interaction with the surface of the Earth. Ultimately this interaction depends on molecular viscosity. Within the few millimeters of the surface, vertical shears are very intense, and in this layer of the atmosphere molecular diffusion is comparable to other forces in the momentum equation. Outside of this viscous sublayer molecular viscosity is too small to influence the dynamics directly and is not important in the boundary layer equations for the mean wind, al-

though it is still important for small scale turbulent eddies. The sources of the turbulence are both strong vertical wind shear and convection. The shear-induced eddies, together with convective eddies caused by surface heating, are very effective in transferring momentum to the surface and in transferring heat (latent and sensible) away from the surface at rates many orders of magnitude larger than can be done by molecular processes. The depth of the PBL produced by this turbulent transport may range from as little as 30 *m* in conditions of large static stability to more than 3 *km* in highly convective conditions. On average, at mid-latitudes, the PBL extends through the lowest one kilometer of the atmosphere, and contains about 10% of the mass of the atmosphere ([Holton , 2004](#)).

Basically there are two approaches that may be used to represent the PBL in a numerical model. The first way is to provide sufficient levels near the earth surface to resolve boundary layer adequately. Then the evolution of the meteorological variables is explicitly predicted by including the necessary closure assumptions and terms representing momentum, heat and moisture fluxes in the governing equations. The accuracy of such simulations will depend on how well the turbulent fluxes are specified. Pure molecular analogy may not be entirely satisfactory especially with an unstable surface layer because convective plumes will develop that transport heat and moisture differently than Fickian diffusion. This suggests that a complete treatment of the boundary layer should be combined with the treatment of convection. Despite unstable case is more complex to describe, also stable case presents difficult problems. In any case it is not known whether the turbulent fluxes can be predicted accurately enough level by level to provide a good structure throughout the PBL, especially since data are generally insufficient to provide initial conditions. Anyway, for large scale NWP the exchange of energy between the PBL and the atmosphere above may be more important than details within the PBL.

The second approach is to represent, or parameterize, not only the small scale turbulent fluxes but also the entire vertical structure of the PBL in terms of one or two layers. From this parameterization key variables such as the wind, temperature, etc., at any desired level, as well as the momentum, heat and moisture fluxes from the surface, etc., may be extracted. Such a parameterization assumes the boundary layer to be quasi-stationary, implying that the response of PBL to large scale forcing is very rapid. The

parameterization approach gives a less detailed representation than the first approach, but it is far cheaper in computer time and it may be sufficiently accurate for many purposes (*Haltiner and Williams* , 1992).

## **Radiation**

Ultimately, the primary factor driving the atmosphere is the differential solar (short wave) radiation between the poles and the equator. But the actual radiational heating of the atmosphere depends on the difference between the incoming (solar) and the outgoing (terrestrial, long wave) radiations, which depends on many factors, such as temperature, clouds, water vapor, carbon dioxide, ozone, dust, etc. The processes involved are very complex and a detailed treatment for purposes of weather forecasting would require an enormous amount of computer time. Consequently, approximate solutions are sought that are realistic in terms of objectives of a numerical prediction or simulation model.

The atmospheric long radiation with wavelengths between 2.5 and 40.0  $\mu\text{m}$  is primarily affected by absorption by water vapor, carbon dioxide and ozone. Although scattering of long-wave radiation by air molecules is negligible, scattering by large aerosol may be significant at times; nevertheless, the latter is also neglected in view of other simplifications and unavailability of observational data on aerosols. Upward long wave radiative flux from the ground is determined by the surface emissivity that in turn depends upon land-use type, as well as the ground (skin) temperature. Shortwave radiation instead includes visible and surrounding wavelengths that make up the solar spectrum; for shortwave radiation, the upward flux is the reflection due to surface albedo. Furthermore a sufficiently dense cloud will act as a black body radiator at its top and bottom, while within the cloud the net flux of long wave radiation is zero, so solar radiation is also strongly affected by clouds layers (*Haltiner and Williams* , 1992). Definitely, the object of any parameterization of atmospheric radiation for use in an atmospheric circulation model, taking into account the processes described above, is to provide a simple, accurate and fast method of calculating the total radiative flux profile within the atmosphere. These calculations must supply

- the total radiative flux at the surface to calculate surface energy balance and
- the vertical and horizontal radiative flux divergence to calculate the radiative heating and cooling rates of an atmospheric volume.

The parameterization should include the combined effects of absorption and scattering by the trace gasses of  $H_2O$ ,  $CO_2$  and  $O_3$  together with the model-predicted clouds and water vapor distributions ([Stephens, 1984](#)).

## 2.4 Global and limited area models

Currently the starting point in Numerical Weather Predictions are Global Circulation Models (GCMs); this kind of models simulate the behavior of atmosphere over a domain comprising the whole globe, or at least an hemisphere, at horizontal resolution of tens of kilometers, vertical resolution of tens of meters and temporal step of order of minutes. GCMs involving the entire globe do not need lateral boundary conditions and only initial conditions are necessary. Initial fields for GCMs initialization are produced interpolating over the model grid an high number of observed data coming from different sources displaced all over the world; these sources include a worldwide observation network composed by about 15000 stations locate on the mainland, some thousands of buoys, data deriving from ships and aircraft observations, radar data and atmospheric sounding necessary to have information on vertical structure of atmosphere. The high inhomogeneities in spatial distributions of available observed data resulting in huge areas of the globe not or poorly monitored, as in the case of the oceans, and the difficulties in obtaining atmospheric vertical profiles are some of the major sources of error in initialization of global models.

Because of much of the most destructive behavior of the atmosphere occurs at scales down to a few kilometers, GCMs resolution is not sufficiently high to allow an accurate simulation of atmospheric evolution over these scales; furthermore, currently it is not possible to increase the resolution of this kind of models inasmuch the computational effort necessary to simulate on global wide domain with grid resolution of order of kilometers is too high. To overcome this problem, if the resolution increases, necessarily the extension of the domain must decrease, so were developed Limited Area Models (LAMs) that involve just a portion of the globe allowing an higher

spatial-temporal resolution. For a LAM, because of the presence of lateral boundaries, both initial and lateral boundary conditions must be provided: in this case initial fields and boundary conditions are provided by a model covering a greater area, usually a global model.

In summary major differences between GCMs and LAMs are extension of integration domain, spatial-temporal resolution, and consequently the scales of phenomena that can be explicitly resolved or that require to be parameterized, and the source of initial and boundary conditions used.

Finally LAM performances will be dependent to a multitude of factors as the reliability of initial/boundary conditions (and then reliability of GCMs simulations), the numeric method applied (scheme and truncation errors) to numerically integrate governing equations and the ability of the parameterization schemes to represent sub-grid phenomena effects on the explicitly resolved variables.

## **2.5 The Weather Research and Forecasting model**

Simulations performed in the following of this thesis were produced by Weather Research and Forecasting model (WRF).

WRF model is a numerical weather prediction (NWP) and atmospheric simulation system designed for both research and operational applications. The development of WRF has been a multi-agency collaboration to build a next-generation mesoscale forecast model and data assimilation system: the WRF effort has been a collaborative one among the National Center for Atmospheric Research (NCAR) Mesoscale and Microscale Meteorology (MMM) Division, the National Oceanic and Atmospheric Administration (NOAA) National Centers for Environmental Prediction (NCEP) and other American agencies and universities (*Skamarock et al., 2008*).

WRF is maintained and supported as a community model to facilitate wide use internationally, for research, operations, and teaching. It is suitable for a broad span of applications across scales ranging from large-eddy to global simulations. The model supports a large variety of parameterization schemes, among which clouds microphysics, cumulus, surface layer, plane-

tary boundary layer, atmospheric radiation, some of which will be studied in the following of this thesis.

A WRF simulation, but in general any weather simulations, is composed by three steps: preprocessing, run and postprocessing.

The preprocessing consists in preliminary operations necessary to model initialization: definition of geographic data of the domain, as height, sea-land border, ecc., and interpolation on the domain grid of initial and boundary conditions provided by a global model. The run consists in numerical integration of model equations utilizing initial and boundary conditions assigned in the preprocessing stage; during this phase values of equations variables at each domain grid point are calculated. Finally the postprocessing is the stage in which meteorological fields of interest are calculated starting from data produced during the run stage.

## WRF governing equations

WRF model integrates the compressible, nonhydrostatic Navier-Stokes equations, formulated using a terrain-following mass vertical coordinate  $\eta$  (Figure 2.8). In order to obtain a thickening of vertical levels in correspondence to the orography, where meteorological dynamics are more complicated because of the interaction between the atmosphere and the orography itself, WRF equations are formulated using a vertical coordinate defined as

$$\eta = (p_h - p_{ht})/\mu \quad (2.8)$$

with

$$\mu = p_{hs} - p_{ht}. \quad (2.9)$$

where  $p_h$  is the hydrostatic component of the pressure, and  $p_{hs}$  and  $p_{ht}$  refer to values along the surface and top boundaries, respectively, and  $\mu(x, y)$  represents the mass per unit area within the column in the model domain at  $(x, y)$ . The equations are cast in flux form using variables that have conservation properties, following the philosophy of [Ooyama \(1990\)](#).

In general prognostic equations can be cast in conservative form

$$\frac{d\mu\xi}{dt} = F_{\Xi} \quad (2.10)$$

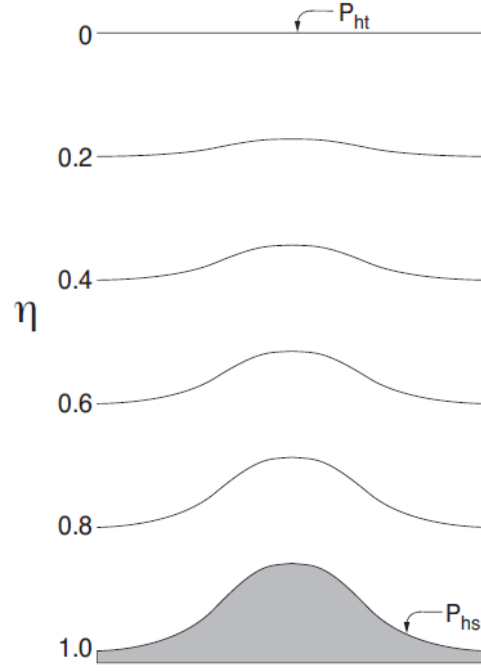


Figure 2.3: Vertical coordinate terrain-following  $\eta$ .

where  $d/dt$  is the total derivative as defined in Chapter 1 and  $F_{\Xi}$  represents sources and sinks related to variable  $\xi$ .

Introducing vertical variable  $\eta$  defined by Equation (2.8), defining

$$\mathbf{V} = \mu \mathbf{v} = (U, V, W), \quad \Omega = \mu \dot{\eta}, \quad \Theta = \mu \theta \quad (2.11)$$

with  $\mathbf{v} = (u, v, w)$ ,  $w = \dot{\eta}$  and redefining variables and coordinates utilized in Chapter 1 ( $x_1, x_2, x_3 \equiv (x, y, z)$  and  $(u_1, u_2, u_3 \equiv (u, v, w)$ ), Navier-Stokes equations and other fundamental equations obtained in Chapter 1 can be reformulated as

$$\frac{\partial U}{\partial t} + (\nabla \cdot \mathbf{V}u) - \frac{\partial}{\partial x}(p\phi_{\eta}) + \frac{\partial}{\partial \eta}(p\phi_x) = F_U \quad (2.12)$$

$$\frac{\partial V}{\partial t} + (\nabla \cdot \mathbf{V}v) - \frac{\partial}{\partial y}(p\phi_{\eta}) + \frac{\partial}{\partial \eta}(p\phi_y) = F_V \quad (2.13)$$

$$\frac{\partial W}{\partial t} + (\nabla \cdot \mathbf{V}w) - g \left( \frac{\partial p}{\partial \eta} - \mu \right) = F_W \quad (2.14)$$

$$\frac{\partial \Theta}{\partial t} + (\nabla \cdot \mathbf{V}\theta) = F_{\Theta} \quad (2.15)$$

$$\frac{\partial \mu}{\partial t} + (\nabla \cdot \mathbf{V}) = 0 \quad (2.16)$$

$$\frac{\partial \phi}{\partial t} + \mu^{-1}[(\mathbf{V} \cdot \nabla \phi) - gW] = 0 \quad (2.17)$$

where  $\theta$  is the potential temperature,  $p$  is the pressure and  $\phi = gz$  is the geopotential which evolution is described by Equation (2.17). In this formulation the right hand side terms  $F_U$ ,  $F_V$ ,  $F_W$  and  $F_{\Theta}$  represent forcing terms arising from not resolved subgrid scale phenomena, spherical projections, and the earth rotation; this terms, as not explicitly resolved, need to be parameterized in order to introduce in Equations (2.12) - (2.17) the effects that they produce on explicitly resolved variables.

Equations (2.12) - (2.17) with the diagnostic relation for the inverse density  $\alpha$

$$\frac{\partial \phi}{\partial \eta} = -\alpha \mu \quad (2.18)$$

and the equation of state

$$p = p_0 \left( \frac{R_a \theta}{p_0 \alpha} \right)^{\gamma} \quad (2.19)$$

are the core of WRF model.

In order to explicitly introduce the effect of moisture, Equations (2.12) - (2.19) are reformulated retaining the coupling of dry air mass to the prognostic variables, retaining the conservation equation for dry air and additionally introducing a further prognostic equation for the evolution of mixing ratio<sup>1</sup> of each hydrometeor presents in atmosphere.

Redefining the vertical coordinate with respect to the dry-air mass,  $\eta$  can be written as

$$\eta = (p_{ah} - p_{aht})/\mu_a \quad (2.20)$$

where  $\mu_a$  is the mass of the dry air in the column and  $p_{ah}$  and  $p_{aht}$  represent the hydrostatic pressure of the dry atmosphere and the hydrostatic pressure at the top of the dry atmosphere; consequently coupled variables are defined as

$$\mathbf{V} = \mu_a \mathbf{v}, \quad \Omega = \mu_a, \dot{\eta} \quad \Theta = \mu_a \theta \quad (2.21)$$

---

<sup>1</sup>The mixing ratio  $\zeta_i$  is defined as the mass of a constituent  $m_i$  divided by the total mass of all other constituents in a mixture  $\zeta_i = \frac{m_i}{m_{tot} - m_i}$ .

and the moist version of Equations (2.12) - (2.17) becomes

$$\frac{\partial U}{\partial t} + (\nabla \cdot \mathbf{V}u) + \mu_a \alpha \frac{\partial p}{\partial x} + \frac{\alpha}{\alpha_a} \frac{\partial p}{\partial \eta} \frac{\partial \phi}{\partial x} = F_U \quad (2.22)$$

$$\frac{\partial V}{\partial t} + (\nabla \cdot \mathbf{V}v) + \mu_a \alpha \frac{\partial p}{\partial y} + \frac{\alpha}{\alpha_a} \frac{\partial p}{\partial \eta} \frac{\partial \phi}{\partial y} = F_V \quad (2.23)$$

$$\frac{\partial W}{\partial t} + (\nabla \cdot \mathbf{V}w) - g \left( \frac{\alpha}{\alpha_a} \frac{\partial p}{\partial \eta} - \mu_a \right) = F_W \quad (2.24)$$

$$\frac{\partial \Theta}{\partial t} + (\nabla \cdot \mathbf{V}\theta) = F_\Theta \quad (2.25)$$

$$\frac{\partial \mu_a}{\partial t} + (\nabla \cdot \mathbf{V}) = 0 \quad (2.26)$$

$$\frac{\partial \phi}{\partial t} + \mu^{-1} [(\mathbf{V} \cdot \nabla \phi) - gW] = 0 \quad (2.27)$$

$$\frac{\partial Q_m}{\partial t} + (\nabla \cdot \mathbf{V}q_m) = F_{Q_m} \quad (2.28)$$

with the diagnostic equation for dry inverse density

$$\frac{\partial \phi}{\partial \eta} = -\alpha_a \mu_a \quad (2.29)$$

and the diagnostic relation for the full pressure (vapor plus dry air)

$$p = p_0 \left( \frac{R_a \theta_m}{p_0 \alpha_a} \right)^\gamma. \quad (2.30)$$

In Equations 2.22-2.30,  $\alpha_a$  is the inverse density of dry air  $1/\rho_a$  and  $\alpha$  is the inverse density taking into account the full parcel density  $\alpha = \alpha_a(1 + q_v + q_c + q_r + q_i + \dots)^{-1}$  where  $q_*$  are the mixing ratios (mass per mass of dry air) for water vapor, cloud, rain, ice, etc., while Equation (2.28) is just the equation for the evolution of mixing ratio of hydrometeors.

## Map projections

For various purpose, analysis, prediction and depiction of meteorological variables, it can be useful to map all or part of the surface of the Earth on a plane. Such map projection should be as nearly like the spherical surface as possible in order to limit distortion of projected fields: if angles between intersecting curves are preserved, projection is called conformal, if distances

from sphere to projection are preserved, the projection is called isometric, ecc.

WRF supports different projection methods among which the most commonly used are Lambert conformal, Polar stereographic and Mercatore (Figure 2.4). The choice of the projection principally depends on the loca-

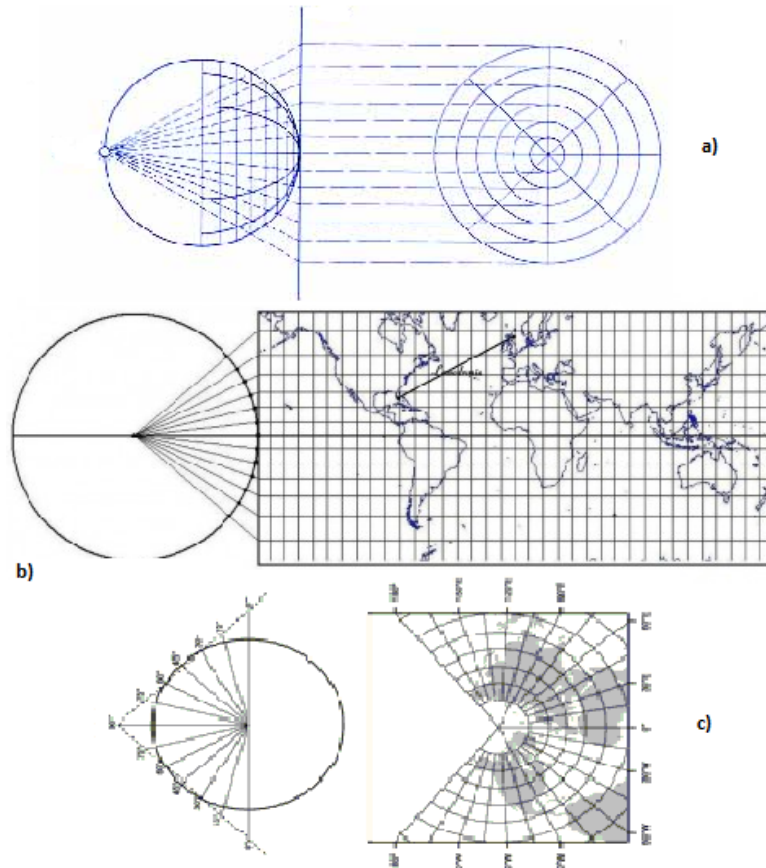


Figure 2.4: a) Polar stereographic, b) Mercatore and c) Lambert conformal projections.

tion of the simulation domain as fields distortion, as visible in Figure 2.4, depends on latitude: for mapping an entire hemisphere, Polar stereographic is the best projection, Mercatore for equatorial zone and Lambert conformal for mid-latitudes.

To transform the governing Equations (2.22) - (2.28), map scale factors  $m_x$  and  $m_y$  are defined as the ratio of the distance in computational space  $\Delta X$

and  $\Delta Y$  to the corresponding distance on the earth surface:

$$(m_x, m_y) = \frac{(\Delta X, \Delta Y)}{\text{distance on the earth } (\Delta x, \Delta y)}. \quad (2.31)$$

So considering a distance in the computational space  $\Delta X$  the link with the actual distance  $\Delta x$  on the sphere is

$$\Delta X = m_x \Delta x \longrightarrow \Delta x = \frac{\Delta X}{m_x}; \quad (2.32)$$

similarly for a distance in  $y$  direction

$$\Delta Y = m_y \Delta y \longrightarrow \Delta y = \frac{\Delta Y}{m_y}. \quad (2.33)$$

In the case of isotropic projections (Lambert conformal, Polar stereographic, and Mercator)  $m_x = m_y = m$  and it is possible to redefine variable  $U$ ,  $V$ ,  $W$  and  $\Omega$  in Equations (2.22) - (2.28) as

$$U = \mu_a u/m, \quad V = \mu_a v/m, \quad W = \mu_a w/m, \quad \Omega = \mu_a \dot{\eta}/m \quad (2.34)$$

and consequently it is possible to rewrite model projected governing Equations (2.22) - (2.28) taking into account that also right hand side terms of these equations are affected by projection inasmuch curvature and Coriolis effects are included in these terms (*Skamarock et al., 2008*).

## WRF discretization

**Temporal discretization** In general a strategy to improve computational efficiency during model equations integration is to use a time split integration in order to separate temporal scales and to integrate high frequency waves through a short time step and low frequency waves using a longer time step. The WRF solver uses a time split integration scheme: slow or low-frequency meteorologically significant modes are integrated using a third-order Runge-Kutta time integration scheme (*Wicker and Skamarock, 2002*), while the high-frequency acoustic modes are integrated over smaller time steps to maintain numerical stability.

The Runge-Kutta methods are a family of implicit and explicit iterative methods developed around 1900: defining model prognostic variables as

$\phi_t = (U, V, W, \Theta, \phi, \mu, Q_m)$  and the equations as  $\Phi^t = R(\Phi^t)$ , third-order Runge-Kutta integration takes the form of 3 steps to advance a solution  $\Phi(t)$  to  $\Phi(t + \Delta t)$ :

$$\Phi^* = \Phi^t + \frac{\Delta t}{3}R(\Phi^t) \quad (2.35)$$

$$\Phi^{**} = \Phi^t + \frac{\Delta t}{2}R(\Phi^*) \quad (2.36)$$

$$\Phi^{t+\Delta t} = \Phi^t + \Delta t R(\Phi^{**}) \quad (2.37)$$

where  $\Delta t$  is the time step for the low-frequency modes.

Regarding high frequency modes, the horizontally propagating acoustic modes and gravity waves are integrated using a forward-backward time integration scheme, and vertically propagating acoustic modes and buoyancy oscillations are integrated using a vertically implicit scheme using the acoustic time step (*Skamarock et al., 2008, Ooyama, 1990 and Laprise, 1992*).

**Spatial discretization** The spatial discretization in the ARW solver uses a C grid staggering for the variables as shown in Figure 2.5: normal velocities are staggered one-half grid length from the thermodynamic variables. Geopotential  $\phi$  and  $\mu$  are defined in correspondence of velocities while the diagnostic variables used in the model, the pressure  $p$  and inverse density  $\alpha$ , are computed at points of thermodynamic variables. Staggered grids enable for certain partial derivatives, such as the advection of a mass-related fields, to be evaluated over a smaller grid interval; this increases the spatial resolution while decreases the effects of truncation errors on the solution (*Haltiner and Williams, 1992*). For spatial integration in the WRF model 2<sub>nd</sub>, 3<sub>rd</sub>, 4<sub>th</sub>, 5<sub>th</sub>, and 6<sub>th</sub> order upwind-biased schemes are available (*Skamarock et al., 2008*).

**Stability constraints** When running WRF model there are two time steps to specify, the time step used by Runge-Kutta scheme and the acoustic time step used in the acoustic sub-step of the time split integration procedure. The necessary condition for convergence of solution in both cases is the Courant-Friedrichs-Lewy (CFL) condition presented in Section 2.2:

$$C = U \frac{\Delta t}{\Delta x}$$

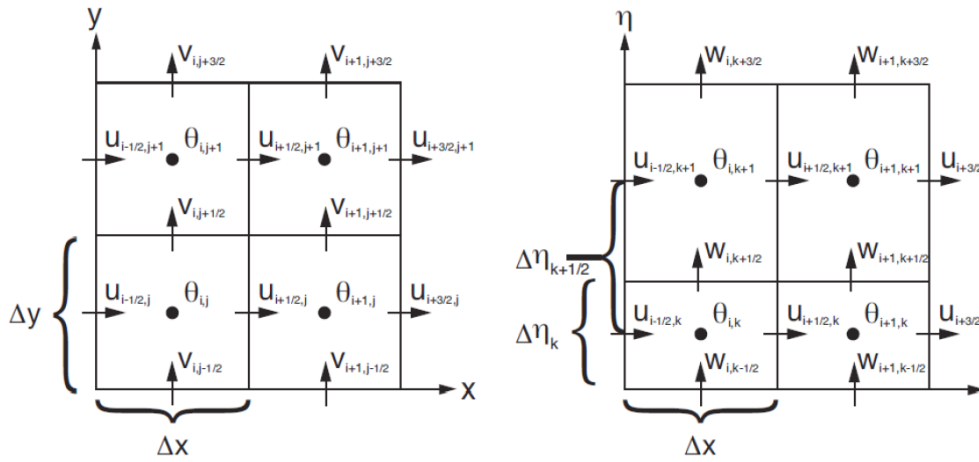


Figure 2.5: Horizontal and vertical grids employed by WRF model.

where the value of  $C$ , usually  $\leq 1$ , depends on the order of the scheme adopted; consequently, the choice of  $\Delta t$  is related to the maximum velocity expected for the simulation in the case of the Runge-Kutta scheme, and to speed of sound in the case of the acoustic time-step. In WRF model it is also possible to choose an adaptive time step: in this case the third-order Runge-Kutta time step is based on the temporally evolving wind fields and computed step by step on the basis of the maximum value of the velocity components, over the whole domain, at the considered time. The adaptively-chosen time step is usually larger than the typical fixed time-step, so the dynamic integrates faster and the time necessary to complete the simulation can be substantially reduced (*Skamarock et al., 2008*).

## Boundary and initial conditions

In order to integrate model equations, initial conditions and, for any non-global numerical simulation, lateral boundary conditions as the simulation domain is finite, are necessary.

After defining the simulation domain (projection type, location on the globe, number of grid points, nest locations, and grid distances) static fields, that

is data that can be considered constant during the simulation, i.e., Coriolis parameter, terrain elevation, land-use type, land/water mask, etc., are interpolated to the prescribed domain.

The second step consists in interpolating 3-dimensional fields (including the surface) as temperature, relative humidity, horizontal components of momentum and 2-dimensional fields as surface pressure, soil moisture, surface temperature, sea surface temperature, etc., provided by a larger scale model. Regarding vertical interpolation the WRF preprocessor vertically interpolates using functions of dry pressure (Equation (2.20)) while input data usually contains both a total pressure and moisture field: starting at the top each column of input pressure data, the integrated moisture is subtracted from the pressure field step-wise down to the surface. Then, by removing the pressure at the model lid, it is possible to obtain the total dry surface pressure  $p_{sa}$ , define the model total dry column pressure

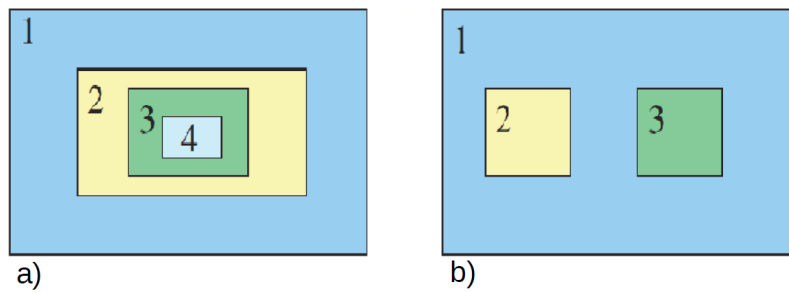
$$\mu_a = p_{sa} - p_{aht}. \quad (2.38)$$

and consequently it is possible to calculate the model vertical level  $\eta$ . Knowing  $\eta$ ,  $p_{aht}$  and the column dry pressure at each  $(i, j, k)$  location, it is now possible to interpolate the 3-dimensional arrays.

## Nesting

WRF model supports horizontal nesting (widely used in simulations performed in the following of the thesis) that allows resolution to be focused over the region of interest by introducing one or more additional grids into the simulations. The nested grids are rectangular and are aligned with the parent (coarser) grid within which they are nested and can be telescopic, Figure 2.6, panel *a*), or at the same level with respect to a parent grid, Figure 2.6, panel *b*).

**1-Way and 2-Way Grid Nesting** There are two ways to produce nested grids simulations: 1-way nesting or 2-way nesting. In both 1-way and 2-way simulation modes, the fine grid boundary conditions (i.e., the lateral boundaries) are interpolated from the coarse grid forecast. In a 1-way nest, this is the only information exchange between the grids (from the coarse



---

Figure 2.6: WRF model allowed nest configurations: telescopic nests, panel a) and nests at the same level with respect to a parent grid, panel b).

grid to the fine grid). In the 2-way nest integration, the fine grid solution replaces the coarse grid solution for coarse grid points that lie inside the fine grid. This information exchange between the grids is now in both directions (coarse to fine for the fine grid lateral boundary computation and fine to coarse during the feedback at each coarse grid time step)(*Skamarock et al., 2008*).

# Chapter 3

## Simulation of heavy precipitations over Liguria with WRF

### 3.1 Introduction

As seen in previous chapters, the way in which unresolved scale phenomena are parameterized is a crucial point in numerical simulation of evolution of the atmosphere; in particular, in this chapter, we focus on the effects that parameterization of microphysics has on precipitation forecasts in case of deep convection events; for this purpose an intercomparison of eight different microphysics parameterization schemes available in the WRF model and an analysis of the sensitivity of predicted precipitation to horizontal resolution are presented. This analysis concerns three different case studies, corresponding to severe rainfall events occurred over Liguria region (Italy) between October 2010 and November 2011. In all the selected cases, the formation of a quasi-stationary mesoscale convective system over the Ligurian Sea interacting with local dynamical effects (orographically-induced low-level wind and temperature gradients) played a crucial role in the generation of severe precipitations.

Mediterranean coastal regions are regularly affected by sudden heavy precipitation events leading to very dangerous flash floods. It may happen that the rain accumulated in one hour accounts for the entire monthly

average of a given location, and the rain accumulated in one day can even account for the entire yearly average (*Altinbilek et al.*, 1997).

The principal meteorological preconditioning factors for such events are quite well known and have been discussed in a number of works (see, for example, *Nuissier et al.*, 2008; *Ricard et al.*, 2012). Firstly, a deep and sustained source of heat and moisture is provided by the Mediterranean Sea during the autumn period. The second factor is the convergence and lifting provided by synoptic configurations advecting south (easterly or westerly) flows to the coasts. The third preconditioning factor is the presence of significant orography next to the sea which can contribute to precipitation enhancement and trigger deep convective motion within the flow by amplifying and focusing low-level moisture convergence.

The structures responsible for these severe events are typically intense and small-sized quasi-stationary V-shaped mesoscale convective systems, repeatedly affecting the same area for several hours (*Fiori et al.*, 2014; *Chappell*, 1986). The severity of these events is critically modulated by local factors such as upwind islands, complex coastlines and steep orography, so that even very small scale (e.g., a few kilometers) features need to be considered. Due to its position and complex topographical peculiarities, one of the most affected areas is Liguria, a region located in northwestern Italy. It consists of a narrow strip of land bordered by the Ligurian Sea, the Alps and the Apennines mountains, reaching elevations above 2000 m. High population density, urban development and strong modifications of local drainage patterns concur to produce a very high hydrogeological risk (*Brandolini et al.* (2012)). Among the most destructive events, we recall the ones occurred in October 1970, September 1992, September 1993 and, more recently, November 2000, October 2010, October 2011 and November 2011 (see, for example: *Fiori et al.*, 2014; *Rebora et al.*, 2013; *Silvestro et al.*, 2012, and the literature therein).

Reliable quantitative precipitation forecasts (QPF) are required to limit the risks induced by heavy precipitation. However, as stated by *Davolio et al.* (2009), severe rainfall prediction, being the result of many mutually interacting multiscale processes, not yet completely understood and modeled, is still a major challenge for numerical weather prediction (NWP) systems (see also *Fiori et al.*, 2011). Furthermore, the intrinsic uncertainty related to deep moist convection (*Hohenegger and Schaer*, 2007) and the

large sensitivity of precipitation to uncertainties in the initial and boundary condition decrease the skill of numerical models, which are usually not yet able to predict timing, spatial location and intensity of precipitation with satisfactory accuracy, even at high horizontal resolution and short forecast times (*Davolio et al., 2009; Weisman et al., 2008; Miglietta and Rotunno, 2012*).

To improve prediction capabilities progress must be made in understanding the mechanisms that govern the formation and the precise localization of such convective systems capable to produce uncommon amounts of precipitation. As seen in Chapter 2, microphysical schemes are the parameterizations responsible for computing atmospheric water vapor, cloud liquid water, cloud ice and various types of precipitation, therefore they are crucial for a correct prediction of severe rainfall events. The broader categories of warm-rain (liquid only), cold (ice, snow, graupel/hail), and mixed-phase (supercooled particles) processes simplify the microphysical processes such as melting, evaporation, accretion, collision-coalescence, accumulation, condensation, deposition, and nucleation that are important in understanding how a convective storm will develop and produce precipitation.

There are, however, basic hydrodynamics-based phenomena which still need to be included in cloud parameterization schemes. An example is the recent understanding of the crucial role played by turbulence in the condensation stage of (warm) cloud formation (*Celani et al., 2008; Celani et al., 2007; Celani et al., 2005*). Such a phenomenon, although believed to be important, e.g., to explain the observed spreading of the droplet size distribution (*Brenguier and Chaumat, 2001*) is still waiting for being incorporated in simplified microphysics parameterizations.

With the variety of microphysics parameterizations that have been developed, it is important to perform intercomparison and sensitivity studies to understand what scheme can be appropriately used for individual cases (*Rajeevan et al., 2010; Morrison and Milbrandt, 2011*). Although comparisons were performed in different ways, a large sensitivity to microphysical schemes of storm structure, precipitation coverage and intensity, and updraft/downdraft strength was found in all these studies. In addition, *Bryan and Morrison (2012)* showed a sensitivity of simulated storms to both microphysics schemes and horizontal resolutions.

In the present study two different strategies have been exploited to as-

sess the model skill in forecasting precipitation: a traditional approach, where matches between forecast and observations are considered on a point-by-point basis, and a new-generation object-based method where model success is based on the correct localization and intensity of precipitation patterns. This last method allows to overcome the known fictitious models performance degradation for increasing spatial resolution: when the model resolution is increased up to a few km, assessing forecast quality by traditional verification statistics, based on point matches between predictions and observations, becomes critical (*Casati et al., 2008; Gilleland et al., 2009; Ebert, 2009*). Fine-scale differences that are not present in coarser resolution forecasts may be penalized by traditional scores, strongly sensitive to localisation and timing errors up to the space and time resolution of the sample (*Lack et al., 2010*). Such shortcomings can be expressed with the so-called ‘double penalty effect’: a spatially shifted, but otherwise perfect forecast, arises in two errors: a miss where rain is observed and a false alarm where it is predicted (*Rossa et al., 2008*).

New-generation spatial verification methods, through the identification and the geometrical description of ‘objects’ in forecast and observation fields (e.g. accumulated precipitation or radar reflectivity), permit to evaluate forecast skill in a more consistent way. A first step in this direction is represented by the so-called neighborhood approach (*Ebert, 2009*). According to this method, good scores are assigned to simulations able to identify precipitation patterns, although not exactly located in space and time: if the forecasted event falls within a chosen distance from the observed event, it can still be considered successful. Through neighborhood-type verification it is possible to assess systematic displacement errors as well as the scale dependency of the model performance (*Tustison et al., 2001; Casati et al., 2008; Ebert, 2009*).

More sophisticated recently proposed spatial verification techniques consist in an objective comparison of some features characterizing forecast and observation fields (see for example *Gilleland et al., 2009*). For instance, *Ebert and McBride (2000)* introduced an object-oriented methodology, the contiguous rain area analysis, that identifies and quantifies the forecast displacement error by ‘measuring’ the spatial error between observed and predicted precipitation objects. Such objects are identified by isolating precipitation patterns in both the forecast and observation fields, through the

use of suitable rainfall thresholds. Once the horizontal displacement is determined (e.g., by minimizing the mean square error between the forecasted and observed objects, or by maximizing the correlation between the objects), the total forecast error can then be decomposed into its components: displacement error, rainfall volume error, and fine-scale pattern error.

The research presented in this chapter compares eight microphysics schemes available in state-of-the-art non-hydrostatic mesoscale model WRF (*Ska-marock et al., 2008*). Specifically, different sets of simulations of recent hazardous events occurred in Liguria region have been performed with the twofold aim of investigating the sensitivity of the model QPF to horizontal resolution and identifying the best performing microphysics parameterization approaches. Model predictions have been verified using rainfall data from the Ligurian regional monitoring network using different verification methodologies. In particular, in addition to a qualitative ‘eyeball’ verification and the traditional approach based on the calculation of categorical scores (*Wilks, 2006*), a new-generation spatial verification technique, namely the Method for Object-Based Diagnostic Evaluation (MODE), developed by Davis et al. (*Davis et al., 2006; Davis et al., 2006*) has been adopted.

## 3.2 Materials and methods

### Ligurian region cyclogenesis

A lee cyclone is a variety of a cyclone that occurs in some specific regions in the middle latitudes and in particular in the lee of the mountains like the Alps, the Rocky Mountains and the Andes. The observations show that cyclogenesis occurs to the east of mountains ridges oriented south-north, and to the south of east-west oriented mountains. Taking into account the prevailing direction of air stream in the mountain regions in the world it is possible to identify most cyclogenesis near mountains as lee cyclogenesis when it occurs in the lee side of the mountains in response to the passage of an upper-level trough. Though the phenomenon of lee cyclones is well known in synoptic meteorology, the mechanisms responsible for the cyclogenesis in the lee of the mountain ridges have not been clarified for a long

time (*Tsidulko and Alpert, 2001*).

The Mediterranean basin, which is affected by moving depressions generated either in the Atlantic Ocean or in northwestern Europe, is well known as a region of frequent cyclones formation. As the Mediterranean is surrounded by an almost continuous barrier of mountains, the geographical and temporal distribution of Mediterranean cyclones appears to be rather complicated; in particular there are some Mediterranean areas that experience an abnormally high frequency of cyclogenetic events: the most remarkable of these is centered on the Gulf of Genoa just south of the Western Alps (*Maheras et al., 2001*). Indeed, the blocking influence of the Alps on north-westerly air streams renders the gulf of Genoa in the Ligurian Sea a preferred place for lee cyclogenesis.

Cyclones in the lee of the Alps frequently occur in consequence of an outbreak of a polar air mass against the Alps. Prior to lee cyclone development a low pressure trough in the upper troposphere approaches the Alps from north or north-west in combination with cold air advection against the Alps in the lower troposphere. The principle effect of the Alps is to block the low-level flow. Although the cold air could in principle go over the mountains, it will be deflected to a good part around the Alps depending on the static stability in place. This blocking effect is often apparent in the deformation of the cold front at the leading edge of the cold air mass. During the blocking period of about 6 to 12 hours the upper-level trough moves over the Alps without hindrance. In this situation the three-dimensional mass balance is disrupted because the pressure fall induced by the approach of the upper-level trough is no more compensated by cold air advection at the ground. Therefore, a pressure fall in the lee of the Alps is found (*Tibaldi et al., 1980; Speranza et al., 1985*). In principle the mass loss would be compensated as soon as that part of the cold air which had to flow around the barrier has arrived in the lee. But secondary effects set in which complicate the scenario. It is not only the mass field which experiences a perturbation by the mountains. At any time there is a tendency in the flow that the wind field is in balance with the mass field (quasi-geostrophic relationship). As a consequence to the disturbed balance there will be forcing of upward motion in the lee of the Alps which in turn leads to a stretching of the low level air mass. Thereby a vortex is generated in the pressure fall area in the lee of the Alps (*Tafferner, 1990*). The situation described

above can strongly look different depending on the flow direction toward the Alps, the vertical depth of the cold air, the strength of the upper-level potential vorticity maximum inside the trough, the strength of advection, the moisture supply from the Mediterranean Sea and the state of the air mass south of the Alps. The intensity of the lee cyclone, its life cycle and the amount of precipitation are all dependent on these flow configurations ([Tafferner, 1990](#)).

The described cyclonic area bears rain, often intense, on the Ligurian coast and hills of Tuscany, due to orographic lift which affects the southern side of the Apennines. The area of low pressure is slow moving, and may follow a trajectory from west to east, then going on to affect the regions of the Adriatic, or move from the north-west to south-east down along the Tyrrhenian Sea producing rain over many parts of Italy. The rain produced over Liguria region in these situations, although often intense, generally are not associated with floods because the non stationarity of the low prevents rain affecting same areas for many hours.

A different situation occurs when a strong high pressure area is present East of Italy. In this case the natural eastward movement of the trough approaching the western Mediterranean is stopped before evolving in a lee cyclone over the Gulf of Genoa. In this situation the position of the trough just West of Liguria region induces at the same time a persisting southerly warm and moist flow over the Tyrrhenian Sea and a cold outflow from the Po valley towards the western and the central part of the Ligurian Sea. The interaction between these two flows can produce quasi-stationary convergence lines causing very intense, persisting and localized rain, further amplified by orographic effect due to the Ligurian Apennines, resulting in devastating floods.

A detailed description of the most recent floods happened over Liguria region is reported in the next section.

### **Description of the case studies**

The selected case studies concern recent flood events occurred in Liguria between October 2010 and November 2011. These high precipitation events

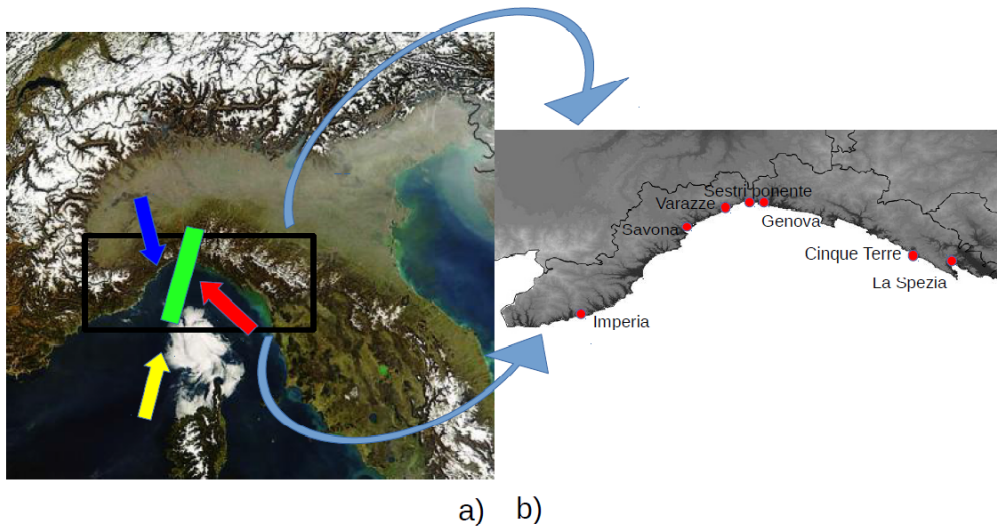


Figure 3.1: Panel *a*): schematic representation of a convergence line (green) over Liguria between the south-easterly low-level jet (red arrow) and the northerly cold flow from the Po Valley (blue arrow). A south-westerly upper-level flow (yellow arrow) contributes to advecting towards the coast the convective cells originated offshore. Panel *b*): Map of Liguria region illustrating the main geographical locations cited throughout the chapter.

are consequence of the formation of quasi-stationary Mesoscale Convective Systems over the Ligurian Sea, triggered and maintained by complex mesoscale features, in particular low-level temperature and winds gradients associated with orographically-induced flows.

Specifically, the onset of convective systems leading to severe rainfall events over the region is favored by the convergence between a warm and moist south-easterly low-level jet on the eastern side, channeled between Corsica and Central Italy and impinging over the Ligurian Apennines, and a northerly shallow cold flow coming from the Po Valley through the lowest orography gaps and affecting the western part of Liguria (Figure 3.1). The magnitude of the low-level temperature gradient between the Po Valley and the Ligurian Sea seems to have a significant influence on the extension and intensity of the cold northerly outflow and, as a consequence, on the exact position of the convergence line triggering the convective development (*Buzzi et al., 2014*).

The case studies considered in the present work are briefly introduced hereafter. Some details about the October 2010 event can be found in [Brandolini et al. \(2012\)](#), while for a more exhaustive description of the 2011 events the reader is referred to the already cited literature (in particular, [Rebora et al., 2013](#); [Fiori et al., 2014](#); [Buzzi et al., 2014](#)).

#### 4 October 2010

Between late evening of the 3 October 2010 and early morning of the 4 October 2010, a deep pressure minimum was present over the Bay of Biscay (986 *hPa*) within a wide trough extending over the western Mediterranean. A frontal system was approaching Liguria and induced an intense warm and moist south or south-easterly flow over the Gulf of Lion and the Tyrrhenian Sea (Figure 3.2, a)). The presence of a relatively high pressure area over the Po Valley favored the establishment of a pressure gradient across the Apennines, associated to cooler offshore winds very close to the coast from Savona to Genoa. The intense low-level convergence triggered the development of several convective cells, persisting over the area for about 6 hours, moving eastwards very slowly. Because of this, very intense rainfalls affected central Liguria, specifically the area surrounding the municipalities of Varazze and Arenzano and the western district of the city of Genoa, Sestri Ponente. Precipitation amounts reached 400 *mm* at Monte Gazzo (with a maximum intensity of 140 *mm/h*) (Figure 3.2, b)) ([Brandolini et al., 2012](#)). In the early afternoon the system attenuated and moved eastwards faster, affecting eastern Liguria with moderate rainfalls.

#### 25 October 2011

A deep pressure minimum (977 *hPa* at 00 *UTC*) was present west of Ireland and a wide frontal system extended from south-eastern Ireland to Morocco (Figure 3.3, a)); at the same time East Europe was affected by a strong high pressure (1036 *hPa* over Baltic countries). During the evening of the 25 October the eastward movement of the low-pressure system originated a secondary minimum located over the Gulf of Lion. This synoptic configuration determined an intense advection of warm and humid air mass from North Africa to Liguria. In the meantime, the presence of a

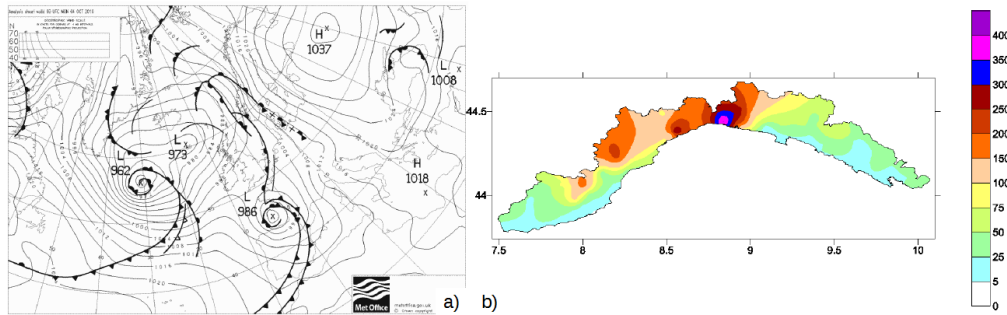


Figure 3.2: Panel a): synoptic situation over Europe at 00 UTC, 4 October 2010. UK Met Office analysis (from <http://www.wetterzentrale.de/>). Panel b): precipitation amount recorded over Liguria by the regional observing network (ARPAL) from October 4, 2010, 00 UTC to October 5, 00 UTC.

meso-high pressure area over the Po Valley associated to pre-existing colder air generated a very strong pressure gradient across the Apennines, favoring a quite massive cold outflow towards the western and central Ligurian Sea (see Figure 4 from [Rebora et al. \(2013\)](#)). Indeed, the temperature gradient between the Po Valley and the warmer eastern Liguria was much stronger than in the case of the October 2010 event, namely about  $12^{\circ}\text{C}$  ([Buzzi et al., 2014](#)) instead of  $4^{\circ}\text{C}$  (not shown). Thus, the convergence line originated in a more south-eastward position and remained quasi-stationary from the late morning to the evening of 25 October 2011, when the cold front approached Liguria. A mesoscale V-shaped convective system developed along the convergence line and produced very heavy rainfalls over the very famous Cinque Terre tourist area as well as the inland areas (Val di Vara, Val di Magra, Lunigiana). In Borghetto Vara rainfall intensity reached  $150\text{ mm/h}$ ,  $330\text{ mm}/3\text{h}$  and  $470\text{ mm}/6\text{h}$ , with a total accumulation equal to  $539\text{ mm}$  (Figure 3.3, b)).

#### 4 November 2011

During the 4 – 8 November 2011 period Liguria was affected by extensive and intense rainfalls that hit the entire regional territory. Particularly, during 4 November a destructive flash flood affected the city of Genoa. The large-scale situation was similar to those described for the previous events and characterized again by a wide, deep low-pressure system over

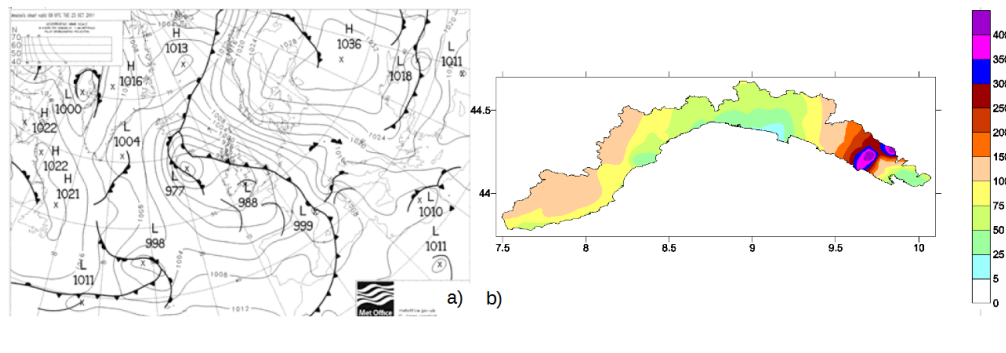


Figure 3.3: Panel *a*): synoptic situation over Europe at 00 *UTC*, 25 October 2011. UK Met Office analysis (from <http://www.wetterzentrale.de/>). Panel *b*): precipitation amount recorded over Liguria by the regional observing network (ARPAL) from October 25, 2011, 00 *UTC* to October 26, 00 *UTC*.

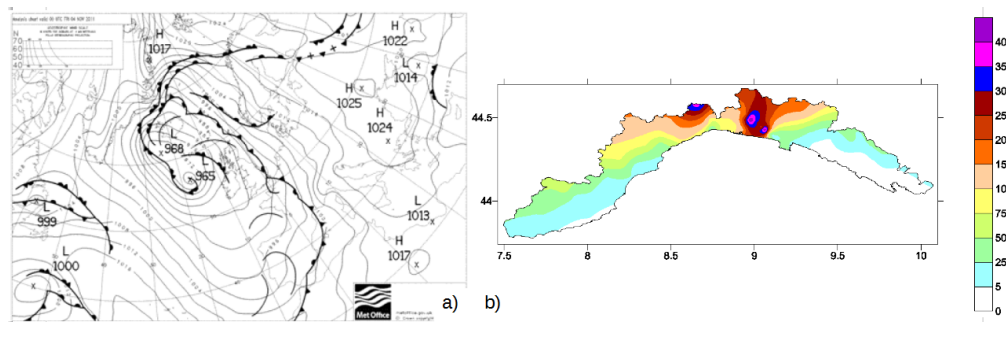


Figure 3.4: Panel *a*): synoptic situation over Europe at 00 *UTC*, 4 November 2011. UK Met Office analysis (from <http://www.wetterzentrale.de/>). Panel *b*): precipitation amount recorded over Liguria by the regional observing network (ARPAL) from November 4, 2011, 00 *UTC* to November 5, 00 *UTC*.

western Europe and a blocking anticyclone over the eastern part of the continent (Figure 3.4, a)). A convergence line between the warm and moist south-easterly low-level jet and the cold outflow originating from the Po Valley formed in this case off the Genoa coast and favored the development of a quasi-stationary self-regenerating V-shaped convective system. The rainfall intensity reached 181 *mm/h* at the Vicomorasso rain gauge station, while total amounts exceeding 400 *mm/12h* were recorded (Figure 3.4, b)).

## Model setup

The Advanced Research core of the WRF model, Version 3.4, was adopted in this study. The WRF model, briefly introduced in the previous chapter, is comprehensive described in [Skamarock et al. \(2008\)](#).

We adopted a model configuration quite similar (with regard to domains set-up and physics options) to that used operationally at the University of Genoa and described in the recent work by [Bove et al. \(2014\)](#), which was focused on atmospheric chemical transport and where a first validation of surface temperature and wind fields was carried out. Three two-way nested computational domains in a Lambert Conic Conformal projection were defined, covering western and central Europe with horizontal resolution of 10 km, northern Italy with horizontal resolution of 3.3 km and the Liguria region with a grid spacing of 1.1 km (Figure 3.5). The number of terrain-following vertical levels adopted was 35, with higher resolution close to the surface. Initial and boundary conditions were generated from the operational global model GFS ([Environmental Modeling Center, 2003](#)) outputs ( $0.5 \times 0.5$  degree resolution). 48-h-long WRF runs, with outputs saved every hour, were performed for each case study. Namely, simulations were started at 00 UTC of October 3 and 4, 2010, October 24 and 25, 2011, November 3 and 4, 2011.

Several physics options are available in WRF to describe the effects that unresolved sub-grid phenomena have on resolved variables (Chapter 2, Section 2.5). For the long-wave radiation the Rapid Radiation Transfer Model (RRTM) scheme ([Mlawer et al., 1997](#)) was selected, whereas for the short-wave solar radiation the Goddard scheme ([Chou and Suarez, 1994](#)) was adopted. The Kain-Fritsch parameterization ([Kain, 2004](#)) was used for cumulus in the outer domain only, whereas in the higher-resolution domains convective processes were explicitly resolved. The Mellor-Yamada-Janjic scheme ([Janjic, 2002](#)) for the boundary layer, the Eta similarity surface layer scheme ([Janjic, 2002](#)) and the Noah land surface model ([Chen and Dudhia, 2001](#)) were chosen.

Other model options being fixed, the intercomparison of the quantitative precipitation forecasts obtained using eight different microphysics schemes was analyzed (summarized in Table 3.1). In general, for bulk microphysics parameterization schemes, for each hydrometeor  $m$  considered

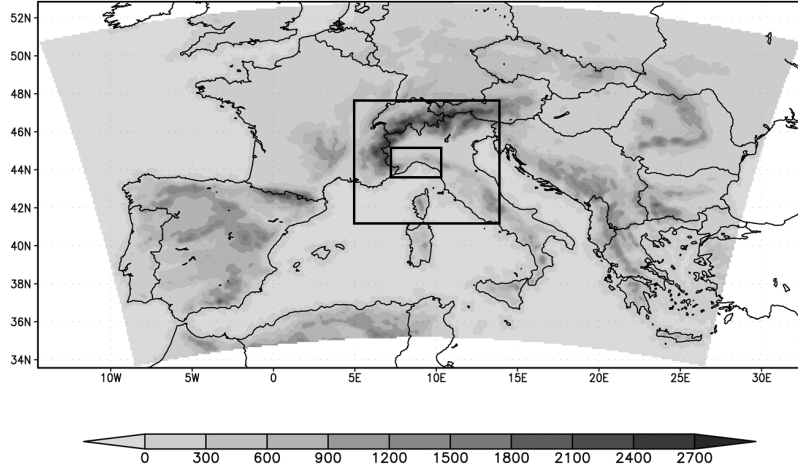


Figure 3.5: Topography ( $m$ ) of the outermost WRF computational domain and location of the two nested domains over northern Italy (larger box) and Liguria region (smaller box).

by the scheme, an equations of the type (2.28) is defined

$$\frac{\partial Q_m}{\partial t} + (\nabla \cdot \mathbf{V} q_m) = F_{Q_m}$$

or equivalently

$$\frac{\partial Q_m}{\partial t} + \frac{\partial U q_m}{\partial x} + \frac{\partial V q_m}{\partial y} = -\frac{\partial \Omega_s q_m}{\partial \eta} + D_{q_m} + S_{q_m} \quad (3.1)$$

where the sedimentation speed,  $\Omega_s$ , and the diffusion coefficient,  $D_{q_m}$ , are function of particles diameter, while  $S_{q_m}$ , also function of particles diameter, represents source or sink terms related to all possible microphysical processes affecting the  $m$ -th hydrometeor, such as growth, melting, freezing, etc. In order to solve Equations (3.1) it is necessary to express the terms  $\Omega_s$ ,  $D_{q_m}$  and  $S_{q_m}$  as a function of the prognostic variable  $Q_m$ . If some semiempirical functional form for the particle size distribution, e.g. gamma distribution, is assumed

$$N_m(D) = N_{0m} \exp(-\lambda_m D) \quad (3.2)$$

and  $N_{0m}$  and the density of the particle  $m$ ,  $\rho_m$ , are known (for example from experimental observations) it is possible to obtain the total mass  $M$

of the hydrometeor in the considered volume and then the mixing ratio as a function of  $\lambda_m$

$$M_m = \frac{\pi\rho_m}{6} \int_0^\infty D^3 N_m(D) dD = \frac{\pi\rho_m}{6} \int_0^\infty D^3 N_{0m} \exp(-\lambda_m D) dD \quad (3.3)$$

from which, reversing the relationship, it is possible to express  $\lambda_m$  as a function of  $M_m$  and then of the mixing ratio. So it is possible to write size distribution (3.2) as a function of the mixing ratio and, finally, close the Equation (3.1) expressing also  $\Omega_s$ ,  $D_{qm}$  and  $S_{qm}$ , that are related to the particles size, as a function of the mixing ratio  $Q_m$ ; this is the case of a single moment scheme. If the scheme, for each hydrometeor, together with the evolution of the mixing ratio, provides also a prognisic equation for the evolution of the concentration of the hydrometeor itself, is named double moment scheme.

The Thompson microphysics (*Thompson et al., 2004*), a well-known and widely tested two-moment bulk scheme, including several techniques found in more sophisticated spectral/bin microphysics schemes and considering all six hydrometeors, was chosen as reference scheme. Its usage is recommended for convection-permitting simulations in the WRF-ARW User's Guide and it has been adopted in many studies concerning the simulation of severe precipitation events (see, for example, the paper by *Fiori et al. (2014)*, analyzing one the case studies considered in the present chapter).

## Observation data set

The verification data set used to evaluate model performances has been derived by the raingauge network named OMIRL, the official regional network that is managed by the Ligurian Regional Environmental Protection Agency (ARPAL) and part of the Italian Raingauge Network of the Italian Civil Protection Department (*Silvestro et al., 2012*). The network is composed by about 150 professional, WMO compliant, systematically maintained monitoring stations (Figure 3.6). Data are provided with a time step of 5 *min* and the territorial coverage is of 1 rain gauge / 40  $km^2$  on average with higher density around the city of Genoa.

For the present study, forecasted and observed 12-*h* accumulated precipitation (from 00 *UTC* to 12 *UTC* and from 12 *UTC* to 00 *UTC* of the

Table 3.1: Overview of the microphysics parameterization schemes considered in the present study.

Parameterization scheme	Acronym	Single/double moment	Number of hydrometeors	References
Purdue-Lin	<i>P-Lin</i>	Single	6	( <i>Lin et al., 1983; Chen and Sun, 2002</i> )
WSM5	<i>WSM5</i>	Single	5	( <i>Hong et al., 2004</i> )
Eta Ferrier	<i>Eta</i>	Single	6	( <i>Ryan, 1996</i> )
WSM6	<i>WSM6</i>	Single	6	( <i>Hong and Lim, 2006</i> )
Thompson	<i>Thom</i>	Double only for cloud ice	6	( <i>Thompson et al., 2004</i> )
Morrison	<i>Morr</i>	Double	6	( <i>Morrison et al., 2009</i> )
WDM5	<i>WDM5</i>	Double only for rain and cloud water	5	( <i>Lim and Hong, 2010</i> )
WDM6	<i>WDM6</i>	Double	6	( <i>Lim and Hong, 2010</i> )

following day) have been considered. From point observations, gridded precipitation fields (see Figures 3.2, 3.3, 3.4) have been obtained using the widely adopted Ordinary Kriging geostatistical technique, recognized as one of the best tools to interpolate discrete measurements (*Ly et al., 2011*). Statistical intercomparison tends to be highly sensitive to forecast displacement error, especially when verifying on high-resolution grids or on a short accumulation time. In particular, large errors can be expected if using a single rain gauge measure as representative of the average precipitation amount over an even very small area and a relatively coarser grid should be adopted to perform model validation (*Cherubini et al., 2002; Mass et al., 2002*). Thus, observed precipitation has been interpolated onto a 5-km spaced regular grid. Further details about this point are given in Section 3.4.

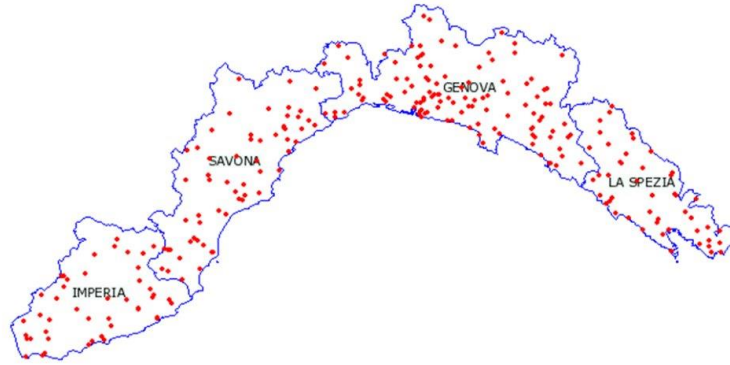


Figure 3.6: The rain gauges of the Ligurian regional monitoring network managed by the Ligurian Regional Environmental Protection Agency, ARPAL.

### 3.3 Verification methodology

In this section the verification approaches adopted in the present work are presented, starting from traditional categorical indices based on the definition of contingency tables. Then, the new-generation MODE spatial verification techniques is introduced, which focuses on the realism of the forecast, by comparing features or ‘objects’ that characterize both forecast and observation fields.

#### The traditional approach

A traditional approach to give a quantitative assessment about model skill in predicting precipitation is based on punctual matches between forecasts and observations. Contingency tables (Table 3.2) are typically defined, in which possible combinations of forecasted and observed precipitation above or below a given threshold are summarized. To be more specific, let us define *hits*,  $a$ , if both observed and forecasted values are above threshold, *false alarms*,  $b$ , if forecast is above threshold and observation is below, *misses*,  $c$ , if forecasted value is below threshold and observed value is above, and *correct no rain forecasts*,  $d$ , if both forecasts and observations are below threshold. From this table it is possible to calculate categorical scores in order to point out some characteristics of the simulations. A comprehensive

description of this methodology is given in [Wilks \(2006\)](#). Below some common statistical scores utilized in model performances evaluation and considered for the present study are summarized.

The Bias is the ratio between the number of forecasted events and the

Table 3.2: Example of a  $2 \times 2$  contingency table summarizing possible combinations of forecasted and observed precipitation for a selected threshold.

	Obs yes	Obs no	
Frc yes	$a$	$b$	$a + b$
Frc no	$c$	$d$	$c + d$
	$a + c$	$b + d$	$N$

number of observed events:

$$Bias = \frac{a + b}{a + c}; \quad (3.4)$$

it provides an evaluation of the model propensity to over- ( $Bias > 1$ ) or underpredict ( $Bias < 1$ ) observed events;  $Bias = 1$  means that the number of forecasted events is the same as that of the observed events. The Bias is not a measure of accuracy and not necessarily  $Bias = 1$  corresponds to a perfect forecast.

The False Alarm Rate (FAR) is the fraction of forecasted events that were false alarms:

$$FAR = \frac{b}{a + b}; \quad (3.5)$$

the best score corresponds to  $FAR = 0$ , the worst to  $FAR = 1$ ; also in this case  $FAR = 0$  not necessarily corresponds to perfect forecasts.

The Threat Score (TS) is the fraction of all forecasted or observed events that were correct:

$$TS = \frac{a}{a + b + c}; \quad (3.6)$$

the best score corresponds to  $TS = 1$ , the worst to  $TS = 0$ ; in this case  $TS = 1$  means perfect forecasts.

## Spatial verification techniques

Spatial verification methods are particularly suitable to address the model capability to reproduce structures like the convective systems responsible

for the high precipitation events considered in the present research, which, because of their typical dimensions, need high-resolution simulations to be predicted (*Lack et al., 2010; Gilleland et al., 2009*). Such methods are consistent with subjective perceptions and reward simulations able to identify precipitation patterns, even if not exactly located in space and time. Figure 3.7 helps us to understand the necessity to discriminate different situations: cases (a)-(d) will yield the same scores, (namely,  $TS=0$ ) although they pertain very different types of forecast errors. On the contrary, case (e) would be associated to a positive TS value, but would probably not be evaluated as the best subjectively.

The spatial verification approach used in this study is the Method for

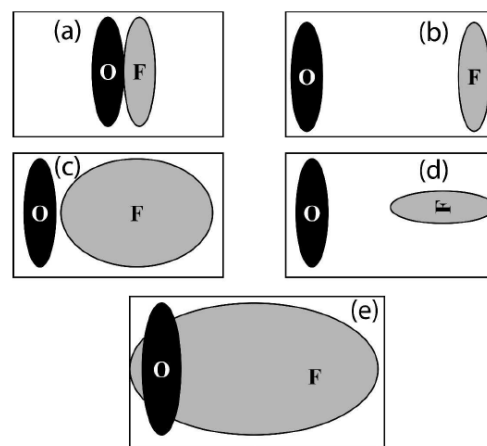


Figure 3.7: Schematic example of different combinations of forecasts and observations: shaded areas represent idealized rain patterns, either observed (black) or predicted (grey). From *Davis et al., 2006*.

Object-Based Diagnostic Evaluation (MODE), developed by Davis et al. (*Davis et al., 2006; Davis et al., 2006*) and implemented in the popular MET verification tool by the NCAR Developmental Testbed Center. The first step is the identification of objects, namely precipitation patterns, in the observed and predicted fields. These structures are defined not only by applying an intensity threshold to the field, but also by a convolution procedure whereby the fields are first smoothed over space and then thresholded; the convolution step serves to make areas more contiguous than in

the original field and to filter out too small or weak features that are not interesting for the study (Davis *et al.*, 2009). Varying radius of convolution and threshold changes the number of objects, their intensity and dimensional scale: it is user's task to choose suitable values in order to focus on the target phenomena. After identification of objects, attributes that are considered relevant for the situation under study are defined, like object displacement, orientation, extension, intensity, and for any forecasted and observed objects pair an index is derived in which user-defined weights to these attributes are combined through an algorithm. This index, called total interest (Davis *et al.*, 2009), is given by:

$$I_j = \frac{\sum_{i=1}^M c_i w_i F_{i,j}}{\sum_{i=1}^M c_i w_i} \quad (3.7)$$

where  $j$  refers to the  $j$ -th objects pair considered and  $F_{i,j}$  is the interest function that prescribes, on a scale from 0 to 1 with 1 being perfect, how closely a forecast attribute matches the observed attribute. The coefficient  $w_i$  is the weight assigned to that interest function and  $c_i$  is a function of attribute that describes the confidence in a partial interest value obtained from  $w_i F_{i,j}$ , while  $M$  is the total number of attributes considered.

### 3.4 Results and discussion

The analysis of the numerical experiments realized in the present study aims at the evaluation of the sensitivity of the QPF provided by the WRF model to different modeling configurations, in particular to the spatial resolution of the simulations, and at the intercomparison of different microphysics parameterization schemes. At this stage, a preliminary qualitative analysis is given, mainly obtained from eyeball verification, while in the following subsections a more objective evaluation is provided through the application of the statistical techniques presented in the previous section.

In Figure 3.8, the 24-h accumulated precipitation over Liguria region for the event on 25 October 2011, predicted by the WRF model at different resolutions, is reported. In this case, the Thompson microphysics, taken as the reference scheme, is used. It is evident that higher-resolution simulations are capable to provide more realistic and detailed precipitation patterns. In particular, predicted rainfall peaks are closer to the observed

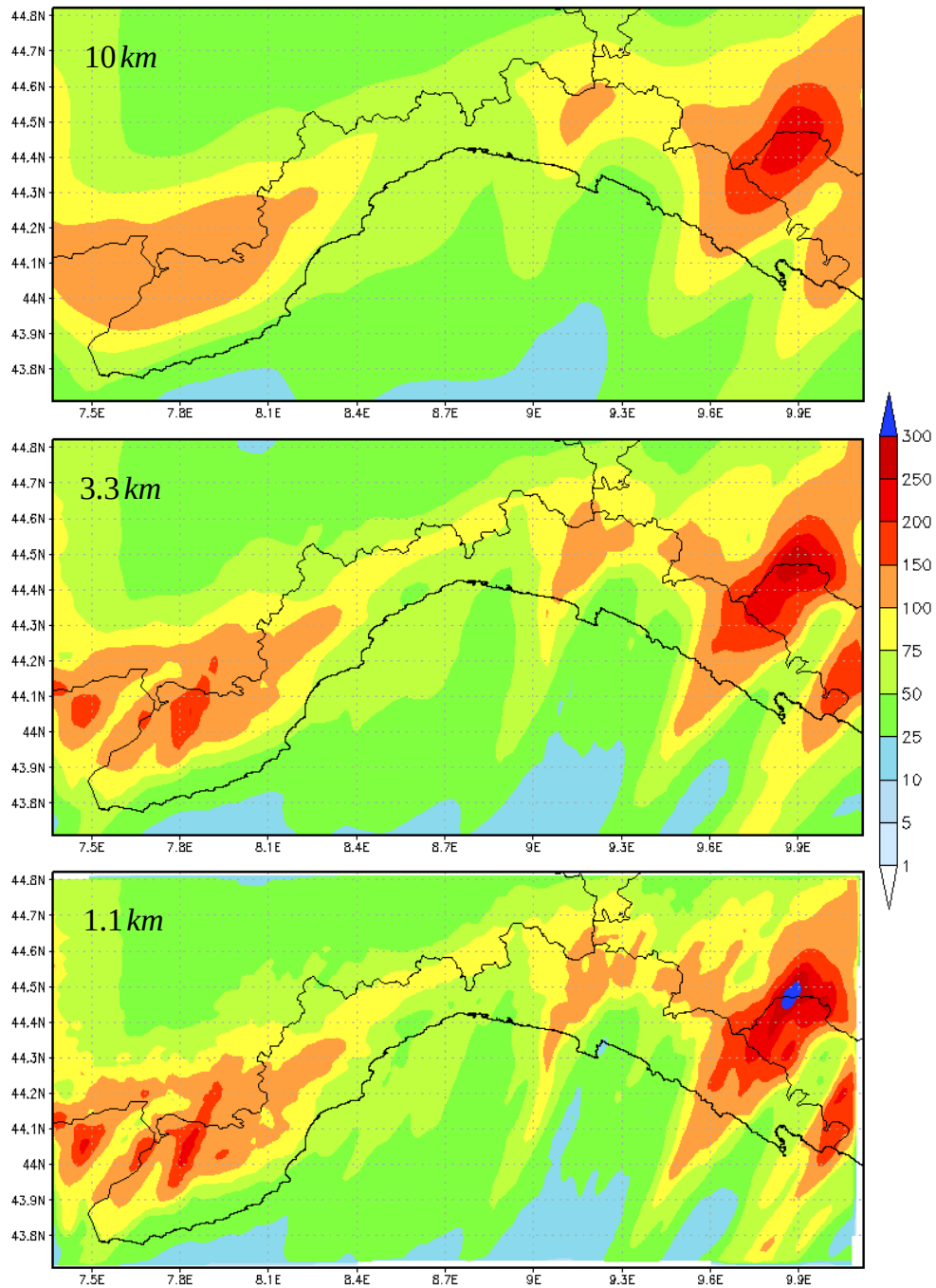


Figure 3.8: 24-*h* accumulated precipitation predicted over Liguria by the WRF model reference configuration (Thompson microphysics) at different resolutions: 10 *km* (top), 3.3 *km* (center) and 1.1 *km* (bottom). Simulations are initialized at 00 *UTC* of 25 October 2011 and forecast valid time is 26 October 2011, 00 *UTC*.

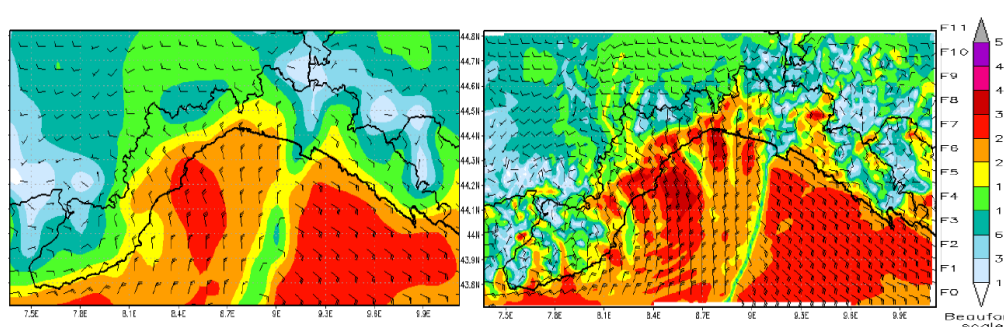


Figure 3.9: 10-*m* wind field predicted by the WRF model at 06 *UTC*, 25 October 2011 at different resolutions: 10 *km* (left) and 1.1 *km* (right). Shaded contours represent Beaufort scale classes and corresponding wind speed values in knots.

ones (see Figure 3.3 in Section 3.2) and more extended over the sea than in the parent domain. Indeed, while at a 10-*km* resolution precipitation maxima are located over the inland hilly areas and the orographic enhancement seems to be the dominant process, at convection-permitting resolutions the precipitation pattern associated with the convective system is better reproduced. In particular, in the simulation on the finest grid the narrow convergence line between the moist south-easterly low-level jet and the shallow cold flow from the Po Valley, playing a crucial role in triggering the onset of the convective system and driving its evolution, is very well caught (Figure 3.9). Similar considerations can be drawn for the other considered case studies, in particular for the event on 4 November 2011. Slightly different is the case of 4 October 2010, when the convergence line was less pronounced and formed very close to the coast off the western suburbs of the Genoa city (not shown). In this situation the WRF model, even at 1.1 *km* resolution, reproduced quite poorly these very small-scale features and underestimated quite considerably the observed rainfall peaks. Nevertheless, higher-resolution simulations again outperformed predictions on the parent domain grid (Figure 3.10).

In Figure 3.11, precipitation amounts predicted for the October 2011 event by all the considered microphysical schemes on the finest resolution computing domain are compared. The precipitation patterns predicted by the various schemes exhibit relevant differences, highlighting a quite strong

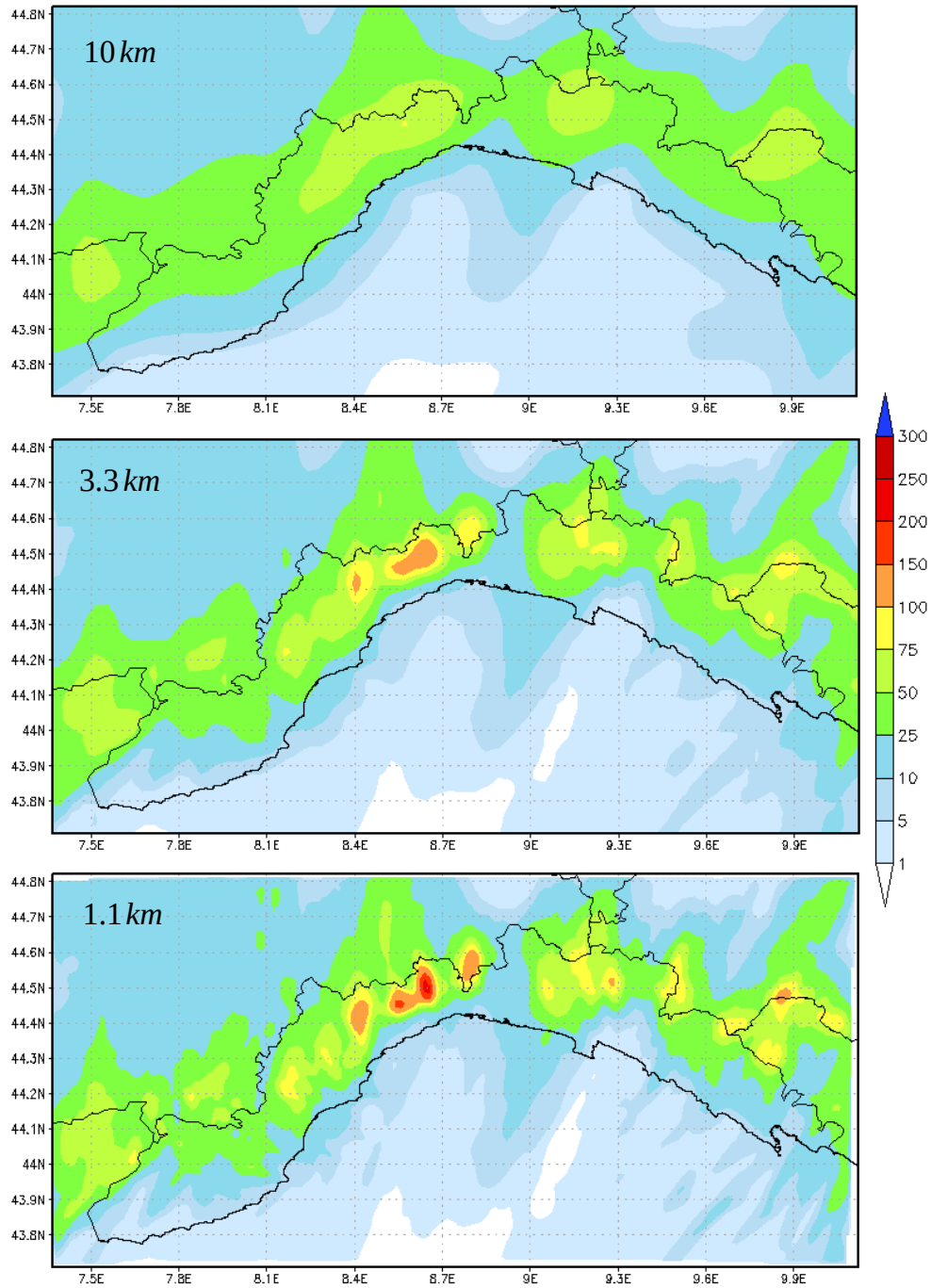


Figure 3.10: 24-hr cumulated precipitation predicted over Liguria by the WRF model reference configuration (Thompson microphysics) at different resolutions: 10 km (top), 3.3 km (center) and 1.1 km (bottom). Simulations are initialized at 00 UTC of 04 October 2010 and forecast valid time is 05 October 2010, 00 UTC.

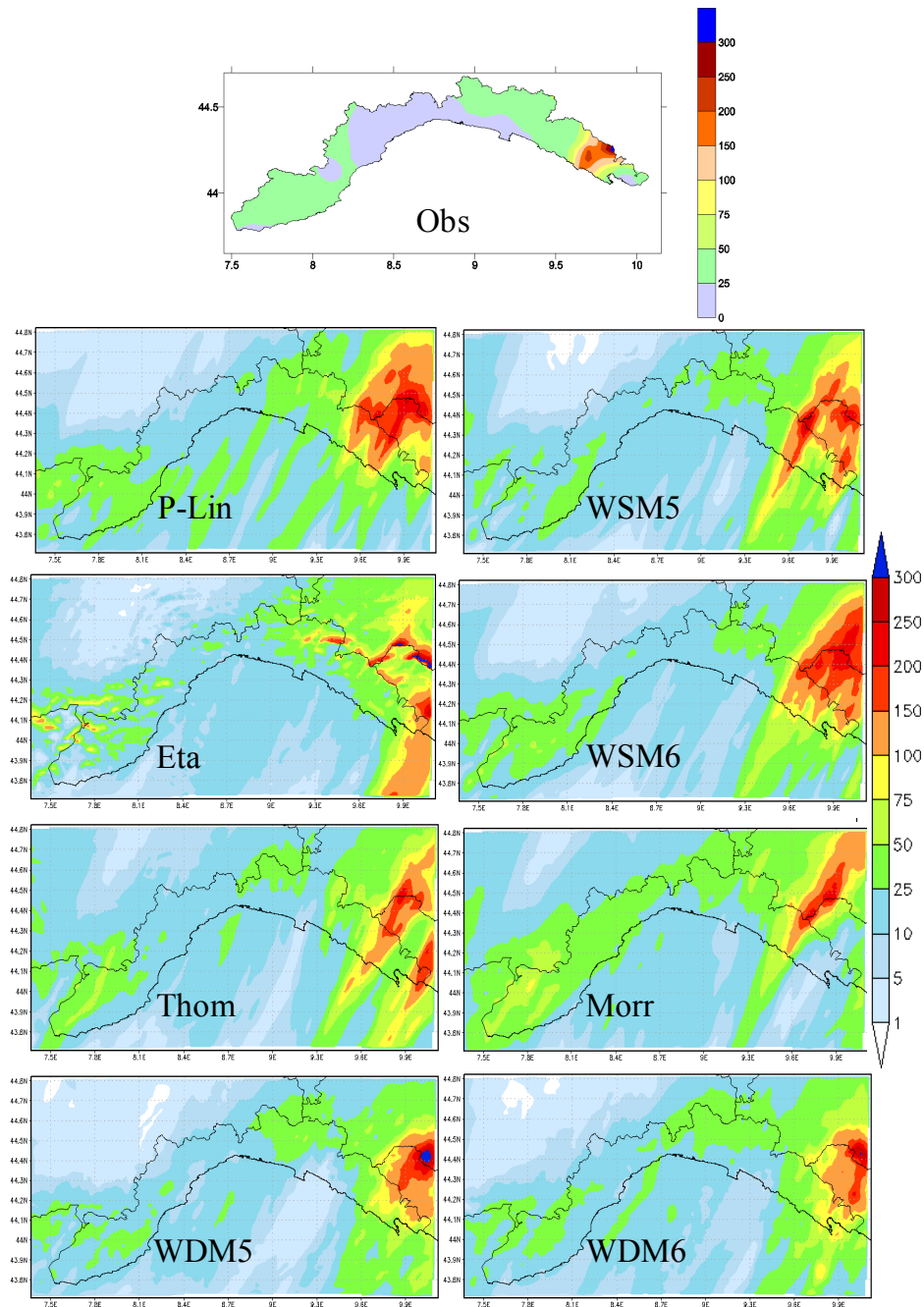


Figure 3.11: Observed (top) and predicted precipitation using different microphysical parameterization schemes on the 1.1 km resolution domain. Rainfall is accumulated from 12 UTC, 25 October to 00 UTC, 26 October 2011 and simulations are started at 00 UTC of 25 October 2011.

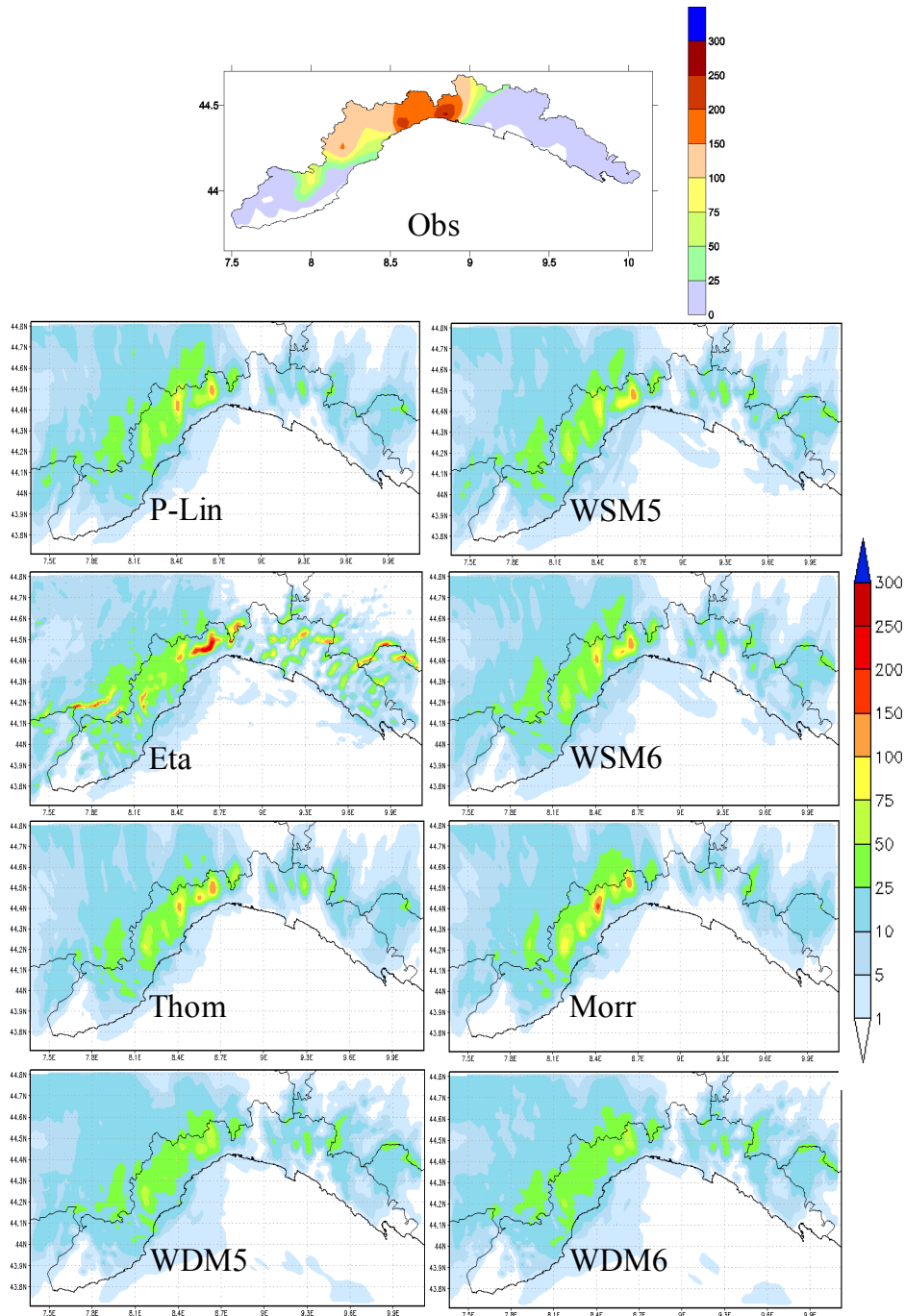


Figure 3.12: Observed (top) and predicted precipitation using different microphysical parameterization schemes on the 1.1 km resolution domain. Rainfall is cumulated from 00 UTC, 04 October to 12 UTC, 04 October 2010 and simulations are started at 00 UTC of 04 October 2010.

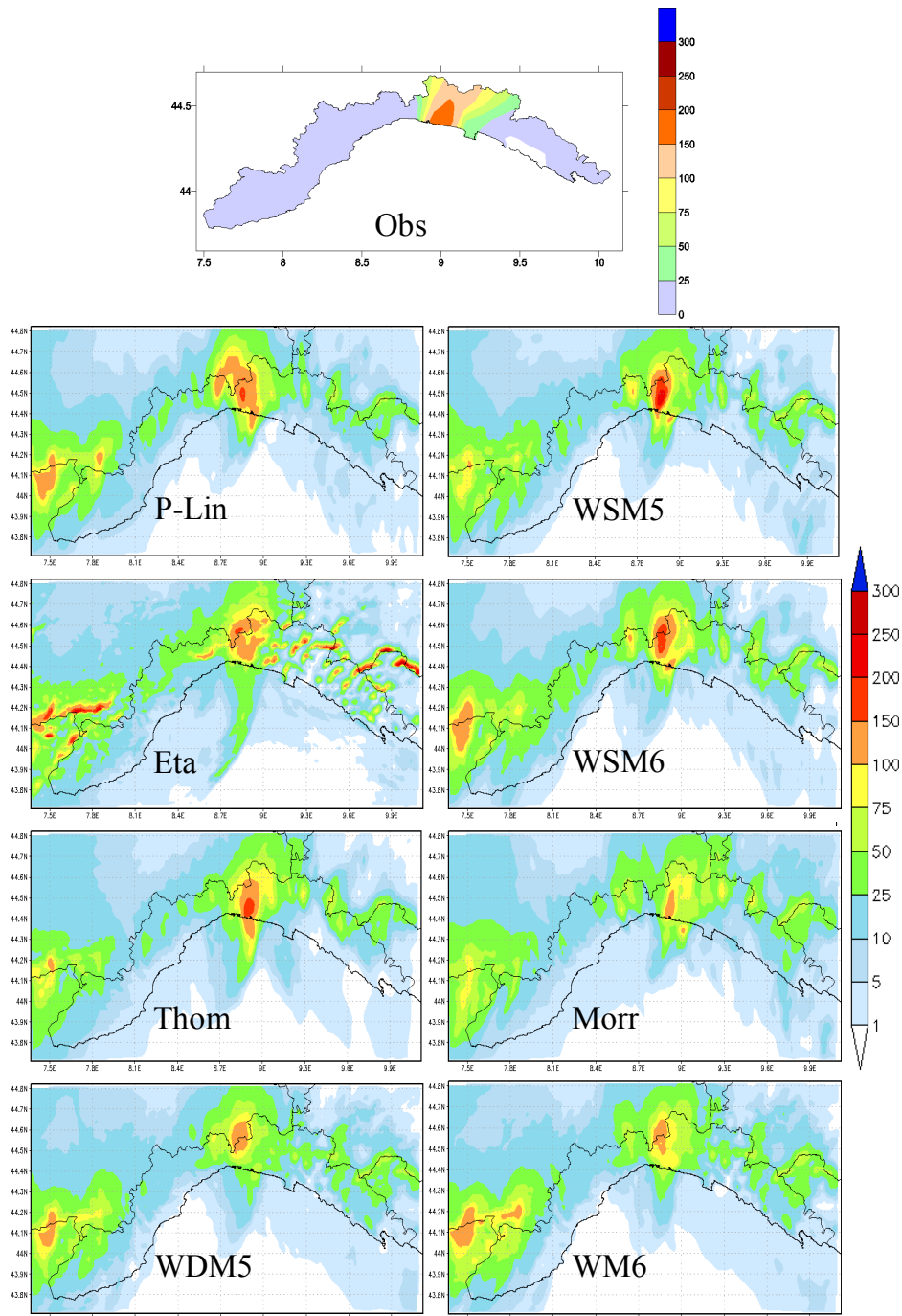


Figure 3.13: Observed (top) and predicted precipitation using different microphysical parameterization schemes on the 1.1 km resolution domain. Rainfall is cumulated from 00 UTC, 04 November to 12 UTC, 04 November 2011 and simulations are started at 00 UTC of 03 November 2011.

dependence of the QPF on the microphysics adopted. More realistic predictions in terms of intensity and location of precipitation are obtained using *WSM5*, Thompson and Morrison schemes, while simulations with *Eta*, *WDM5* and *WDM6* schemes show quite poor performances. In particular, the Eta Ferrier scheme seems to overestimate the orographic precipitation enhancement, producing a too high number of rainfall peaks, whose location is often completely wrong (see analogous comparison for the other considered events in Figures 3.12 and 3.13).

Table 3.3 summarizes the maximum precipitation predicted by all the considered microphysics at 1.1 km resolution versus the maximum precipitation observed in the three events here studied. Precipitation is accumulated over 24 h: second and fourth columns refer respectively to +24-h and +48-h forecasts, third and fifth columns report the distance (in km) between observed and predicted precipitation peaks. The aforementioned underestimation of the precipitation maxima for the October 2010 case study is evident, with the sole exception of the simulations conducted with the *Eta* scheme, whose drawbacks have already been discussed. On the contrary, QPF for the October 2011 and November 2011 events is more satisfactory, despite a certain underestimation by most of the modeling experiments. From this simple analysis, Purdue-Lin, WSM5, WSM6, Thompson and Morrison schemes seem to provide the best results.

It is to point out that for the 4 October 2010 and, at a lesser extent, the 4 November 2011 events, +48-h forecasts seem to better approximate the observed rainfall peaks, but generally the localization of the event is improved by the most recent forecast. The mean distance between observed and forecasted peaks, considering all the events, is 37.2 km at +24 h and 57.0 km at +48 h. This fact underlines the role of the initialization on final performances and further work should be addressed to study the sensitivity of the model to initial and boundary conditions for a more complete analysis.

### Point verification

A first attempt to provide an objective quantification of model performances is given from the calculation of some traditional statistical indices, presented

Table 3.3: Maximum 24-*h* accumulated rainfall predicted by the WRF model at 1.1 *km* resolution for the three events considered in this study as a function of the microphysical scheme and for different forecast horizons. Second and fourth columns refer to simulations initialized at 00 UTC of the day when the event occurred (+24 *h*) and at 00 UTC of the previous day (+48 *h*), respectively. Third and fifth columns report the corresponding distances from the rain gauges where the highest precipitation was observed, shown in the last column.

4 October 2010					
Parameterization scheme	Max +24 <i>h</i> fcst ( <i>mm</i> )	Dist ( <i>km</i> )	Max +48 <i>h</i> fcst ( <i>mm</i> )	Dist ( <i>km</i> )	Max obs ( <i>mm</i> )
<i>P-Lin</i>	173.3	15.9	215.7	15.9	
<i>WSM5</i>	201.1	15.9	243.0	15.9	
<i>Eta</i>	477.4	81.5	467.2	81.5	
<i>WSM6</i>	204.8	15.9	235.4	15.9	411.2
<i>Thom</i>	218.1	17.7	209.5	17.3	
<i>Morr</i>	194.6	34.2	208.6	25.1	
<i>WDM5</i>	117.2	81.4	163.4	75.8	
<i>WDM6</i>	119.4	49.4	182.3	81.5	
25 October 2011					
Parameterization scheme	Max +24 <i>h</i> fcst ( <i>mm</i> )	Dist ( <i>km</i> )	Max +48 <i>h</i> fcst ( <i>mm</i> )	Dist ( <i>km</i> )	Max obs ( <i>mm</i> )
<i>P-Lin</i>	368.4	9.8	251.0	176.0	
<i>WSM5</i>	343.2	29.7	299.1	29.1	
<i>Eta</i>	632.8	30.3	505.5	29.5	
<i>WSM6</i>	361.4	24.9	338.5	16.6	538.2
<i>Thom</i>	361.9	29.9	224.4	30.5	
<i>Morr</i>	358.9	29.9	224.0	29.5	
<i>WDM5</i>	413.8	34.4	240.4	34.3	
<i>WDM6</i>	460.6	32.0	246.5	36.1	
4 November 2011					
Parameterization scheme	Max +24 <i>h</i> fcst ( <i>mm</i> )	Dist ( <i>km</i> )	Max +48 <i>h</i> fcst ( <i>mm</i> )	Dist ( <i>km</i> )	Max obs ( <i>mm</i> )
<i>P-Lin</i>	304.5	26.9	326.8	129.5	
<i>WSM5</i>	297.1	25.7	258.0	9.1	
<i>Eta</i>	557.8	95.9	609.5	80.0	
<i>WSM6</i>	299.7	25.7	267.2	126.9	477.6
<i>Thom</i>	310.0	28.1	256.1	27.0	
<i>Morr</i>	353.7	28.5	204.1	28.5	
<i>WDM5</i>	185.2	26.8	235.0	126.4	
<i>WDM6</i>	216.3	131.9	372.2	130.1	

in Section 3.3. Model precipitation outputs were interpolated to the locations of observing stations using bilinear interpolation. Other interpolation schemes were tested (nearest neighbor and distance-weighted mean), but no significant difference was found in the obtained results. From this data we obtained ten contingency tables (corresponding to the ten thresholds utilized for the analysis: 0.2, 5.0, 10.0, 20.0, 30.0, 40.0, 50.0, 75.0, 100.0 and 150.0  $mm/12 h$ ) for the calculation of the statistical indices.

Bias, False Alarm Rate and Threat Score are reported for each case study in Figure 3.14. Two 48-h-long simulations with a 24-h initialization time shift have been considered for each event. The indices have been calculated on a sum of four contingency tables (i.e. two tables for each model run, corresponding to 12-h accumulation periods: from 00 UTC to 12 UTC and from 12 UTC to 00 UTC of the following day), following a procedure similar to that described by *Mariani et al.* (2005).

For the sake of brevity, these plots refer to the reference modeling configuration adopted (i.e. Thompson microphysics), but analogous considerations hold for the other microphysics schemes studied. It is evident that there is almost no difference between 3.3- $km$  and 1.1- $km$  resolution simulations, and in some cases simulations on 3.3- $km$  grid seem to be even better than those on the finest grid. Bias and TS values, for thresholds between 0.2  $mm/12 h$  and 50.0  $mm/12 h$ , are lowest for 1.1- $km$  simulations and the parent domain obtains the best scores. Only for higher thresholds finer resolution simulations outperform those on the parent domain (see especially the FAR plot).

This behavior is related to the double penalty problem mentioned in the Introduction of the chapter: although from an eyeball verification a finer resolution seems to perform better, the statistical indices values lead us to other conclusions.

In Figures 3.15 - 3.16 similar plots are shown. In this case, the indices obtained from the two contingency tables corresponding to each model run are reported, to highlight the impact of the initial conditions on the forecast skill. As already emerged from Table 3.3, it is evident that only for the 25 October 2011 event the most recent forecast obtains significantly better scores. Conversely, simulations initialized the day before the event seem to give more accurate results in the other considered events, especially for the 4 November 2011 case study.

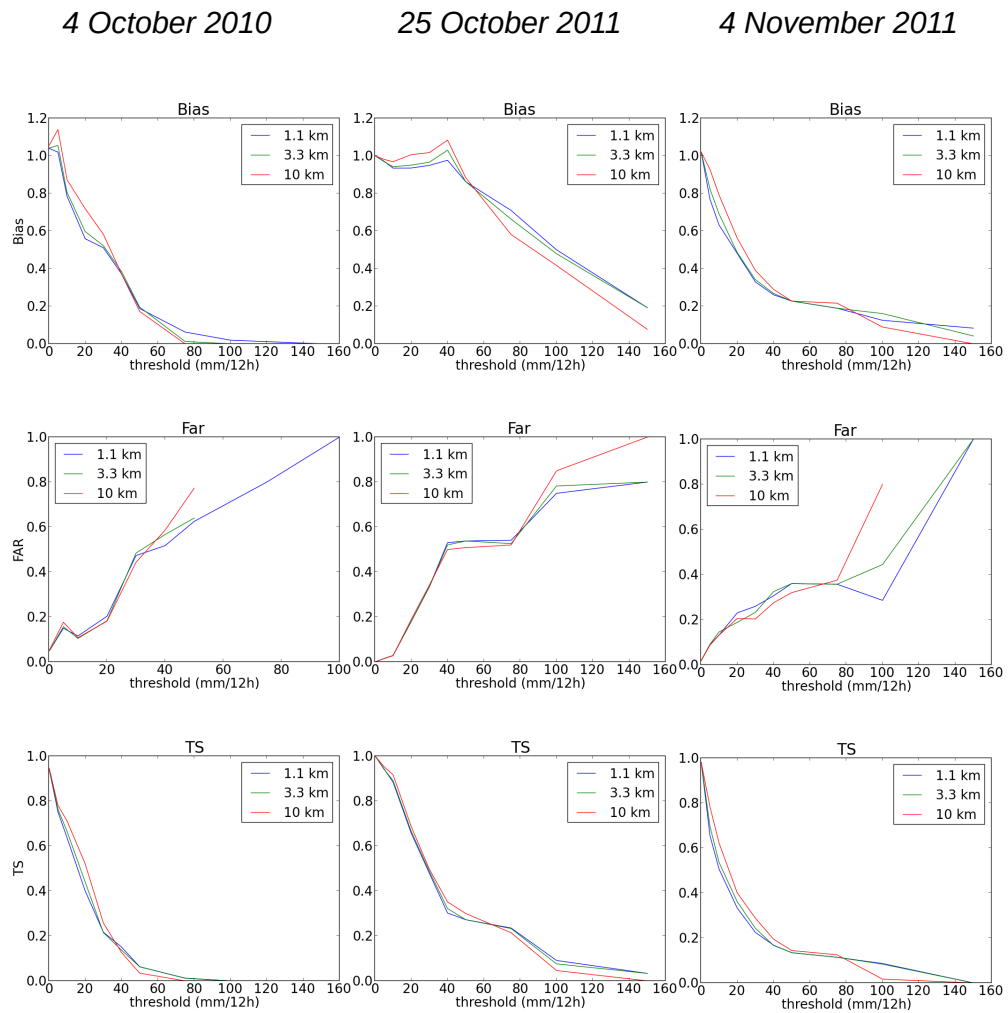


Figure 3.14: Bias (top), False Alarm Rate (center) and Threat Score (bottom) versus precipitation threshold calculated from the simulations of 4 October 2010 (left), 25 October 2011 (center) and 4 November 2011 (right) events at different resolutions using Thompson microphysics.

The double penalty issue is even more evident from the histograms reported in Figure 3.17. Here the QPFs at 10 km and 1.1 km grid resolution for all the eight numerical experiments initialized on 3 November 2011 at 00UTC are compared with the quantitative precipitation estimation (QPE-black bars) evaluated on the same range of time. Observed precipitation amounts refer to the stations belonging to the OMIRL network that have recorded the highest rainfall peaks during the whole event. It is evident the considerable decrease in the precipitation predicted by the simulations on the finest grid with respect to those on the parent domain, despite Figures 3.8 and Figure 3.10 show an increase (in some case a doubling) of predicted precipitation intensity at higher resolutions. The results shown in Figure 3.17 are the most striking, but similar findings have been obtained for all the considered events, also for shorter accumulation times, namely 12 or 24 hours (not shown for the sake of brevity).

This is due to the greater localization of precipitation peaks (more rain in a more restricted area) and to the consequently reduced likelihood that a specific grid point (corresponding to the location of a station) belongs to the precipitation peak area. These results confirm the inadequacy of verification based on point matches between forecasts and observations and the need for different verification techniques when high resolution simulations are considered.

## Object-oriented verification

To overcome the problems posed by traditional point verification and discussed in the previous sections, the new-generation spatial verification technique named MODE, introduced in Section 3.3, has been used. For this purpose, precipitation fields on a 5-*km*-spaced regular lat-lon grid have been obtained from station data (more details are given in Section 3.2). Forecast fields have been interpolated on the same grid from their native resolutions (namely, 10 *km*, 3.3 *km* and 1.1 *km*) using the remapping technique (Accadia *et al.*, 2003), that, by considering grid point values as grid-box ones, conserves the total precipitation forecast over the native grid.

The choice of the verification grid (as well as that of quite long accumulation periods, 12 h or 24 h) is a sort of balance between two counteracting requirements. On the one hand, some kind of spatial and temporal upscal-

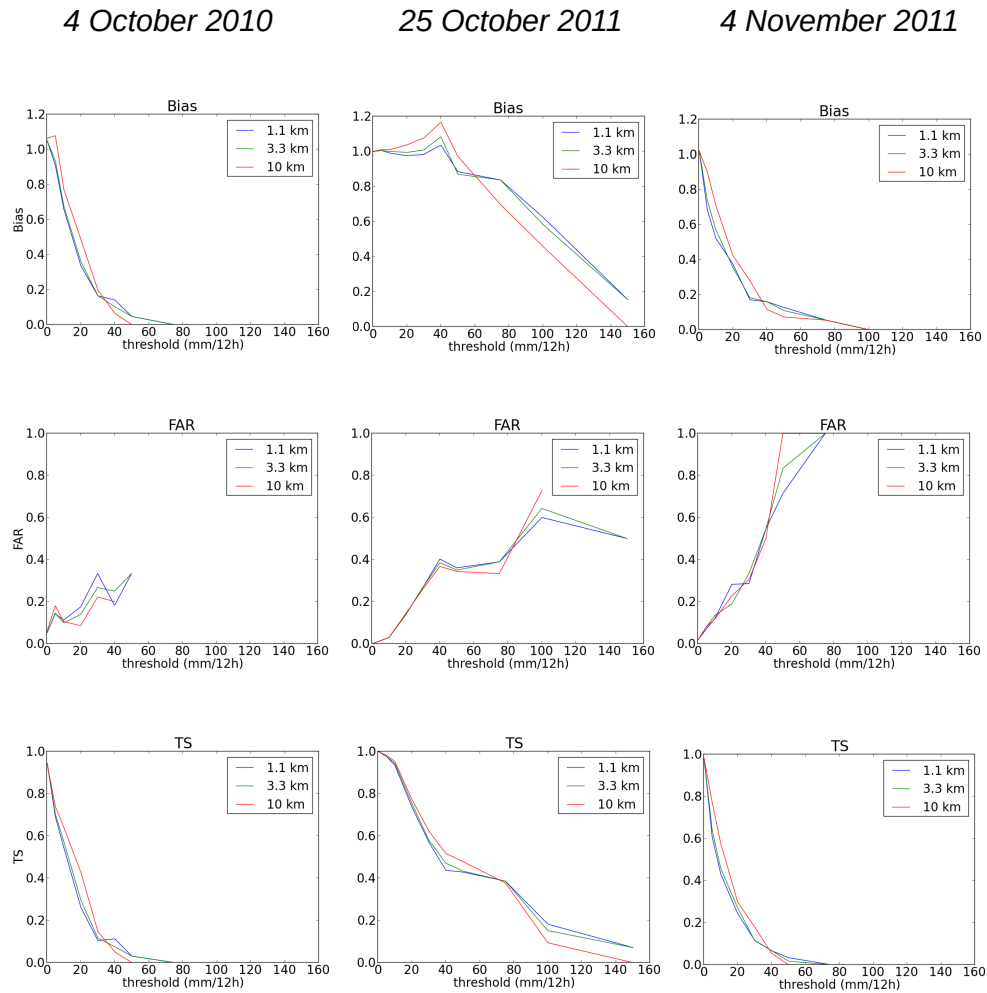


Figure 3.15: Bias (top), False Alarm Ratio (center) and Threat Score (bottom) versus precipitation threshold calculated from the simulations of 4 October 2010 (left), 25 October 2011 (center) and 4 November 2011 (right) events at different resolutions using Thompson microphysics, calculated on the basis of the simulations initialized the same day of the events.

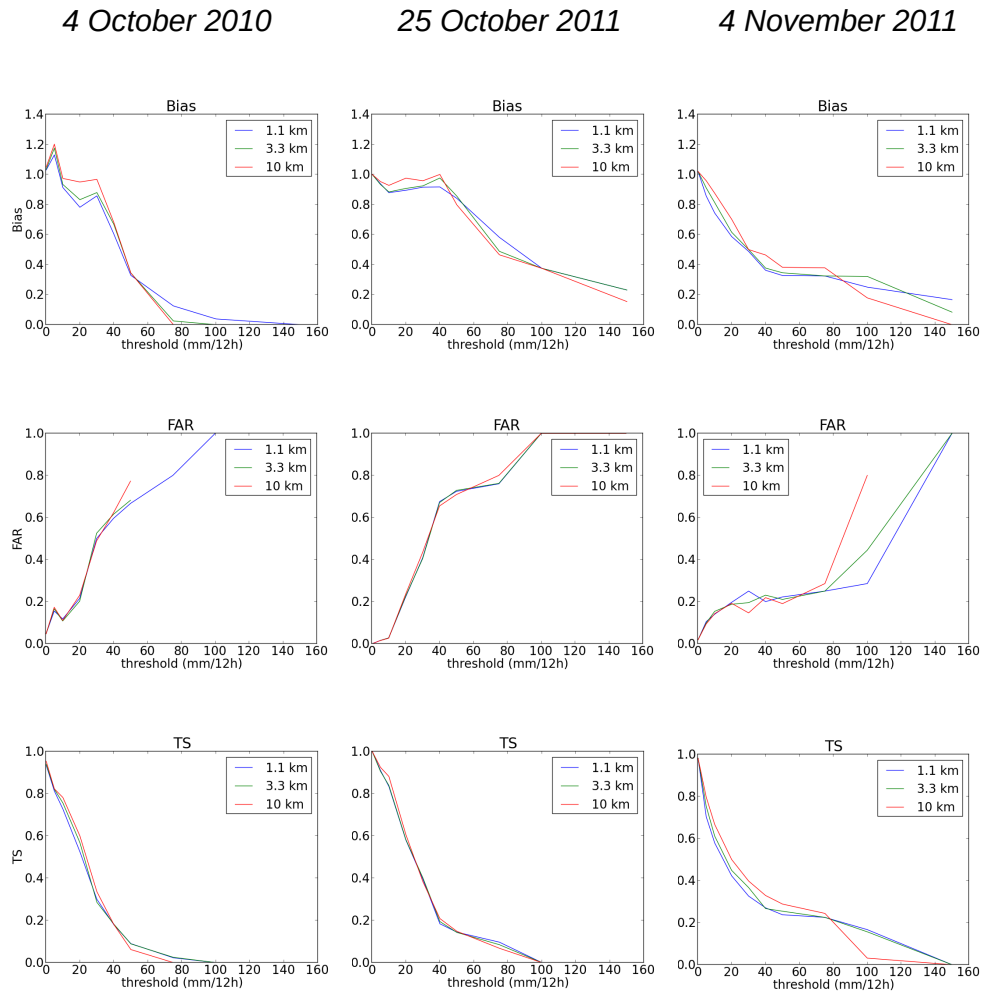


Figure 3.16: Bias (top), False Alarm Ratio (center) and Threat Score (bottom) versus precipitation threshold calculated from the simulations of 4 October 2010 (left), 25 October 2011 (center) and 4 November 2011 (right) events at different resolutions using Thompson microphysics, calculated on the basis of the simulations initialized the day before the events.

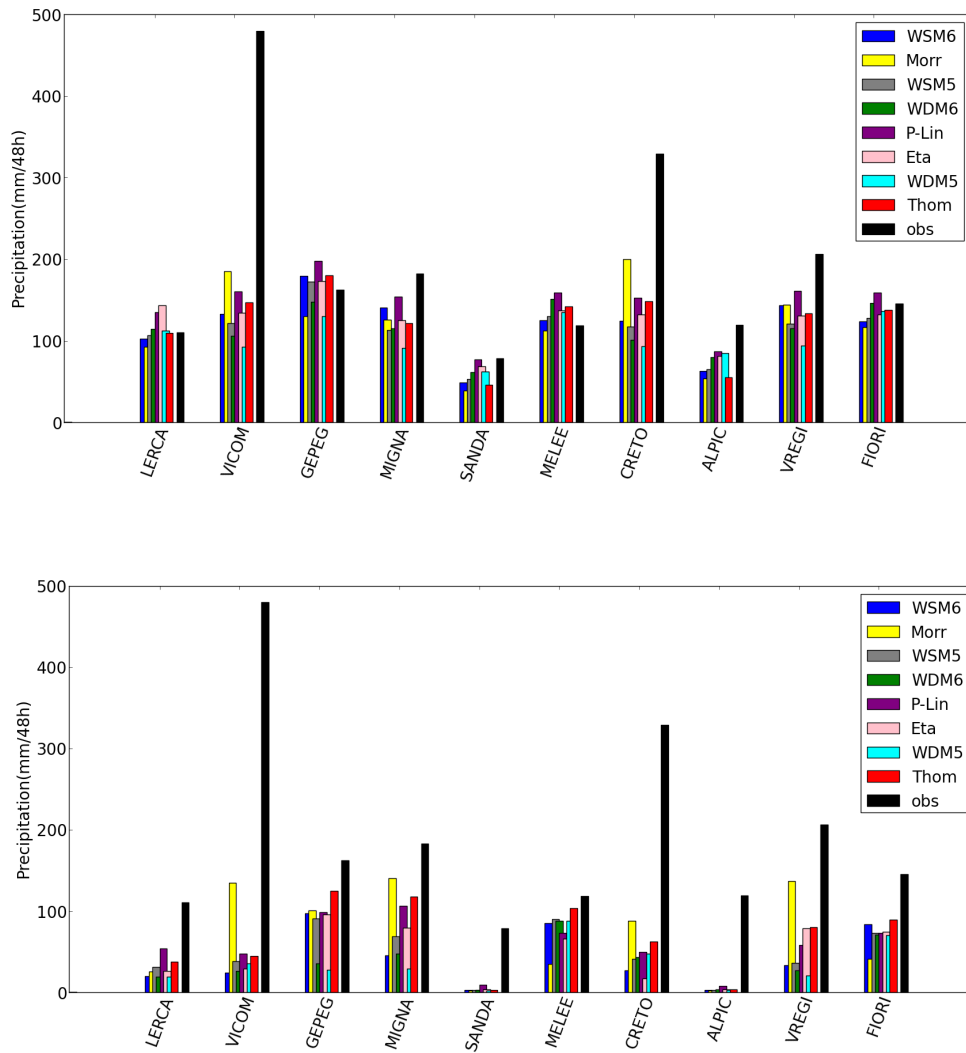


Figure 3.17: Total observed precipitation ( $mm/48 h$ ) during the 4 November 2011 event at selected stations (black bars) and corresponding forecasts obtained using different microphysical schemes and at different resolutions:  $10 km$  (top) and  $1.1 km$  (bottom).

ing is needed to make the verification of very-high resolution forecasts more robust (as already pointed out in Section 3.2); on the other hand an excessive smoothing of forecasts and observations fields could filter out relevant small-scale features (which are precisely what we intend to investigate and can only be reproduced by high-resolution simulations). Moreover, since the MODE approach itself involves a smoothing of precipitation fields (see Section 3.3), a coarser verification grid is expected to cause a loss of information. So we decided to remap predicted and observed precipitation over a 5 x 5 km grid, taking into account the mean distance between rain gauges in Liguria and especially in the urban area of Genoa, where the highest rainfall was reported in two out of the three considered events (with the only exception of the Cinque Terre case study in October 2011).

Following the MODE technique and using the NCAR MET tool, precipitation objects have been defined in both forecast and observation fields, corresponding to thresholds of 100 and 150 *mm/12 h*. This procedure allows us to focus only on very intense phenomena, filtering out lighter rain areas, that are not meaningful for the purposes of this study. Geometrical properties of these structures are then investigated, so as to obtain information on the model capability to reproduce the features detected in the observed precipitation fields.

Figure 3.18 illustrates examples of objects identified in observed and forecasted precipitation fields. This figure represents two extreme cases: in the left two panels (referring to the simulation on 4 October 2010 with the Eta Ferrier scheme on the finest resolution domain), there is no correspondence between structures in the forecast and the observation fields. On the contrary, in the right panels (referring to the simulation on 25 October 2011 over the same domain with the WSM6 scheme) the coupling is very good: the observed precipitation object is satisfactorily reproduced by the model, although a slight overestimation of the spatial extension of the intense rainfall area is evident.

To quantify the degree of ‘coupling’ for each pair of objects identified in forecast and observation fields, the total interest index has been calculated, weighting centroid distance, boundary distance, spatial extension difference, orientation of main axes difference, extension of the intersection area and precipitation intensity within the objects boundaries. The choice of the attributes and the corresponding weights for the calculation of the total

interest index (reported in Table 3.4) is based on that originally proposed by (Davis *et al.*, 2009), with the introduction of a further attribute related to precipitation intensity percentiles within each pair of objects, since our work is focused on extreme events and precipitation intensity spatial behavior is a relevant parameter to be compared.

Results of this analysis are summarized by histograms of Figures 3.19-3.20.

Table 3.4: Attributes weights used for the total interest index computation.

Attribute	weight
distance between centroids	16.7 %
distance between boundaries	33.3 %
angle difference between objects axes	8.3 %
area ratio	8.3 %
area overlap ratio	16.7 %
precipitation percentile intensity within object, above a fixed threshold	16.7 %

In Figure 3.19, the total number of the identified objects pairs, given threshold values of 100  $mm/12 h$  and 150  $mm/12 h$ , is reported as a function of the total interest value and the horizontal resolution of the simulations. The objects are tallied up on all the 48 simulations performed at a given resolution (8 microphysics schemes for each initialization time: 00 UTC of 3-4 October 2010, 24-25 October 2011, 3-4 November 2011). It is evident that the number of detected pairs increases as the model resolution is enhanced, especially if the 150  $mm/12 h$  threshold is considered. From this analysis the benefits of running higher resolution simulations are clearly evident, in contrast with the results obtained through the traditional approach, but in agreement with the qualitative eyeball verification. The peak observed for the total interest 0.9 – 0.95 bin is associated to the simulations of the 25 October 2011 flood. This event, being driven by dynamical and thermodynamical processes acting on somewhat larger scales than the other cases examined, was reproduced quite well also by coarser resolution simulations, so that the number of identified objects and their coupling degree is slightly dependent on the resolution, at least as far as the 100  $mm/12 h$  threshold is concerned.

Finally, we used the MODE technique for the analysis of the perfor-

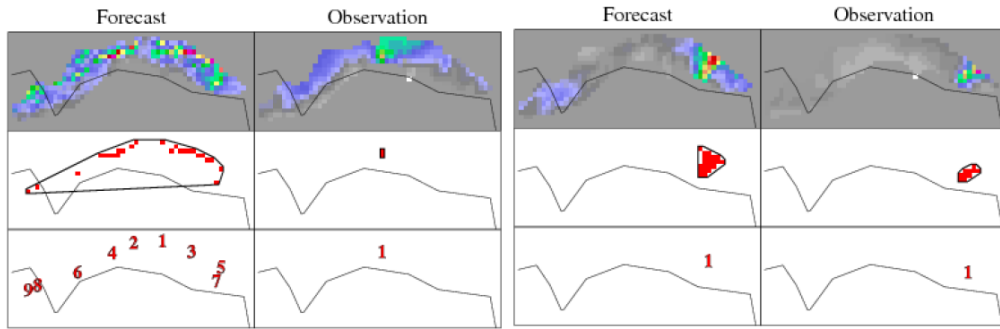


Figure 3.18: Left panels: example of a poor forecast according to the MODE object-oriented approach. No correspondence is found between structures in the forecast and the observation fields. The simulation initialized on 4 October 2010 at 00 *UTC* using the Eta Ferrier scheme on the 1.1 *km* resolution domain is considered and the precipitation threshold is 100 *mm/12 h*. Right panels: Example of a good forecast. The observed precipitation object is satisfactorily reproduced by the model, despite a slight overestimation of its spatial extension. The simulation initialized on 25 October 2011 at 00 *UTC* using the WSM6 scheme on the 1.1 *km* resolution domain is considered and the precipitation threshold is 100 *mm/12 h*.

manances of individual microphysics parameterization schemes, as far as simulations on the 1.1 *km* resolution domain are concerned. In Figure 3.20, the overall number of identified objects pairs versus total interest values is presented for each considered parameterization scheme. Focusing, in particular, on the highest threshold (bottom panel), best performances are attributable to Purdue-Lin, WSM5, WSM6 and Thompson schemes, for which pairs of objects are found with associated high total interest values, indicating a good matching between forecasts and observations (in agreement with the qualitative analysis given in Section 3.4). Looking at the upper panel of Figure 3.20, referred to the 100 *mm/12 h* threshold, also the Eta Ferrier microphysics seems to perform well, but this is due to the excessively high number of structures that this scheme produces. The WDM6 scheme also shows good performances but only if considering the lower threshold, while it is almost absent in the bottom panel histogram.

These results are highlighted in Table 3.5, where the total numbers of objects, predicted by each scheme and found in the observed precipitation fields, are reported regardless of their matching, which is measured by the

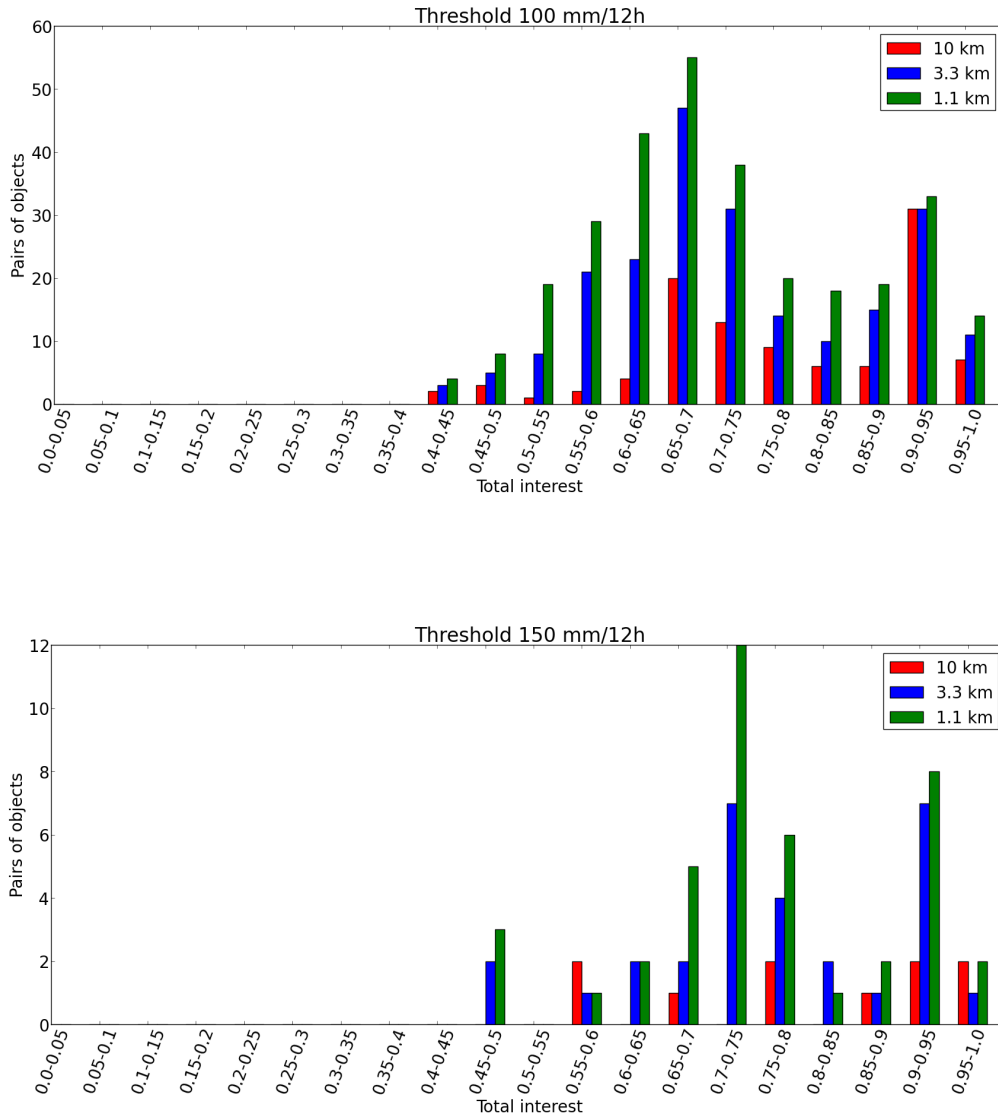


Figure 3.19: Overall number of identified objects pairs as a function of the total interest value and the model resolution for 100  $mm/12 h$  (top) and 150  $mm/12 h$  (bottom) rain thresholds, including all simulations performed for the three case studies.

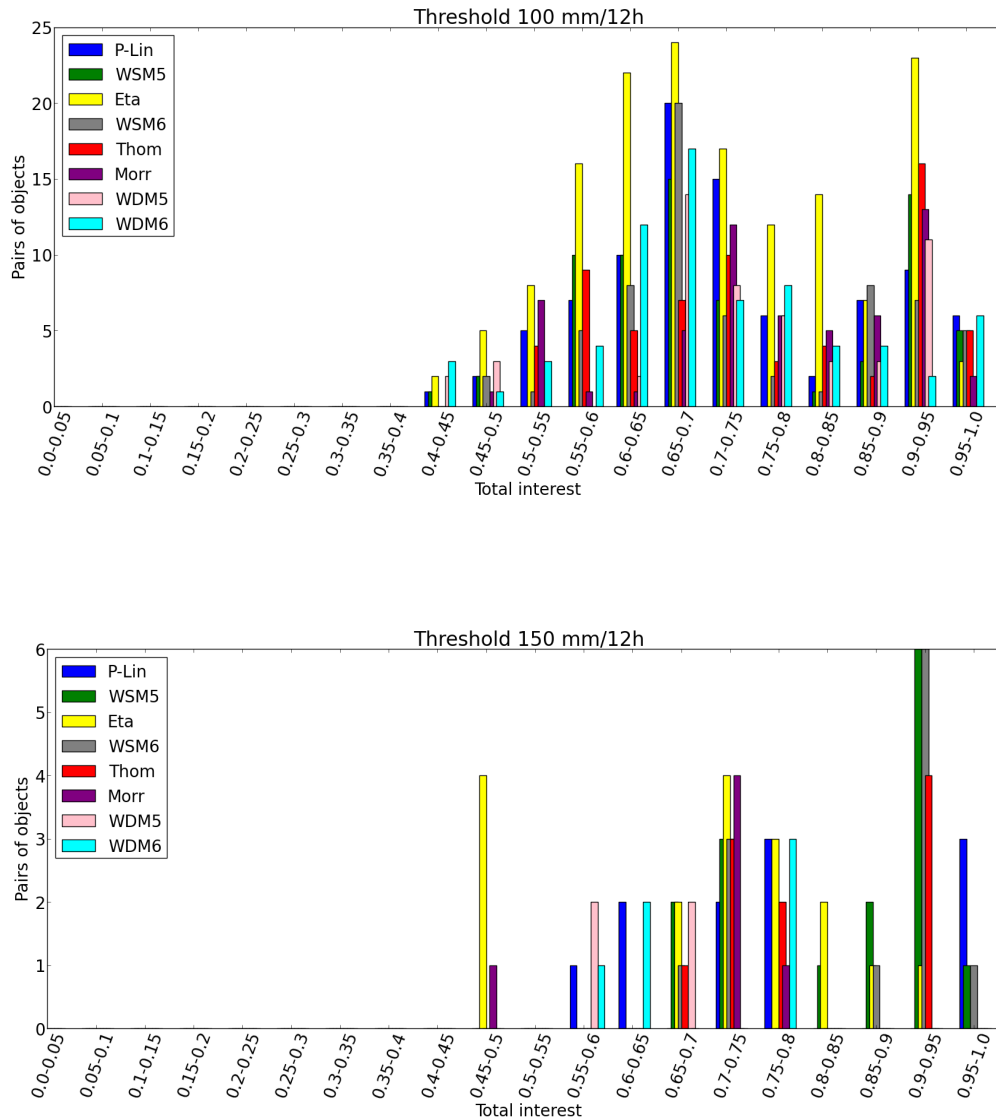


Figure 3.20: Overall number of identified objects pairs versus total interest values for each considered parameterization scheme for 100 mm/12 h (top) and 150 mm/12 h (bottom) rain thresholds, including all simulations performed on the 1.1 km resolution domain for the three case studies.

Table 3.5: Total numbers of objects, identified in predicted precipitation fields for each parameterization scheme and found in the observations fields, for 100  $mm/12 h$  and 150  $mm/12 h$  rain thresholds, including all simulations performed on the 1.1  $km$  resolution domain for the three case studies.

Scheme	# objects in forecasts (100 $mm/12h$ )	# objects in observations (100 $mm/12h$ )	# objects in forecasts (150 $mm/12h$ )	# objects in observations (150 $mm/12h$ )
<i>P-Lin</i>	20		5	
<i>WSM5</i>	21		7	
<i>Eta</i>	45		13	
<i>WSM6</i>	17		6	
<i>Thom</i>	15	20	5	12
<i>Morr</i>	13		4	
<i>WDM5</i>	11		2	
<i>WDM6</i>	14		2	

total interest index and shown in the aforementioned histograms. This kind of analysis is not aimed at providing an accuracy evaluation, but gives information about the model propensity to over- or underpredict precipitation, in a similar way as the Bias index does in the case of traditional point verification. Again, Purdue-Lin, WSM5, WSM6 and Thompson are the schemes producing a number of structures most resembling the number of observed objects, while *Eta* tends to overestimate the number of structures and, as a consequence, to overpredict precipitation.

An interesting outcome of our analysis is that double-moment schemes (with the exception of Thompson microphysics) seem to give relatively poor results. In particular, simulations with the WDM5 and WDM6 schemes in most cases predicted much less precipitation with respect to the corresponding single-moment ones and seem to underestimate especially the precipitation associated to convective systems. This is in contrast with what found in other works (e.g. [Bryan and Morrison, 2012](#); [Lim and Hong, 2010](#)). The latter study, in particular, demonstrates the greater ability of WDM6 with respect to WSM6 in reproducing the stratiform and convective regions of an idealized 2D thunderstorm. However, opposite results were obtained by [Morrison et al. \(2009\)](#), which found that their double-moment approach induced greater rain evaporation rates in the convective region with respect to the single-moment case. Moreover, according to [Morrison](#)

*et al.* (2009), the prediction of ice-phase number concentrations has significantly less impact on the results than the prediction of warm-phase concentrations in deep convective cases. This could offer an explanation of the good performance of Thompson microphysics emerged in the present study, this scheme being double-moment only for cloud ice. The Thompson scheme was found to be the best performing also in a study concerning severe convection in India and, in particular, outperformed the much more complex double-moment Morrison scheme (*Rajeevan et al.*, 2010).

A thorough interpretation of our results in terms of the different physical processes accounted by the different parameterization schemes we considered is beyond the scope of this work. This is a really complex task as too many non-linear and non-local mechanisms contribute together to originating a precipitation pattern to allow simple physical interpretations, and even simpler idealized simulations like those performed in the aforementioned works can give contradictory results. Therefore, dedicated studies are necessary, focused on the analysis of specific mechanisms, to single out the key microphysical processes acting in severe precipitation events as those analyzed in this chapter.

### 3.5 Conclusions

In this chapter we have reported the results of different numerical experiments exploiting the Advanced Research core of the Weather Research and Forecasting (WRF) model to simulate heavy precipitation events over Liguria. All the simulated case studies are characterized by the presence of quasi-stationary mesoscale convective systems over the Ligurian Sea, triggered and maintained by complex low-level temperature distributions and orographically-induced flows.

Our attention being focused on the precipitation field, in the present study the sensitivity of model predictions to the spatial resolution and the intercomparison of eight different parameterization schemes of cloud microphysics (either single- or double-moment) have been analyzed. The resolution issue is particularly important in situations like those considered here, where the topographic forcing has a crucial role in triggering heavy precipitations; furthermore a proper description of microphysical processes is of utmost importance for a precise estimate of precipitation amounts.

Three severe rainfall events occurred in the period between October 2010 and November 2011 have been analysed. The simulated precipitation fields obtained with different model configurations have been compared against a verification data set derived by the official regional rain gauge network, composed by 150 professional WMO-compliant stations, managed by the Ligurian Regional Environmental Protection Agency. Predicted and observed precipitation with different accumulation times have been chosen as relevant observables for the comparison.

Two different types of statistical analysis have been carried out to evaluate the efficiency of different model configurations and parameterization approaches: i) traditional categorical indices based on the definition of contingency tables where model forecasts and observations are compared at different points corresponding to the locations of the rain gauge stations; ii) a new-generation spatial verification technique where model patterns (or ‘objects’) are compared against patterns extracted from the gridded precipitation fields obtained from the observations. The following main results are worth recalling:

- a quite strong dependence of the quantitative precipitation forecasts on the adopted microphysics parameterizations clearly emerges;
- higher-resolution simulations are capable to provide more realistic and detailed precipitation patterns. This conclusion stems from the application of the object-based statistical analysis while the point-based analysis suggests opposite conclusions due to the known double-penalty issue;
- a set of parameterization schemes more suitable than others emerges for the case studies analyzed; the Purdue-Lin, WSM5, WSM6 and Thompson microphysics are the overall best performing ones.

In this work, the attention was focused on microphysics, but the same methodology could be used to investigate the impact on QPF of other physical parameterizations, such as those concerning the PBL. The interaction of the microphysical processes with the humidity and temperature tendencies provided by PBL schemes can modify not only low-level but also deep convective clouds and resulting surface precipitation amount (*Konor et al., 2009*). Moreover, PBL parameterizations may alter the large-scale

environment that is strongly coupled to the cloud and storm structural evolution (*Zampieri et al., 2005; Efsthathiou et al., 2013*).

The results here presented also emphasize the role of the initialization on final model performances. In the present study, mesoscale data assimilation has not been performed, but it can be expected to provide a relevant contribution, especially if high-resolution information about the moisture content of the atmosphere becomes available (e.g. precipitable water derived by Global Navigation Satellite Systems devices). Also, the consideration of a larger number of case studies, placed in different Mediterranean regions, should be worth considering with the aim of verifying the generality of our conclusions for extreme precipitation events sharing with those we have analyzed in Liguria the same triggering mechanisms.

Finally, as a further issue to be addressed in future activities, the investigation of the role of the (warm) sea and its two-way interaction with the atmosphere is surely of primary importance. This role has been discussed and assessed extensively in the literature for tropical storms (see, for example, *Trenberth, 2005*), while it has not been explored in detail in the case of mid-latitude storms over the Mediterranean area. However, it is clear that a warmer sea surface temperature (SST) increases air-sea surface heat fluxes and, as a consequence, the available energy and moisture for atmospheric convection and, thus, precipitation (*Seager et al., 1995*). In the next chapter it will be presented a study on the role that SST have on trigger, evolution and intensity of the severe flooding events treated in this chapter.

Results presented in the present chapter are reported in *Numerical simulations of Mediterranean heavy precipitation events with the WRF model: A verification exercise using different approaches*, Cassola, F., Ferrari, F., and Mazzino A., *Atmospheric Research, 164-165*, 210 – 225, (2015).

# Chapter 4

## The role of the Sea Surface Temperature on the flash floods events over Liguria

### 4.1 Introduction

After having analyzed in the previous chapter the impact that resolution and different ways of parameterize microphysics have on heavy precipitations produced by strong convective events, now we focus on the effect that air-sea interaction produce on the same kind of events.

Many studies in the last decades have highlighted the existing relationship between sea surface temperature (SST) and large-scale atmospheric phenomena. It is well known, for example, that intensity and track of tropical cyclones are strongly influenced by SST patterns (*Emanuel, 1986; Zhu and Zhang, 2006*). Also widely studied is the impact on the global atmospheric circulation of large and persisting SST anomalies, such as those associated to the El Niño Southern Oscillation (*Glantz, 2001; McPhaden et al., 2006*). Conversely, the effects that SST inhomogeneities can produce on mesoscale atmospheric systems in mid-latitudes are currently not fully understood. This is mainly because small-scale SST patterns (of the order of 1-10 *km*) are typically not well represented in the initial conditions used to force meteorological models. Also, only recently the time evolution of SST can be provided to atmospheric models as an updated boundary condition for real-time simulations, after the advent of coupled atmospheric-ocean mod-

els (*Brossier et al.*, 2009; *Warner et al.*, 2010; *Berthou et al.*, 2015; *Ricchi et al.*, 2016).

Unfortunately, mesoscale systems, often associated with intense convection, in some cases are able to produce huge amounts of precipitation in a very short time, causing severe damages and even casualties. In particular, as introduced in Chapter 3, Mediterranean coastal regions are regularly affected by localized heavy precipitation events, resulting in very dangerous flash floods, often of limited predictability (*Ricard et al.*, 2012). As also presented in the previous chapter, due to its position, exposed to southerly moist flows from the Mediterranean Sea, and the steep orography near the coasts, one of the most affected areas is Liguria region in northwestern Italy (*Silvestro et al.*, 2012; *Rebora et al.*, 2013; *Buzzi et al.*, 2014; *Cassola et al.*, 2015). Extreme precipitation is usually observed between late summer and mid autumn, when heat and moisture fluxes from the Mediterranean Sea are the highest, thus suggesting a fundamental role of SST in the generation and evolution of convective systems. However, while the importance of air-sea interactions has been intensively assessed in tropical regions, also from a climate change point of view (*Trenberth*, 2005), in the case of Mediterranean storms this topic clearly emerged just in recent years (*Lebeaupin et al.*, 2006; *Meredith et al.*, 2015). For instance, *Miglietta et al.* (2011) found that SST variations could weaken or intensify a Mediterranean "tropical-like" cyclone, while *Pastor et al.* (2015) investigated the sensitivity to artificial SST patterns for torrential rainfall events in the Valencia region (Spain). Also, *Davolio et al.* (2015) found that an accurate SST initialization is crucial for a correct description of an exceptional Bora wind storm in the Adriatic Sea. However, no study has addressed so far the role of SST in driving catastrophic rainfall episodes in the Ligurian Sea.

The main aim of this work is to analyze through numerical simulations how the mesoscale convective systems, responsible for some major flood events recently occurred in Liguria, respond to small SST variations (less than 1 °C), obtained by replacing a coarse large-scale field with a multi-satellite high-resolution analysis.

## 4.2 The analyzed case-studies

The case studies considered in this chapter are the same of the previous chapter, with the addition of a further event occurred subsequently to the progress of work presented in Chapter 3.

Indeed, in the evening of 9 October 2014 a new devastating flood hit the city of Genoa. The synoptic configuration leading to the generation of this event is similar to configurations that generated events presented in Chapter 3: a deep pressure minimum west of the region and a strong high pressure over eastern Europe; in Figure 4.1 mean sea level pressure and 500 – *mb* geopotential height over Europe, averaged during 4 October 2010, 25 October 2011, 4 November 2011 and 9 October 2014 events are shown in order to underlie the common synoptic situation during all considered events. Compared to the other cases, however, the last event shows a weaker synoptic scale forcing over Liguria.

The day before the event a deep low pressure area was present over Ireland (976 hPa), while a strong anticyclone affected western Russia (1042 hPa) (Figure 4.2, panel a)). In the morning of 9 October 2014, a wide trough extending from England to Canary Islands advected a warm and humid air mass from Libya to Liguria. At the same time, the pressure gradient between the Po Valley and the warmer Ligurian Sea induced a shallow northerly cold flow over west Liguria. The interaction of these two thermodynamically different air masses generated a convergence line associated to intense V-shaped convective systems that affected the city of Genoa in different times. A first V-shaped convective system hit the city between late morning and early afternoon; then, after a short break, in the late evening a second and more intense system developed, producing in about three hours a major flood in the eastern part of the city and in the surrounding areas. Precipitation amount reached 374 mm in Torriglia, northeast of Genoa (Figure 4.2, panel b)).

## 4.3 Model setting and simulations

These events, as in the previous work, were simulated using the ARW core of the WRF model, Version 3.4. For this study, a configuration similar to

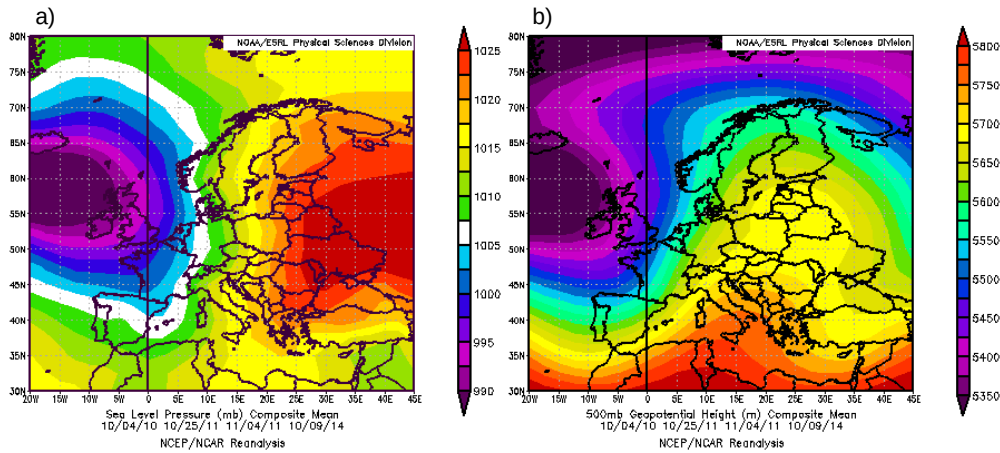


Figure 4.1: Mean sea level pressure (hPa) and 500-mb geopotential height over Europe during the considered case studies from the NCEP/NCAR Reanalysis: the plots are obtained averaging 00 UTC values over 4 October 2010, 25 October 2011, 4 November 2011 and 9 October 2014 (images provided by the NOAA/ESRL Physical Sciences Division, Boulder Colorado, from their web site at <http://www.esrl.noaa.gov/psd>).

those described in *Bove et al. (2014)* and *Cassola et al. (2015)* and presented in the previous chapter was used. Specifically, three two-way nested grids in a Lambert Conic Conformal projection were used, covering respectively: western and central Europe with 10 km, northern Italy with 3.3 km and the Liguria region with 1.1 km grid spacing (Chapter 3, Figure 3.5). The number of terrain-following vertical levels adopted was 35, with higher resolution close to the surface. As previously, the following parameterization schemes were implemented: Thompson microphysics (*Thompson et al., 2004*), Rapid Radiative Transfer Model (*Mlawer et al., 1997*) for longwave radiation, Goddard shortwave radiation (*Chou and Suarez, 1994*), Eta similarity surface layer (*Janjic, 2002*), Noah land surface model (*Chen and*

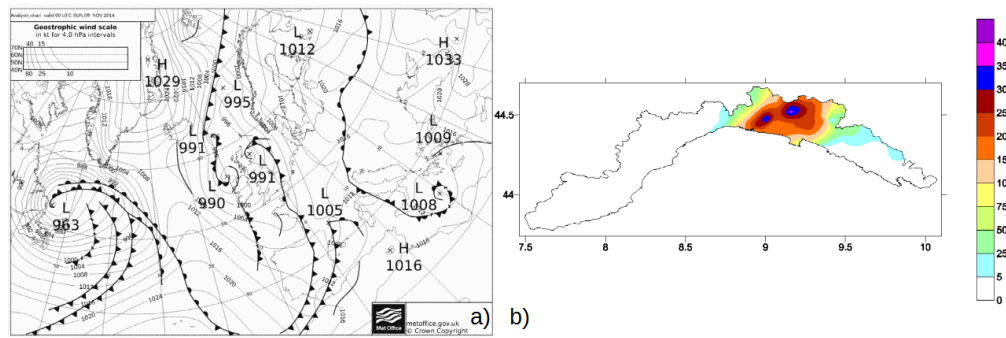


Figure 4.2: Panel a): synoptic situation over Europe at 00 UTC, 9 October 2014. UK Met Office Analysis (from <http://www.wetterzentrale.de/>). Panel b): precipitation amount ( $mm$ ) recorded over Liguria by the regional observing network from October 9, 00 UTC, to October 10, 00 UTC.

*Dudhia, 2001*) and Mellor-Yamada-Janjic planetary boundary layer (*Janjic, 2002*). The Kain-Fritsch cumulus scheme (*Kain, 2004*) was used in the outer domain only, whereas in the higher-resolution grids deep convection was explicitly resolved.

Initial and boundary conditions were taken from the operational GFS (Global Forecast System) analysis and 3-hourly forecast fields, respectively ( $0.5 \times 0.5$  degree resolution). Three 48-*h*-long WRF runs, with outputs saved every hour, were performed for each case study, starting respectively at 00 UTC of the same day of each event and at 00 and 12 UTC of the preceding day.

In order to quantify the sensitivity of the simulated precipitation patterns to variation in the SST field, we performed two sets of simulations: one using the low-resolution SST field from the GFS analysis and one ingesting high-resolution satellite-retrieved SST data coming from two different satellite SST data sets. For events occurred in 2010 and 2011 were adopted the reprocessed (REP) daily gap-free (L4) data at a resolution of  $0.0417 \times 0.0417$  degree. This product is based on AVHRR Pathfinder Version 5.2 (PFV52) data set obtained from the US National Oceanographic Data Center and the GHRSSST project (<http://pathfinder.nodc.noaa.gov>; <https://www.ghrsst.org/>). REP L4 data were interpolated on the original Pathfinder grid through an Optimal Interpolation algorithm and are representative of night SST values (00 UTC). For the October 2014 event, the

CNR MED L4 ultra-high-resolution (UHR, corresponding to 0.01 degree) SST data were also available and were adopted here. This database is obtained from infrared measurements collected by satellite radiometers, using statistical interpolation; data from different satellites, collected between 9 PM and 6 AM in order to avoid any diurnal warming contamination, are spatially and temporally merged through an Optimal Interpolation algorithm to create a daily 00 UTC SST field (*Buongiorno Nardelli et al., 2013*). Both data sets provide daily 00 UTC analyses. To initialize simulations at 12 UTC, SST fields corresponding to 00 UTC of adjacent days have been interpolated. The error introduced with this approach is reasonably small since the intra-daily SST variation should be quite negligible.

A posteriori, we found that for the October 2014 case the GFS-forced runs were not able to satisfactorily represent the development of convection. Thus, this event was also simulated using as atmospheric initial and boundary conditions the ECMWF (European Centre for Medium-range Weather Forecasts) analyses ( $0.125 \times 0.125$  degree resolution), to investigate the impact of changes in large-scale forcing in comparison with that due to SST variations.

Again, model sensitivity was evaluated against raingauge data provided by the observing network managed by the ARPAL. Radar reflectivity images, made available by ARPAL every ten minutes, have also been considered for the October 2010 event, on which most of the following analysis will be focused. Unfortunately, the radar sited on Monte Settepani in the Ligurian Apennines, just a few tens of km from the area of interest, was out of order in that period and only data from a farther radar located close to Turin were available. Therefore, radar images were used just for a qualitative comparison with the simulated precipitation fields.

## 4.4 The role of the sea surface temperature

The results of all the numerical experiments performed in this study are summarized in Table 4.1, where the 24-h accumulated precipitation simulated by WRF at 1.1 km resolution with different initialization setups is compared with the corresponding observed values for each event. The impact on simulated precipitation of the satellite-derived SST appears to be significant in most cases. It is worth noting that the ingestion of a more

detailed SST analysis in the model leads to more intense and, consequently, more realistic precipitation peaks especially for simulations initialized the day before the event (36-h and 48-h forecasts). The effect on shorter-term simulations is less evident and, at least in one case (October 2011), is significantly negative. The effect of SST on the precipitation peaks location is limited, due to the role of the orography in anchoring precipitation once the convective system is advected towards the coast and inland.

Further work is needed to disentangle the complex interactions between

Table 4.1: Maximum 24-*h* accumulated rainfall simulated with WRF model at 1.1 *km* grid spacing for each considered event. Initial conditions (global model with or without satellite-derived SST) and simulations acronyms are specified in the first and in the second column respectively. Third, fourth and fifth columns refer to runs initialized at 00 *UTC* of the day when the event occurred (+24 *h*) and at 12 and 00 *UTC* of the previous day (+36 *h* and +48 *h*), respectively. The observed precipitation maximum is shown in the last column.

Initial conditions	Simulations	Max +24 <i>h</i> fcst ( <i>mm</i> )	Max +36 <i>h</i> fcst ( <i>mm</i> )	Max +48 <i>h</i> fcst ( <i>mm</i> )	Max obs ( <i>mm</i> )
4 October 2010					
GFS	GFS-CTL1	218.1	166.5	209.5	411.2
GFS + sat. SST	GFS-SAT1	237.1	172.3	276.1	•
25 October 2011					
GFS	GFS-CTL2	361.9	243.7	224.4	538.2
GFS + sat. SST	GFS-SAT2	273.6	275.9	254.2	•
4 November 2011					
GFS	GFS-CTL3	310.0	274.0	256.1	477.6
GFS + sat. SST	GFS-SAT3	284.3	306.3	281.9	•
9 October 2014					
GFS	GFS-CTL4	142.2	157.7	97.8	374.0
GFS + sat. SST	GFS-SAT4	135.0	112.6	94.7	•
ECMWF	ECM-CTL	205.2	125.3	118.2	•
ECMWF + sat. SST	ECM-SAT	250.2	103.5	100.0	•

large-scale forcing and SST-induced phenomena leading to precipitation. The rainfall simulated in the short range (+24 *h*) run is closer to the observations, possibly due to a better description of the atmospheric conditions

conducive to heavy rain by the most recent large-scale analysis driving the simulation. The reasons for the limited, or sometimes negative impact of satellite SST in shorter-range simulations might be due to a sort of "spinup" problem, that is, the boundary layer requires some time to adjust to a satellite-retrieved SST (which is not consistent with the large-scale atmospheric forcing). For runs forced with large-scale SST analysis, both SST and atmospheric fields are defined by the same model and no spinup occurs. On the contrary, for simulations initialized the day before, the marine boundary layer has enough time before the triggering of convection to adjust to the high-resolution SST fields and influence mesoscale dynamics and convective processes. This issue emerges more clearly for the 2010 and 2011 case studies, while different considerations are needed for the October 2014 event. In that case, the benefits of a detailed SST field are relevant just in the very short term and only using higher-resolution ECMWF initial and boundary conditions.

Indeed, the October 2014 event is somewhat different and more complex than the previous ones, being characterized by a weaker synoptic forcing, and the accuracy of large-scale initial and boundary conditions appears as the main issue. In this case, the ECM-CTL run initialized at 00 UTC of 9 October 2014 provides significantly better results in terms of localization and timing of the convective cells and of quantitative precipitation forecast with respect both to the GFS-forced runs initialized on the same day and to runs forced with ECMWF and GFS analyses on the previous day: as shown in the Figure 4.4, in the ECMWF analysis a stronger pressure gradient than in the GFS one is found between the Po Valley and the Ligurian Sea. This induces more pronounced low-level convergence and humidity advection, which consequently enhance the convective development. Interestingly, in this case the ingestion of satellite-derived SST is beneficial only for ECMWF runs (cf. Figures 4.3, panel c) and 4.3, panel d) with Figures 4.3, panel a) and 4.3, panel b), respectively). Instead, the maps reported in Figure 4.5 show that, for simulations initialized the day before the event, precipitation peaks are strongly underestimated and displaced westwards (again, cf. Figure 4.2, panel b)). Less pronounced differences are found between ECMWF- and GFS-driven runs with respect to those shown in Figure 4.3, with the former providing just slightly better results. In this case, the ingestion of satellite SST has a minor impact.

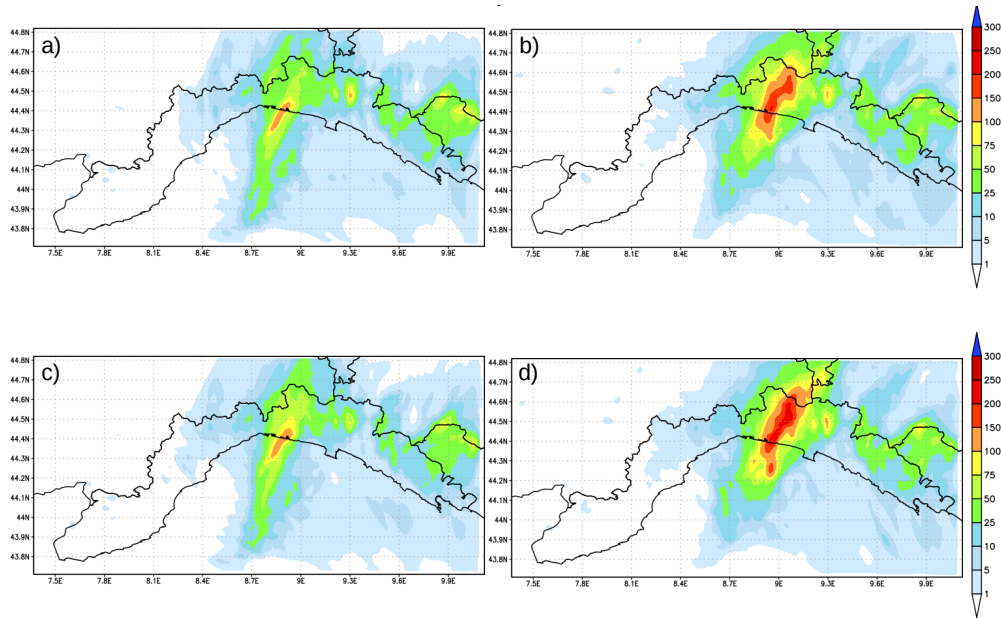


Figure 4.3: 24-h accumulated precipitation ( $mm$ ) predicted for the period ending at 00 UTC, 10 October 2014 by WRF model initialized using GFS, *a*) and ECMWF analyses *b*) at 00 UTC, 9 October 2014. Panels *c*), *d*): Same as *a*), *b*), but using satellite-derived SST data.

The fact that the SST effect is beneficial only for the ECMWF-driven simulation initialized on October 9 may suggest that considering a detailed SST initial field can improve the prediction of severe rainfall episodes in the area, provided that the large-scale forcing is “accurate” enough to allow an adequate description of the convective initiation by the mesoscale model. The aforementioned spinup issue appears less important in this case, maybe also because a large part of the precipitation was observed in the evening (contrary to 2010 and 2011 events), that is at a longer distance from the analysis. Furthermore, ECMWF SST has a finer resolution than GFS, closer to that of satellite analysis, thus the inconsistency between large-scale atmospheric fields and SST is limited compared to GFS-driven

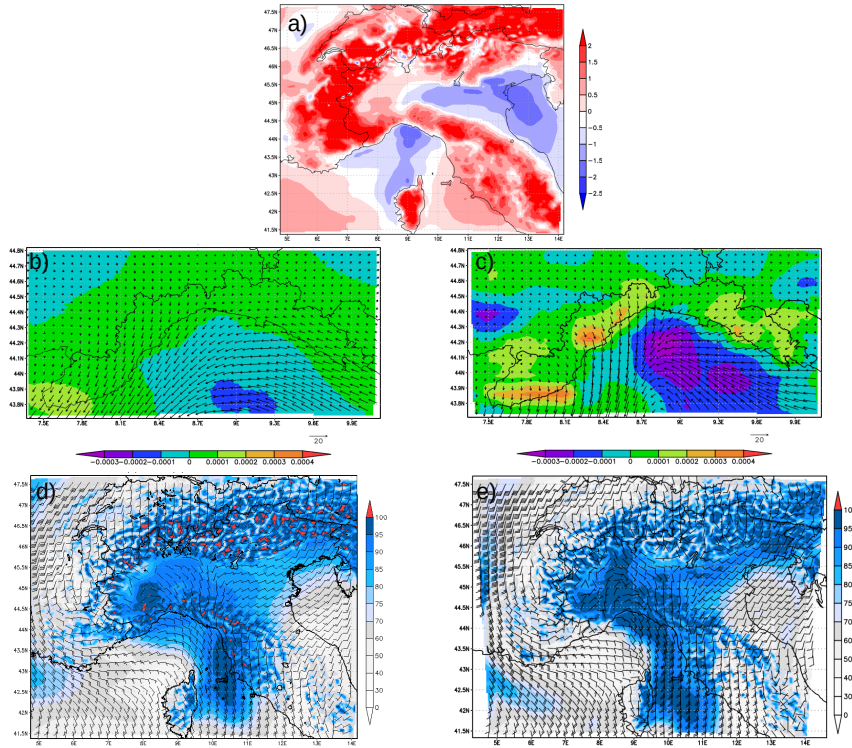


Figure 4.4: Panel *a*): MSLP difference (hPa) on the 3.3 km grid at the initial simulation time using ECMWF and GFS analyses and large scale SST at 00 UTC, 9 October 2014 (ECMWF minus GFS). Wind field divergence (shaded contours,  $s^{-1}$ ) and 10-m wind field (vectors,  $m s^{-1}$ ) at the same instant on the 1.1 km grid, using GFS, *b*), and ECMWF, *c*), analyses. 925-hPa relative humidity (shaded contours, %) and wind field (vectors,  $m s^{-1}$ ) on the 3.3 km grid, adopting GFS, *d*), and ECMWF, *e*), analyses.

runs.

From Table 4.1, the simulation improvement associated to the use of a high-resolution SST is particularly significant for the October 2010 event (+48 *h* run): the synoptic and mesoscale configuration concerning this event is described in the previous chapter. In the following, a deeper analysis of the October 2010 event is presented, to investigate the mechanisms underlying the simulation improvement induced by the use of a higher-resolution SST field. Indeed, this case study was quite poorly reproduced by GFS-driven runs, while the introduction of the satellite-derived SST allows for a better description of the convective system structure and, consequently, more

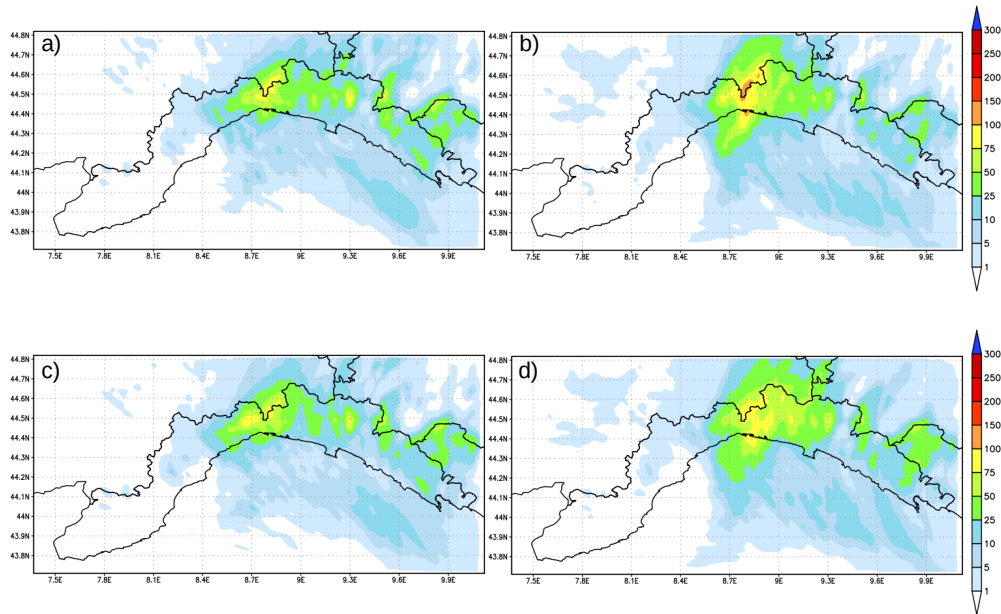


Figure 4.5: 24-h accumulated precipitation ( $mm$ ) predicted for the period ending at 00 UTC, 10 October 2014, by WRF model initialized using GFS, *a*) and ECMWF analyses *b*) at 00 UTC, 8 October 2014. Panels *c*), *d*): same as *a*), *b*), but using satellite-derived SST data.

realistic precipitation estimates. All figures hereinafter were obtained from WRF simulations at 1.1 km initialized at 00 UTC of 3 October 2010, if not otherwise specified.

In Figures 4.7, panel *c*) and 4.7, panel *d*), 12-h accumulated precipitation at 12 UTC of 4 October 2010, obtained from GFS-CTL1 and GFS-SAT1 runs, is compared, while the difference in the SST initial field is shown in Figure 4.7, panel *a*). Positive SST differences are found in a large portion of the Ligurian Sea, especially close to western coasts, where the satellite analysis is about  $1^{\circ}\text{C}$  warmer than GFS. Conversely, slightly cooler temperatures are found in the open sea. The different SST distribution is consistent with the surface latent heat flux discrepancies between the two simulations in the proximity of the convective initiation (06 UTC of 4 October 2010),

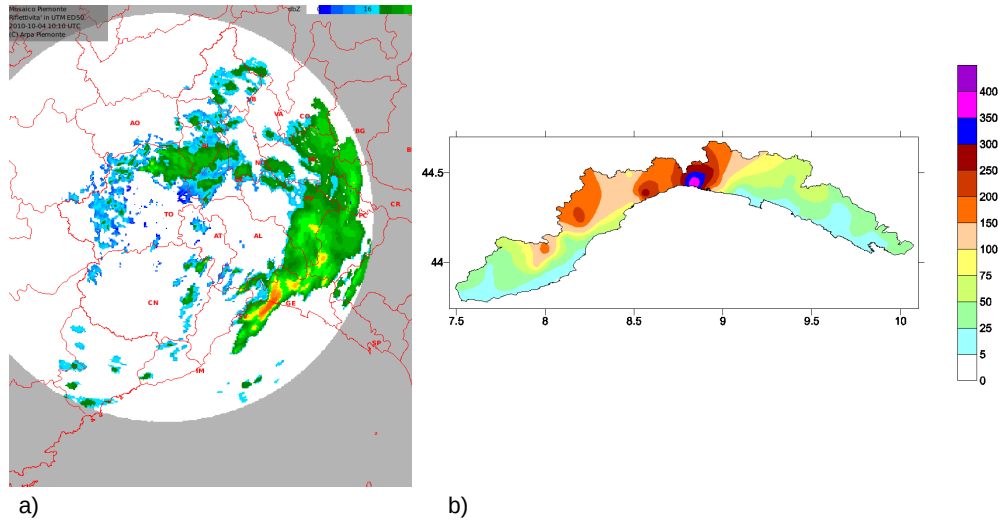


Figure 4.6: a) Radar reflectivity (dbZ) at 10:10 UTC of 4 October 2010. b) 24-h accumulated precipitation ( $mm$ ) recorded by the regional observing network in the period ending at 00 UTC, 5 October 2010. Adapted from [Cassola et al. \(2015\)](#).

depicted in Figure 4.7 panel b): stronger fluxes are found in areas where satellite SST is warmer (up to  $100 W m^{-2}$  off the western coast), which implies a warming and moistening of the boundary layer favoring convective destabilization. As a result, a remarkable increase in precipitation intensity (up to  $70 mm$  in 12 h), a more intense and better defined rainband, and a slight eastward shift of the precipitating system can be noticed in the GFS-SAT1 experiment. The latter simulates better the effective localization and intensity of the observed phenomena (cf. Figures 4.6, panel a) and 4.6, panel b) with Figure 4.7, panel d)).

A crucial role for the simulation improvement is also played by the low-level convergence observed over the sea. Figure 4.8 panel a) shows the mean sea level pressure (MSLP) difference between WRF simulations on the 3.3 km

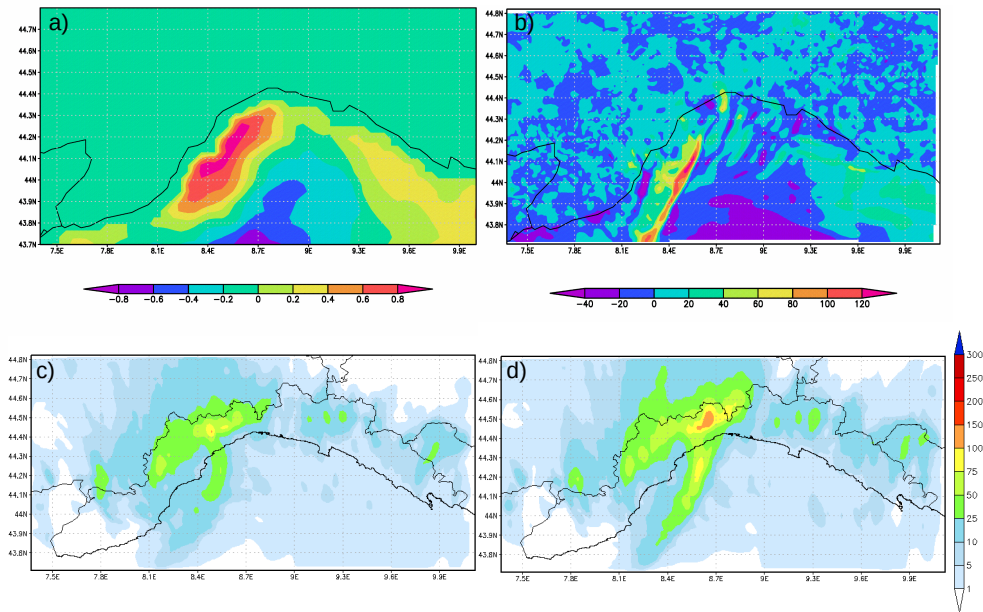


Figure 4.7: *a*) SST difference ( $^{\circ}\text{C}$ ) between satellite-derived and GFS analyses at 00 UTC, 3 October 2010. *b*) Surface latent heat flux difference ( $\text{W m}^{-2}$ ) between GFS-CTL1 and GFS-SAT1 runs at 06 UTC, 4 October 2010. 12-h accumulated precipitation ( $\text{mm}$ ) predicted over Liguria at 12 UTC, 4 October 2010 by *c*) GFS-CTL1 and *d*) GFS-SAT1 simulations.

grid with and without satellite-derived SST, again at 06 UTC of 4 October 2010. A warmer (at least on average) SST corresponds to lower pressure values over the sea, so that the pressure gradient is higher. The modification of the pressure fields induces stronger winds, which are responsible for a line with stronger convergence and its slight eastward shift which, in turn, enhances convective development (Figures 4.8, panel *b*) and 4.8, panel *c*). *Miglietta et al.* (2011) noted that a warmer SST produced faster cyclones, suggesting a stronger transfer of energy (and increased momentum) from the sea to the atmosphere. This picture is also consistent with the results by *Buzzi et al.* (2014), who suggested that the magnitude of the low-level temperature gradient between the Po Valley and the Ligurian Sea can de-

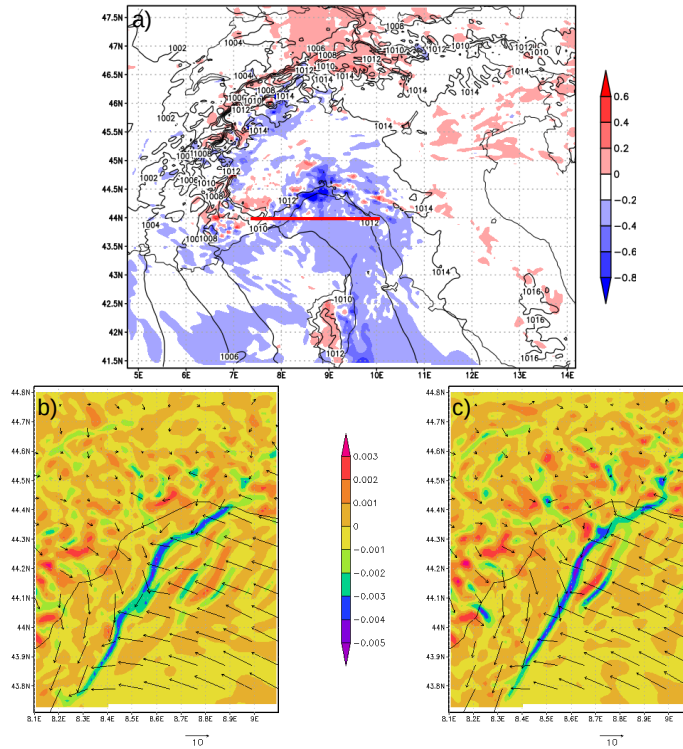


Figure 4.8: *a*) MSLP difference (hPa, shaded contours) between GFS-CTL1 and GFS-SAT1 simulations on the 3.3 km grid and MSLP (hPa, line contours) obtained from GFS-SAT1 at 06 UTC, 4 October 2010. The red line identifies the position of vertical cross sections shown in Figures 4.9a, 4.9b. 10-m wind (vectors,  $m s^{-1}$ ) and divergence (shaded contours,  $s^{-1}$ ) fields on the 1.1 km grid at the same instant, from *b*) GFS-CTL1 and *c*) GFS-SAT1 runs.

termine the extension and intensity of the cold northerly outflow and, as a consequence, the exact position of the convergence line.

West-east cross sections of equivalent potential temperature and cloud water mixing ratio, taken at  $44.0^\circ N$  and intersecting the convergence line, are shown in Figures 4.9, panel *a*) and 4.9, panel *b*). The cold pool associated to the shallow northerly flow and the moist, warm southeasterly low-level jet can be easily recognized. Higher equivalent potential temperatures, indicating larger heat and moisture fluxes from the sea able to fuel deep convection, as well as a higher cloud water content, east of and aloft the convergence line, are found in the GFS-SAT1 simulation (Figure 4.9, panel

b)).

Finally, Figure 4.9, panel c) and panel d) shows the simulated soundings

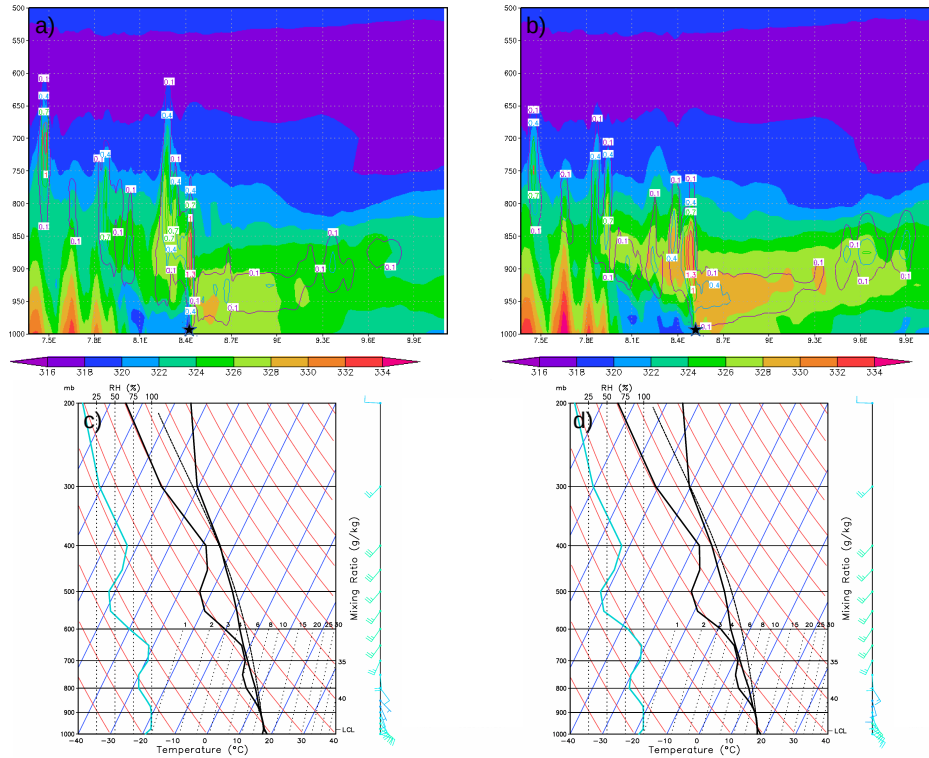


Figure 4.9: Equivalent potential temperature (K, shaded contours) and cloud water mixing ratio ( $g\ kg^{-1}$ , line contours) cross sections, taken at  $44.0^{\circ}N$  and at 06 UTC, 4 October 2010 from a) GFS-CTL1 and b) GFS-SAT1 simulations; black stars indicate the convergence zone between southeasterly and northerly flows. Simulated soundings extracted at 08 UTC, 4 October 2010 east of the convergence line ( $44.1^{\circ}N$ ,  $8.6^{\circ}E$ ) from c) GFS-CTL1 and d) GFS-SAT1. Temperature and dewpoint profiles are plotted as thick, solid black lines, while pseudoadiabats are thin, dashed black lines.

extracted from the two runs two hours later (08 UTC, when the convective system was reaching its maximum intensity) at ( $44.1^{\circ}N$ ,  $8.6^{\circ}E$ ), just east of the convergence line at that time. Again, temperature and humidity profiles obtained from the GFS-SAT1 simulation appear more unstable.

In particular, surface temperature and dewpoint are about  $0.5^{\circ}C$  to  $1.0^{\circ}C$  warmer and CAPE<sup>1</sup> values reach  $562\ J\ kg^{-1}$  with respect to  $329\ J\ kg^{-1}$

<sup>1</sup>CAPE, Convective Available Potential Energy, is an indicator of atmospheric insta-

in the GFS-CTL1 run.

## 4.5 Conclusions and perspectives

The present study investigated the sensitivity to the SST field ingested by a numerical weather prediction model in the development of severe flash-flood events in Liguria (Italy), induced by quasi-stationary mesoscale convective systems. Most of the considered cases reveal significant sensitivity, with variations of less than 1 °C in SST causing corresponding variations in the ground-accumulated precipitation field up to 50-70 mm in 12 h.

The response of heavy precipitation to SST is a complex one, which involves the modification of PBL and low-level flow characteristics and its interaction with topography. The impact of satellite-derived SST on total predicted precipitation appears beneficial especially for simulations initialized the day before the event, due to the relatively slow adjustment of atmospheric fields to the higher-resolution initial condition. Conversely, such an impact is generally neutral or even negative for 24-h forecasts.

The analysis of the most recent episode (October 2014) suggests that a satellite-retrieved SST initial field can improve the quantitative precipitation forecast only when the large-scale forcing is accurate enough. In fact, the assimilation of satellite SST appears beneficial for this event just in combination with the best available large-scale analysis (ECMWF at 00 UTC of 9 October), capable to reasonably describe the convective initiation and development.

The results presented in this chapter are reported in *The role of the sea on the flash floods events over Liguria (northwestern Italy)*, Cassola, F., Ferrari, F., Mazzino, A., and Miglietta, M.M., *Geophysical Research Letters*, 43, 3534 – 3542, (2016) and encourage further research about the

---

bility, function of the difference in virtual temperature between the rising (or sinking) air parcel,  $T_{v,parcel}$ , relative to the air around it,  $T_{v,env}$  at the same elevation:

$$CAPE = \int_{LFC}^{z_{max}} g \frac{T_{v,parcel} T_{v,env}}{T_{v,env}^2} dz$$

where  $LFC$  is the Level of Free Convection, i. e. the level in the atmosphere where the temperature of the environment decreases faster than the moist adiabatic lapse rate of a saturated air parcel at the same level, and  $z_{max}$  is the altitude at which the rising parcel is no longer warmer than the environment.

role of air-sea interaction in driving the formation and evolution of severe convective systems in Liguria and in other Mediterranean regions, possibly exploiting two-way atmosphere-ocean coupled modeling systems. The latter are capable to provide the atmospheric model with a high-resolution, continuously updated SST field, which represents the coastal SST much better than satellite analyses ([Ricchi et al., 2016](#)) and is consistent with the atmospheric fields for the whole simulation.



# Conclusions

In recent years considerable progresses in numerical modeling of atmosphere have been made. Progresses are mainly due to more efficient numerical methods and more accurate description of physical processes that are the basis of subgrid phenomena. These advancements are crucial specially for the possibility of forecasting severe and potentially dangerous events and consequently for the reduction of the hazards associated with these events. In the present thesis the WRF model capability in simulate very intense and localized convective systems was analyzed. In particular I have performed simulations of the four most recent floods that hit Liguria region (Varazze and Sestri Ponente, 4 October 2010, Cinque Terre and Val di Vara, 25 October 2011, and Genoa, 4 November 2011 and 9 October 2014), focusing on the effect of grid resolution, microphysics parameterization schemes and SST initial field. For this purpose several simulations over three two-way nested domains characterized by horizontal resolution of 10, 3.3 and 1.1 *km* were performed. Our attention being focused on the precipitation field, performances of the model were then studied for different microphysics parameterization schemes, forecast ranges and SST initial fields. For the assessment concerning the effect of different microphysics parameterization schemes, two different strategies have been exploited. A traditional approach, where forecasts and observations are matched on a point-by-point basis was flanked by an object-based method where model success is based on the correct localization and intensity of precipitation patterns. Main results emerged in this work are summarized in the following:

- higher-resolution simulations are capable to provide more realistic and detailed precipitation patterns. The amount of precipitation forecasts by simulations performed over finer grid in many cases is about double

than that obtained on the coarser grid, almost always approaching precipitation observed.

- Point-based analysis results misleading in analyzing high resolution simulations inasmuch fine-scale differences that are not present in coarser resolution forecasts are penalized by traditional scores, strongly sensitive to localization and timing errors up to the space and time resolution of the sample (double penalty problem). New generation object-based statistical analysis results more suitable for high resolution simulations analysis.
- A quite strong dependence of the quantitative precipitation forecasts on the adopted microphysics parameterizations emerges, regarding both intensity both localization. For the case studies analyzed, a set of parameterization schemes more suitable than others emerges; the Purdue-Lin, WSM5, WSM6 and Thompson microphysics are the overall best performing ones.
- Most of the considered cases reveal significant sensitivity to SST initial field. Variations of less than 1 °C in SST cause corresponding variations in the ground-accumulated precipitation field up to 50-70 mm in 12 h. In most cases, the variations in SST field produce an alteration in pressure field forecasts and a moistening of the southerly flows, resulting in a strengthening of the convergence phenomenon and then in an enhancement of precipitation forecasts.
- The analysis of the most recent episode (October 2014) suggests that a satellite-retrieved SST initial field can improve the quantitative precipitation forecast only when the large-scale forcing is accurate enough. In fact, the assimilation of satellite SST appears beneficial for this event just in combination with the best available large-scale analysis (ECMWF at 00 UTC of 9 October), capable to reasonably describe the convective initiation and development.
- The impact of satellite-derived SST on total predicted precipitation appears beneficial especially for simulations initialized the day before the event, due to the relatively slow adjustment of atmospheric fields to the higher-resolution initial conditions. Conversely, such an impact is generally neutral or even negative for 24-h forecasts.

Further work will be needed to investigate the impact on the small size, quasi-stationary, V-shaped convective systems analyzed in this thesis, of other physical parameterizations. For example also PBL parameterization schemes can have heavy influence on QPF. The interaction of the micro-physical processes with the humidity and temperature tendencies provided by PBL schemes can modify not only low-level but also deep convective clouds and resulting surface precipitation amount.

Furthermore, the emerged strong sensitivity on QPF to SST field encourages further research about the role of air-sea interaction in driving the formation and evolution of severe convective systems in Liguria and in other Mediterranean regions. The possibility to exploit two-way atmosphere-ocean coupled modeling systems could be fundamental in order to provide to the atmospheric model an high-resolution, continuously updated SST field. A coupled modeling system makes also possible to evaluate potential feedback phenomena between atmosphere and ocean during the event.

Results presented in the present thesis are published in:

1. *Numerical simulations of Mediterranean heavy precipitation events with the WRF model: A verification exercise using different approaches*, Cassola, F., Ferrari, F., and Mazzino A., *Atmospheric Research*, 164-165, 210 – 225, (2015)
2. *The role of the sea on the flash floods events over Liguria (northwestern Italy)*, Cassola, F., Ferrari, F., Mazzino, A., and Miglietta, M.M., *Geophysical Research Letters*, 43, 3534 – 3542, (2016).



# Bibliography

- Accadia, C., S., Mariani, M., Casaioli, and A., Lavagnini, Sensivity of precipitation forecast skill scores to bilinear interpolation and a simple nearest-neighbor average method on high-resolution verification grids, *Wea. Forecasting*, 18, 918–932 (2003).
- Altinbilek, D., E. C., Barret, T., Oweis, E., Salameh, and F., Siccardi, Rainfall climatology on the Mediterranean, EU-AVI 080 Project ACROSS?analyzed climatology rainfall obtained from satellite and surface data in the Mediterranean basin *EC report*, EU-AVI 080 (1997).
- Andrews, D. G., *An introduction to Atmospheric Physics*. Cambridge University Press, second edition (2010).
- Anthes, R. A., A cumulus parameterization scheme utilizing a one-dimensional cloud model, *Mon. Wea. Rev.*, 105, 270–286 (1977).
- Anthes, R. A., Regional Models of the atmosphere in the middle latitudes. *Mon. Wea. Rev.*, 111, 1306–1335 (1983).
- Anthes, R. A., Y. -H. Kuo, E. -Y. Hisie, S Low-Nam, and T. W. Bettge (1989), Estimation of skill and uncertainty in regional numerical models, *Quart. J. Roy. Meteor. Soc.* 115, 763–806, (1989).
- Arakawa, A., and W. H. Schubert,, Interaction of a cumulus cloud ensamble with the large scale environment. Part I, *J. Atmos. Sci.*, 31, 674–701 (1974).
- Arakawa, A., The Cumulus Parameterization Problem: Past, Present, and Future, *J. of Climate*, 17, 2493 – 2525 (2004).

- Berthou, S., S. Mailler, P. Drobinski, T. Arsouze, S. Bastin, K. Beranger, and C. Lebeau-pin-Brossier, Sensitivity of an intense rain event between atmosphere-only and atmosphere-ocean regional coupled models: 19 september 1996, *Quarterly Journal of the Royal Meteorological Society*, *141*(686), 258–271 (2015).
- Betts, A. K., A new convective adjustment scheme. Part I. Observational and theoretical basis, *Quart. J. Roy. Meteor. Soc.*, *112*, 677–691 (1986).
- Betts, A. K., and M. J., Miller, A new convective adjustment scheme. Part II. Single column tests using GATE wave, BOMEX, ATEX and arctic air-mass data sets, *Quart. J. Roy. Meteor. Soc.*, *112*, 693–709 (1986).
- Bove, M. C., P. Brotto, F. Cassola, E. Cuccia, D. Massabò, A. Mazzino, A. Piazzalunga, and P. Prati, An integrated PM<sub>2.5</sub> source apportionment study: Positive Matrix Factorization vs. the chemical transport model CAMx, *Atmos. Environ.*, *94*, 474–286 (2014).
- Brandolini, P., A. Cevasco, M. Firpo, A. Robbiano, and A. Sacchini, Geohydrological risk management for civil protection purposes in the urban area of Genoa (Liguria, NW Italy), *Nat. Hazards Earth Syst. Sci.*, *12*, 943–959 (2012).
- Benguier, J. L., and L., Chaumat, Droplet spectra broadening in cumulus clouds. Part I: broadening in adiabatic cores, *J. Atmos. Sci.*, *58*, 628 – 641 (2001).
- Brossier, C. L., V. Ducrocq, and H. Giordani, Two-way one-dimensional high-resolution air-sea coupled modelling applied to Mediterranean heavy rain events, *Quarterly Journal of the Royal Meteorological Society*, *135*(638), 187–204 (2009).
- Brown, B. G., F., Atger, H., Brooks, *Recommendations for the verification and intercomparison of QPFs from operational NPW models*, Res. Appl. Lab. (2008).
- Bryan, G., and H., Morrison, Sensitivity of a Simulated Squall Line to Horizontal Resolution and Parameterization of Microphysics, *Mon. Wea. Rev.*, *140*, 202 – 225 (2012).

- Buongiorno Nardelli, B., C. Tronconi, A. Pisano, and R. Santoleri, High and Ultra-High resolution processing of satellite Sea Surface Temperature data over Southern European Seas in the framework of Myocean project, *Remote Sensing of Environment*, *129*, 1 – 16 (2013).
- Buzzi, A., S. Davolio, P. Malguzzi, O. Drofa, and D. Mastrangelo, Heavy rainfall episodes over Liguria of autumn 2011: numerical forecasting experiments, *Nat. Hazards Earth Syst. Sci.*, *14*, 1325–1340 (2014).
- Casati, B. L. J., Wilson, D. B., Stephenson, P., Nurmi, A., Ghelli, M., Pocerich, U., Darmath, E. E., Ebert, B. G., Brown, and S., Mason, Review forecast verification: current status and future directions, *Meteorol. Appl.*, *15*, 3–18 (2008).
- Cassola, F., F. Ferrari, and A. Mazzino, Numerical simulations of Mediterranean heavy precipitation events with the WRF model: A verification exercise using different approaches, *Atmospheric Research*, *164-165*, 210 – 225 (2015).
- Celani, A., G., Falkovich, A., Mazzino, and A., Seminara, Droplet condensation in turbulent flows, *Europhys. Lett.*, *70*, 775 – 781 (2005).
- Celani, A., A., Mazzino, A., Seminara, and M., Tizzi, Droplet condensation in two-dimensional Bolgiano turbulence, *J. Turbol.*, *8*, 1 – 9 (2007).
- Celani, A., A., Mazzino, A., and M., Tizzi, The equivalent size of cloud condensation nuclei, *New J. Phys.*, *10*, 075021 (2008).
- Chappell, C. F., *Quasi-stationary convective events. Mesoscale Meteorology and Forecasting*. Amer. Meteor. Soc. (1986).
- Charney, J. C., The use of primitive equations of motion in numerical prediction, *Tellus*, *7*, 6–22 (1955).
- Chen, F., and J. Dudhia, Coupling an advanced land-surface/hydrology model with the Penn state/NCAR MM5 modeling system. Part I: model description and implementation, *Mon. Wea. Rev.*, *129*, 569–585 (2001).
- Chen, S. -H., and W. -Y., Sun, A one dimensional time dependent cloud model, *J. Meteorol. Soc. of Jpn.*, *80*, 99 – 118 (2002).

- Cherubini, T., A., Ghelli, and F., Lalaurette, Verification of precipitation forecasts over the Alpine region using a high-density observing network, *Wea. Forecasting*, *17*, 238–249 (2002).
- Chou, M. -D., and M. J., Suarez, An efficient thermal infrared radiation parameterization for use in general circulation models, *NASA Tech. Memo.*, *104606*, 3–85 (1994).
- Davis, A. C., B., Brown, and R., Bullock, Object-based verification of precipitation forecasts. Part I: methodology and application to mesoscale rain areas, *Mon. Wea. Rev.*, *134*, 1772–1784 (2006).
- Davis, A. C., B., Brown, and R., Bullock, Object-based verification of precipitation forecasts. Part II: application to convective rain system, *Mon. Wea. Rev.*, *134*, 1785–1795 (2006).
- Davis, A. C., B., Brown, R., Bullock, and J. Halley-Gotway, The method for object based diagnostic evaluation (MODE) applied to numerical forecasts from the 2005 NSSL/SPC spring program, *Wea. Forecasting*, *24*, 152–1267 (2009).
- Davolio, S., D. Mastrangelo, M. M. Miglietta, O. Drofa, A. Buzzi, and P. Malguzzi, High resolution simulations of a flash flood near Venice, *Nat. Hazardz Earth Syst. Sci.*, *9*, 1671–1678 (2009).
- Davolio, S., P. Stocchi, A. Benetazzo, E. Bohm, F. Riminucci, M. Ravaioli, X.-M. Li, and S. Carniel, Exceptional Bora outbreak in winter 2012: Validation and analysis of high-resolution atmospheric model simulations in the northern Adriatic area, *Dynamics of Atmospheres and Oceans*, *71*, 1 – 20 (2015).
- Drobinski, P., V. Ducrocq, P. Alpert, E. Anagnostou, K. Beranger, M. Borga, I. Braud, A. Chanzy, S. Davolio, G. Delrieu, C. Estournel, N. Filali Boubrahmi, J. Font, V. Grubisic, S. Gualdi, V. Homar, B. Ivancan-Picek, C. Kottmeier, V. Kotroni, K. Lagouvardos, P. Lionello, M. C. Llasat, W. Ludwig, C. Lutoff, A. Mariotti, E. Richard, R. Romero, R. Rotunno, O. Roussot, I. Ruin, S. Somot, I. Taupier-Letage, J. Tintor, R. Uijlenhoet, and H. Wernli, Hymex: a 10-year multidisciplinary program on the mediterranean water cycle, *Bulletin of the American Meteorological Society*, *95*(7), 1063–1082 (2014).

- Ebert, E. E., J. L., McBride, Verification of precipitation in weather systems: determination of systematic errors, *J. of Hydrology*, 239, 179 – 202 (2000).
- Ebert, E. E., U., Damarath, W., Wergen, and M. E., Baldwin, The WGNE assessment of short-term quantitative precipitation forecasts, *Bull. Am. Meteorol. soc.*, 84, 481–492 (2003).
- Ebert, E. E., Neighborhood verification: a strategy for rewarding close forecasts, *Wea. Forecasting*, 24, 1498–1510 (2009).
- Efstathiou, G. A., N. M., Zoumakis, D., Melas, C. J., Lolis, and P., Kas-somenos, Sensitivity of WRF to boundary layer parameterizations in simulating a heavy rainfall event using different microphysical schemes. Effect on large-scale processes, *Atmos. Res.*, 132-133, 125 – 143 (2013).
- Emanuel, K., An air-sea interaction theory for tropical cyclones. part I: Steady-state maintenance, *J. Atmos. Sci.*, 43, 585–604 (1986).
- Emanuel, K. A., A scheme for representing cumulus convection in large scale models, *J. Atmos. Sci.*, 48, 2313–2335 (1991).
- Emanuel, K. A., and D. J. Raymond, The representation of cumulus con-vection in numerical models, *American Meteorological Society*, (1993).
- Environmental Modeling Center, The GFS atmospheric model, *NCEP Of-fice Note 442*, National Oceanic and Atmospheric Administration (2003).
- Faccini, F., F. Luino, G. Paliaga, A. Sacchini, and L. Turconi, Yet another disaster flood of the Bisagno stream in Genoa (Liguria, Italy): October the 9th-10th 2014 event, *Rend. Online Soc. Geol. It.*, 35, 128–131 (2015).
- Fiori, E., A., Parodi, and F., Siccardi (2011), Uncertainty in prediction of deep moist convective processes: Turbulence parameterizations, micro-physics and grid-scale effects, *Atmos. Res.*, 100, 447 – 456 (2011).
- Fiori, E., A. Comellas, L. Molini, N. Rebora, F. Siccardi, D. J. Gochis, S. Tanelli, and A. Parodi, Analysis and hindcast simulation of an extreme rainfall event in the Mediterranean area: the Genoa 2011 case, *Atmos. Res.*, 138, 13–29 (2014).
- Fletcher, N. H., *The Physics of Rain Clouds*. University Press (1962).

- Fritsch, J. M., and C. F. Chappel, Numerical prediction of convectively driven mesoscale pressure system. Part I: Convective parameterization, *J. Atmos. Sci.*, *37*, 1722–1733 (1890).
- Gilleland, E., D., Ahijevych, B. G., Brown, B., Casati, and E. E., Ebert, Intercomparison of spatial forecast verification methods, *Wea. Forecasting*, *24*, 1416–1430 (2009).
- Glantz, M. H., *Current of Change: Impacts of El Nino and La Nina on Climate and Society*, 3rd ed., 760 pp., Cambridge Univ. Press. (2001).
- Haltiner, G. J. and R. T., Williams, *Numerical prediction and dynamic meteorology*. John Wiley & sons, second edition, (1992).
- Hohenegger, C., and C., Schaer, Atmospheric predictability at synoptic versus cloud-resolving scales, *Bull. Am. Meteorol. Soc.*, *88*, 1783 – 1793 (2007).
- Holton, J. R. (2004), *An introduction to dynamic meteorology*. Academic Press, fourth edition, (2004).
- Hong, S. Y., J., Dudhia, and S. H., Chen, A Revised Approach to Ice Microphysical Processes for the Bulk Parameterization of Clouds and Precipitation, *Mon. Wea. Rev.*, *132*, 103–120 (2004).
- Hong, S. Y., and J. O. J., Lim, Thw WRF Single-Moment 6-Class Microphysics Scheme (WSM6), *J. Korean Meteor. Soc.*, *42*, 129–151 (2006).
- Hong, S. Y, K. S., Lim, J. -H., Kim, and J. -O. J., Lim, Sensitivity Study of Cloud-Resolving Convective Simulation with WRF Using Two Bulk Microphysical Parameterization: Ice-Phase Microphysics versus sedimentation Effects, *J. of Appl. Meteor.*, *48*, 61–76 (2009).
- Janjic, Z. I., Non singular implementation of the Mellor-Yamada level 2.5 scheme in the NCEP meso model, *Tech. Rep. 437*, NOAA Science Center (2002).
- Jansa, A., P. Alpert, P. Arbogast, A. Buzzi, B. Ivancan-Picek, V. Kotroni, M. C. Llasat, C. Ramis, E. Richard, R. Romero, and A. Speranza, MEDEX: a general overview, *Natural Hazards and Earth System Science*, *14*, 1965–1984 (2014).

- Kain, J. S., and J. M. Fritsch, The role of "trigger function" in numerical forecasts of mesoscale convective system, *Meteorol. Atmos. Phys.*, *49*, 93–106 (1992).
- Kain, J. S., The Kain-Fritsch convective parameterization: An update, *J. Appl. Meteor.*, *43*, 170–181 (2004).
- Konor, C. S., G. C., Boezio, C. R., Mechoso, and A., Arakawa, Parameterization of PBL Processes in an Atmospheric General Circulation Model: Description and Preliminary Assessment, *Mon. Wea. Rev.*, *137*, 1061 – 1082 (2009).
- Kuo, H. L., Further studies of the parameterization of the effect of cumulus convection on large scale flow, *J. Atmos. Sci.*, *31*, 1232–1240 (1974).
- Lack, S. A., G. L., Limpert, and N. I., Fox, An object-oriented multiscale verification scheme, *Wea. Forecast.*, *25*, 79 – 92 (2010).
- Lanciani, A., and M., Salvati, Spatial interpolation of surface weather observations in alpine meteorological service, *Foralps*, 1–44 (2008).
- Laprise, L., The Euler equation of motion with hydrostatic pressure as independent variable, *Mon. Wea. Rev.*, *120*, 197–207 (1992).
- Lebeaupin, C., V. Ducrocq, and H. Giordani, Sensitivity of torrential rain events to the sea surface temperature based on high-resolution numerical forecasts, *Journal of Geophysical Research: Atmospheres*, *111*(D12) (2006).
- Lim, K. -S, and S. -Y., Hong, Development of an Effective Double-Moment Cloud Microphysics Scheme with Prognostic Cloud Condensation Nuclei (CCN) for Weather and Climate Models, *Mon. Wea. Rev.*, *138*, 1587–1612 (2010).
- Lin, Y. L., R. D., Farley, and H. D., Orville, Bulk parameterization of the snow field in a cloud model, *J. Appl. Meteor.*, *22*, 1065–1092 (1983).
- Ly, S., C., Charles, and A., Degrè, Geostatical interpolation of daily rainfall at catchment scale: the use of several variogram models in the Ourthe and Ambleve catchments, *Belgium Hydrol. Syst. Sci.*, *15*, 2259 – 2274 (2011).

- Maheras, P., H. A., Flocas, I., Patrikas, and Chr., Anagnostopoulou, A 40 year objective climatology of surface cyclones in the Mediterranean region: spatial and temporal distribution, *Int. J. Climatol.*, *21*, 109–130 (2001).
- Mair, A., and A., Fares, Comparison of rainfall interpolation methods in a mountainous region of a tropical island, *J. Hydro. Engin.*, *16*, 371–383 (2011).
- Mariani, S., M., Casaioli, C., Accadia, M. C., Llasat, F., Pasi, S., Davolio, M., Elementi, G., Ficca, and R., Romero, A limited area model intercomparison on the ‘Montserrat-2000’ flash-flood event using statistical and deterministic methods, *Nat. Hazards Earth Syst. Sci.*, *5*, 565–581 (2005).
- Mass, C. F., D., Ovens, K., Westrick, and B. A., Colle, Does Increasing Horizontal Resolution Produce More Skillful Forecasts?, *Bull. Amer. Meteorol. Soc.*, *83*, 407 – 430 (2002).
- McCann, D. W., The enhanced-V: A satellite observable severe storm signature, *Mon. Wea. Rev.*, *111*, 887–894 (1983).
- McPhaden, M. J., S. E. Zebiak, and M. H. Glantz, ENSO as an integrating concept in earth science, *Science*, *314*, 1740–1745 (2006).
- Meredith, E. P., V. A. Semenov, D. Maraun, W. Park, and A. V. Chernokulsky, Crucial role of Black Sea warming in amplifying the 2012 Krymsk precipitation extreme, *Nature Geoscience*, *8*, 615–619 (2015).
- Mesinger, F. and Arakawa, A., *Numerical methods used in atmospheric models*. GARP publications Vol 1, (1976).
- Miglietta, M. M., A. Moscatello, D. Conte, G. Mannarini, G. Lacorata, and R. Rotunno, Numerical analysis of a Mediterranean ‘hurricane’ over south-eastern Italy: Sensitivity experiments to sea surface temperature, *Atmospheric Research*, *101*, 412 – 426 (2011).
- Miglietta, M. M., and R., Rotunno, Application of theory to observed cases of orographically forced convective rainfall, *Mon. Weather Rev.*, *140*, 3039 – 3053 (2012).

- Mlawer, E. J., S. J., Taubman, P. D., Brown, J. M. Iacono, and S. A., Clough, Radiative transfer for inhomogeneous atmosphere: RRTM, a validated correlated-k model for the long-wave, *J. Geophys. Res.*, *102*, 16663–16682 (1997).
- Morrison, H, and J. O., Pinto, Mesoscale Modeling of Springtime Arctic Mixed-Phase Stratiform Clouds Using a New Two-Moment Bulk Microphysics Scheme, *J. Atmos. Sci.*, *62*, 3683–3704 (2005).
- Morrison, H., G., Thompson, and V., KimTatarskii, Impact of cloud microphysics on the development of trailing stratiform precipitation in a simulated squall line: Comparison of one- and two-moment schemes, *Mon. Wea. Rev.*, *137*, 991–1007 (2009).
- Morrison, H., and J., Milbrandt, Comparison of Two-Moment Bulk Microphysics Schemes in Idealized Supercell Thunderstorm Simulations, *Mon. Wea. Rev.*, *139*, 1103 – 1130 (2011).
- Nuissier, O., V., Ducrocq, D., Ricard, C., Lebeaupin, and S., Anquetin, A numerical study of three catastrophic precipitating events over southern France, I: numerical framework and synoptic ingredients, *Quart. J. Roy. Meteor. Soc.*, *134*, 111 – 130 (2008).
- Ooyama, K. V., A Thermodynamic foundation for modeling the moist atmosphere, *J. Atmos. Sci.*, *47*, 2580–2593 (1990).
- Orlanski, I. A., A rational subdivision of scales for atmospheric process, *Bull. Am. Meteorol. soc.*, *56*, 527–530 (1975).
- Pastor, F., J. A. Valiente, and M. J. Estrela, Sea surface temperature and torrential rains in the Valencia region: modelling the role of recharge areas, *Natural Hazards and Earth System Science*, *15*(7), 1677–1693 (2015).
- Pielke, R. A., *Mesoscale Meteorological Modeling*. Academic Press (2002).
- Rajeevan, M., A., Kesarkar, S. B., Thampi, T. N., Rao, B., Radhakrishna, and M., Rajasekhar, Sensitivity of WRF cloud microphysics to simulations of a severe thunderstorm event over Southeast India, *Ann. Geophys.*, *28*, 603 – 619 (2010).

- Ramis, C., R. Romero, and V. Homar, The severe thunderstorm of 4 October 2007 in Mallorca: an observational study, *Natural Hazards and Earth System Science*, 9(4), 1237–1245 (2009).
- Rebora, N., L. Molini, E. Casella, A. Comellas, E. Fiori, F. Pignone, F. Siccardi, F. Silvestro, S. Tanelli, and A. Parodi, Extreme rainfall in the Mediterranean: what can we learn from observations?, *J. of Hydrometeorology*, 14, 906–922 (2013).
- Ricard, D., V. Ducrocq, and V. Auger, A climatology of the mesoscale environment associated with heavily precipitating events over a Northwestern Mediterranean area, *J. Appl. Meteor. Climatol.*, 51, 468–488 (2012).
- Ricchi, A., M. M. Miglietta, P. P. Falco, A. Bergamasco, A. Benetazzo, D. Bonaldo, M. Sclavo and S. Carniel, On the use of a coupled ocean-atmosphere-wave model during an extreme Cold Air Outbreak over the Adriatic Sea, *Atmos. Res.* 172–173, 48-65 (2016).
- Richardson, L. F., *Weather Prediction by Numerical Process*. Cambridge University Press (1922).
- Rossa, A., P., Nurmi, E., Ebert, *Precipitation: advances in measurement, estimation and prediction*, Meteorological Service (2008).
- Ryan, B. F., On the global variation of precipitating layer clouds, *Bull. Am. Meteorol. soc.*, 77, 53–70 (1996).
- Salby, M. L., *Physics of the Atmosphere and Climate*. Cambridge University Press (2012).
- Salon, S., Ciclogenesi e dinamica dei cicloni sul mar Mediterraneo. Tesi di Laurea in Fisica, Univerità degli studi di Trieste (1998).
- Seager, R., Y., Kushnir, and M. A., Cane, On heat flux boundary conditions for ocean models, *J. Phys. Oceanography*, 25, 3219 – 3230 (1995).
- Silvestro, F., S. Gabellani, F. Giannoni, A. Parodi, N. Rebora, R. Rudari, and F. Siccardi, A hydrological analysis of the 4 November 2011 event in Genoa, *Nat. Hazards Earth Syst. Sci.*, 12, 2743–2752 (2012).

- Silvestro, F., N. Reborá, F. Giannoni, A. Cavallo, and L. Ferraris, The flash flood of the Bisagno Creek on 9th October 2014: An unfortunate combination of spatial and temporal scales, *Journal of Hydrology* (2015).
- Skamarock, W. C., J. B. Klemp, J. Dudhia, D. O. Gill, D. M. Barker, X. Z. Huang, W. Wang, and J. G. Powers, A description of the Advanced Research WRF Version 3, *Tech. rep.*, National Center for Atmospheric Research (2008).
- Speranza, A., A. Buzzi, A. Trevisan, and P. Malguzzi, A theory of deep cyclogenesis in the lee of the Alps. Part I: modifications of baroclinic instability by localized topography, *J. Atmos. Sci.*, *42*, 1521–1535 (1985).
- Stephens, G. L., The parameterization of radiation for numerical weather prediction and climate models, *Mon. Wea. Rev.*, *112*, 826–867 (1984).
- Tafferner, A., Lee cyclogenesis resulting from the combined outbreak of cold air and potential vorticity against Alps, *Meteorol. Atmos. Phys.*, *43*, 31-47 (1990).
- Thompson, G., R. M. Rasmussen, and K. Manning, Explicit forecasts of winter precipitation using an improved bulk microphysics scheme. Part I: Description and sensitivity analysis, *Mon. Wea. Rev.*, *132*, 519–542 (2004).
- Tibaldi, S., A. Buzzi, and P. Malguzzi, Orographically induced cyclogenesis: analysis of numerical experiments, *Mon. Wea. Rev.*, *108*, 1302-1314 (1980).
- Trenberth, K., Uncertainty in hurricanes and global warming, *Science*, *308*, 1753–1754 (2005).
- Tsidulko, M., and P. Alpert, Synergism of upper-level potential vorticity and mountains in Genoa lee cyclogenesis - A numerical study, *Meteorol. Atmos. Phys.*, *78*, 261–285 (2001).
- Tustison, B., D. Harris, and E. Foufoula-Georgiu, Scale issues in verification of precipitation forecasts, *J. Geoph. Res.*, *106*, 11775–11784 (2001).
- Vergassola, M., and A. Mazzino, Structure and intermittency in a passive scalar model, *Phys. Rev. Lett.*, *79*, 1848–1852 (1997).

- Walko, R. L., W. R. Cotton, M. P. Meyers, and J. Y. Harrington, New RAMS cloud microphysics parameterization. Part I: The single moment scheme, *Atmos. Research*, *38*, 29–62 (1995).
- Wallace, J. M. and Hobbs, P. V., *Atmospheric Science*. Academic Press (1977).
- Warner, J. C., B. Armstrong, R. He, and J. B. Zambon, Development of a Coupled Ocean-Atmosphere-Wave-Sediment Transport (COAWST) Modeling System, *Ocean Modelling*, *35*(3), 230 – 244 (2010).
- Weisman, M. L., C., Davies, W., Wang, K. W., Manning, and J. B., Klemp, Experiences with 0-36-h explicit convective forecasts with the WRF-ARW model, *Wea. Forecast.*, *23*, 407 – 437 (2008).
- Wicker, L. J., and W. C. Skamarock, Time splitting methods for elastic models using forward time schemes, *Mon. Wea. Rev.*, *130*, 2088–2097 (2002).
- Wilks, D. S., *Statistical methods in the atmospheric sciences*, ELSEVIER (2006).
- Yano, J. -I., M., Bister<sup>2</sup>, Z, Fuchs, L., Gerard, V. T. J., Phillips, S., Barkidija, and J. -M., Piriou, Phenomenology of convection-parameterization closure, *Atmos. Chem. and Phys.*, *13*, 4111 – 4131 (2013).
- Zampieri, M., P., Malguzzi, and A., Buzzi, Sensitivity of quantitative precipitation forecasts to boundary layer parameterization: a flash flood case study in the Western Mediterranean, *Nat. Hazards Earth Syst. Sci.*, *5*, 603 – 612 (2005).
- Zhu, T., and D.-L. Zhang, The Impact of the Storm-Induced SST Cooling on Hurricane Intensity, *Advances in Atmospheric Sciences*, *23*, 14–22 (2006).